Universitat de Girona

A COMPREHENSIVE METHODOLOGY TO ANALYSE BONDED JOINTS SUBJECTED TO DIFFERENT ENVIRONMENTAL CONDITIONS

Said Ahmed Ibrahim Abdel Monsef

Per citar o enllaçar aquest document:
Para citar o enlazar este documento:
Use this url to cite or link to this publication:
http://hdl.handle.net/10803/669651

ADVERTIMENT. L'accés als continguts d'aquesta tesi doctoral i la seva utilització ha de respectar els drets de la persona autora. Pot ser utilitzada per a consulta o estudi personal, així com en activitats o materials d'investigació i docència en els termes establerts a l'art. 32 del Text Refós de la Llei de Propietat Intel·lectual (RDL 1/1996). Per altres utilitzacions es requereix l'autorització prèvia i expressa de la persona autora. En qualsevol cas, en la utilització dels seus continguts caldrà indicar de forma clara el nom i cognoms de la persona autora i el títol de la tesi doctoral. No s'autoritza la seva reproducció o altres formes d'explotació efectuades amb finalitats de lucre ni la seva comunicació pública des d'un lloc aliè al servei TDX. Tampoc s'autoritza la presentació del seu contingut en una finestra o marc aliè a TDX (framing). Aquesta reserva de drets afecta tant als continguts de la tesi com als seus resums i índexs.

ADVERTENCIA. El acceso a los contenidos de esta tesis doctoral y su utilización debe respetar los derechos de la persona autora. Puede ser utilizada para consulta o estudio personal, así como en actividades o materiales de investigación y docencia en los términos establecidos en el art. 32 del Texto Refundido de la Ley de Propiedad Intelectual (RDL 1/1996). Para otros usos se requiere la autorización previa y expresa de la persona autora. En cualquier caso, en la utilización de sus contenidos se deberá indicar de forma clara el nombre y apellidos de la persona autora y el título de la tesis doctoral. No se autoriza su reproducción u otras formas de explotación efectuadas con fines lucrativos ni su comunicación pública desde un sitio ajeno al servicio TDR. Tampoco se autoriza la presentación de su contenido en una ventana o marco ajeno a TDR (framing). Esta reserva de derechos afecta tanto al contenido de la tesis como a sus resúmenes e índices.

WARNING. Access to the contents of this doctoral thesis and its use must respect the rights of the author. It can be used for reference or private study, as well as research and learning activities or materials in the terms established by the 32nd article of the Spanish Consolidated Copyright Act (RDL 1/1996). Express and previous authorization of the author is required for any other uses. In any case, when using its content, full name of the author and title of the thesis must be clearly indicated. Reproduction or other forms of for profit use or public communication from outside TDX service is not allowed. Presentation of its content in a window or frame external to TDX (framing) is not authorized either. These rights affect both the content of the thesis and its abstracts and indexes.

Universitat de Girona

Doctoral Thesis

A comprehensive methodology to analyse bonded joints subjected to different environmental conditions

Said Ahmed Ibrahim Abdel Monsef

2020

Universitat de Girona

Doctoral Thesis

A comprehensive methodology to analyse bonded joints subjected to different environmental conditions

Said Ahmed Ibrahim Abdel Monsef

2020

Doctoral Program in Technology

Advisors:

Dr. Jordi Renart
University of Girona

Dr. Albert Turon
University of Girona

Thesis submitted to the University of Girona in partial fulfillment for the degree of Doctor of Philosophy

Said Ahmed Ibrahim Abdel Monsef

A comprehensive methodology to analyse bonded joints subjected to different environmental conditions

Doctoral Thesis, 2020

Doctoral Program in Technology

Advisors: Dr. Jordi Renart and Dr. Albert Turon

University of Girona

AMADE Research Group

Escola Politècnica Superior

Department of Mechanical Engineering and Industrial Construction

Carrer Universitat de Girona, 4

17003, Girona

Universitat de Girona

To whom it might concern,

Dr. Jordi Renart Canalias and Dr. Albert Turon Travesa, Associate Professors at the the Department of *Enginyeria Mecànica i de la Construcció Industrial* of *Universitat de Girona*

CERTIFY that the study entitled *A comprehensive methodology to analyse bonded joints subjected to different environmental conditions* has been carried out under their supervision by **Said Ahmed Ibrahim Abdel Monsef** to apply for the doctoral degree with the International mention. We also certify that **Said Ahmed Ibrahim Abdel Monsef** was a full time graduate student at Universitat de Girona, Girona, Spain, from February 2017 to present.

Girona, May 2020,

Dr. Jordi Renart Canalias
Universitat de Girona, Spain

Dr. Albert Turon Travesa
Universitat de Girona, Spain

IN THE NAME OF ALLAH

To my dear family

"Imagination is more important than knowledge. For knowledge is limited, whereas imagination embraces the entire world, stimulating progress, giving birth to evolution."

Albert Einstein

Acknowledgement

I would like to express my gratitude to my advisors, Dr. Jordi Renart and Dr. Albert Turon, for the indefatigable help and for the key contributions that have allowed the development of the present thesis.

I would like to thank also Dr. Pere Maimí who spent a lot of time revising parts of the present thesis. Of course, I am grateful to all members of the research group AMADE at Universitat de Girona for the help and nice moments that I have received from each one.

I have to do a special mention to all members of FEUP and INEGI in University of Porto for their support and making the research stay much more easier and useful.

I would also like to thank my family for the support they provided me through my entire life and in particular, I must acknowledge my parents, my wife and my lovely sons Ahmed and Adam for their support.

In addition, I would like also to thank my professors and colleagues in Zagazig University, Egypt.

Funding

The period of this research has been funded by the Catalan Government (Agència de Gestió d'Ajuts Universitaris i de Recerca), under the Grant 2017 FI_B 00100.

Also, the present work has been partially funded by the Spanish Government (Ministerio de Economia y Competitividad) under contracts RTI2018-099373-B-I00 and RTI2018-097880-B-I00.

Part of the work has been carried out during a three months research stay at INEGI (Institute of Science and Innovation in Mechanical and Industrial Engineering), Universidade do Porto, Funded by AMADE Research Group, between June and September 2019.

List of Publications

The scientific contributions outcome of this thesis are listed below:

- Journal publications

  Published Papers

  1. **S. Abdel Monsef**, A. Ortega, A. Turon, P. Maimí, J. Renart. An efficient method to extract a mode I cohesive law for bonded joints using the double cantilever beam test. **Composites Part B: Engineering**, 2019; 178, p.107424. doi: https://doi.org/10.1016/j.compositesb.2019.107424.
     ISSN: 1359-8368, Impact Factor: 6.864, ranked 3/88 in the category of *Engineering, Multidisciplinary* and ranked 1/25 in the category of *Materials Science, Composites* (1st quartile).

  2. **S. Abdel Monsef**, M. Pérez-Galmés, J. Renart, A. Turon, P. Maimí.The influence of mode II test configuration on the cohesive law of bonded joints. **Composite Structures**, 2020; 234, p.111689. doi: https://doi.org/10.1016/j.compstruct.2019.111689
     ISSN: 0263-8223, Impact Factor: 4.829, ranked 6/25 in the category of *Materials Science, Composites* (1st quartile)[1].

  Papers in processing

  3. **S. Abdel-Monsef**, J. Renart, A. Turon, P. Maimí.Effect of environmental conditions on pure mode I fracture behaviour of adhesively bonded joints.

  4. **S. Abdel-Monsef**, J. Renart, A. Turon, P. Maimí.Effect of environmental conditions on mode II fracture behaviour of adhesively bonded joints.

  5. **S. Abdel-Monsef**, J. Renart, A. Turon, P. Maimí.Effect of environmental conditioning on the cohesive laws of adhesively bonded joints under pure mode I and mode II.

[1] According to the 2018 Journal Citation Reports

6. **S. Abdel-Monsef**, J. Renart, A. Turon, P. Maimí.Simulation of bonded joints under different temperature and ageing conditions using a cohesive zone model.

- Conference communications

7. **S. Abdel Monsef**, J. Renart, A. Turon, P. Maimí. An Efficient Method to Obtain the Cohesive Laws of Bonded Joints in Mode I and Mode II Fracture Tests. 9th International conference on Composite Testing and Model Identification (CompTest 2019), Lulea, Sweden, 27-29 May 2019. Oral presentation.

8. **S. Abdel Monsef**, J. Renart, A. Turon, P. Maimí. Ageing Effect on Pure Mode I Fracture of Adhesively Bonded Joints. 5th International Conference on Structural Adhesive Bonding (AB2019), FEUP, Porto, Portugal, 11-12 July 2019. Oral presentation.

9. **S. Abdel Monsef**, J. Renart, A. Turon, P. Maimí. Formulation of a Cohesive Zone Model with Humidity and Temperature Effects for Modelling Bonded Joints. 7th ECCOMAS Thematic Conference on the Mechanical Response of Composites (COMPOSITES 2019), Girona, Spain, 18-20 September 2019. Oral presentation.

List of Figures

1.1 Usage of adhesive bonding in the Airbus A380 [2]. 2
1.2 Building block approach for testing and numerical simulation. 2
1.3 Flowchart showing the tasks done during this work. 5

2.1 Improved stiffness (left) and stress distribution (right) of adhesively bonded joints in relation to riveted joints [11]. 7
2.2 Bonded joint configurations [12]. 8
2.3 Schematic of the common manufacturing bonding processes between composite components [7]. 9
2.4 Adhesive classification extracted from [12, 13]. 9
2.5 Failure modes in adhesively bonded joints [14]. 10
2.6 Mode I, mode II, and mode III crack propagation modes. 11
2.7 Diagram of environmental parameters influencing the durability of adhesively bonded joints [7]. 12
2.8 Summary of moisture sorption locations and mechanisms [26]. 13
2.9 Comparison of strength variation in bonded FRP/steel joints with increasing exposure duration in moist conditions [27]. The details A, AS, AG and AGS found in [17], refer to the adhesive interface components (A: adhesive, S: Silane and G: glass fibre embedded in the adhesive). . 14
2.10 Fracture surface of fatigue tested AS4/3501 specimens: (a) 20 °C, (b) 50 °C, (c) 90 °C (d) 0 °C, (e) -30 °C and (f) -60 °C ($\times$1000) [34]. . . . 15
2.11 Dugdale's (a) and Barenblatt's (b) cohesive zone models. 18
2.12 Schematic illustration of the DCB, ENF, 4ENF, ELS, ONF, SCB, SLB and OLB specimens [71]. 21
2.13 Idealised shapes of cohesive law. 27
2.14 (a) ENF and (b) DCB test setup [121] 28
2.15 Experimental setup for an MMB test [123]. 28
2.16 Strip yield model for the open hole specimen [136]. 30
2.17 Compact Tension specimen with a FPZ expressed as a superposition of linear problems [138]. 31

3.1 DCB specimen expressed as a superposition of acting loads. 36
3.2 Damage development and FPZ formation in a DCB test after crack initiation: (I) the FPZ is partially developed; (II) the FPZ increases; (III) the FPZ is fully developed; (IV) crack propagation. 40

3.3 Inverse method to obtain the CL where σ^0 is known for 3 selected points: Alternative (i). 42
3.4 Inverse Method to obtain the CL where $\mathcal{G}_{Ic}$ is known for 3 selected points: Alternative (ii). 43
3.5 Inverse Method to obtain the CL where $\mathcal{G}_{Ic}$ and σ^0 are unknown for 3 selected points: Alternative (iii). 43
3.6 FEM using zero thickness cohesive elements. 45
3.7 Analytical and FEM load-displacement curves for $a_0 = 25$ mm, $\mathcal{G}_{Ic} = 0.969$kJ/m^2 and $h = 2.5$ mm, and strong dependence of the load-displacement with σ^0 in agreement with Blackman et al. [106]. The LEFM curve is generated using the procedure found in [142]. 45
3.8 (a) cohesive stresses and (b) displacement jump profiles in the FPZ for the different load levels labeled A, B and C in Figure (3.7) for σ^0=5 MPa. 46
3.9 (a) Predicted load-displacement for FEM and obtained cohesive laws where (b) is Alternative (i), (c) is Alternative (ii) and (d) Alternative (iii), according to Table 3.1. 47
3.10 (a) Load-displacement; (b) CL results from Alternative (iii) with no input parameters in the CL, and; (c) CL obtained from Arrese et al. [129] and the inverse methods developed in section 3.3. 48
3.11 Experimental load-displacement results from [123] with the selected points used in the CL fitting. 49
3.12 Comparison between the experimental J-δ curve [123] and the J-δ curve obtained using the inverse method described in section 3.3. 50

4.1 (a) ENF and (b) ELS specimens expressed as a superposition of acting loads. 52
4.2 (a) Example of an F-U curve with the selected points, 1:k, and (b) the corresponding CL. 55
4.3 (a) ENF and (b) ELS geometry and test fixtures. 57
4.4 Experimental load-displacement curves, tested in [70], that were used to extract the cohesive laws. 58
4.5 Cohesive laws extracted from ELS test results for the material M1 and M2. The line indicates the mean value of the batch and the dots the standard deviation. 58
4.6 Cohesive laws extracted from ENF test results for the material M1 and M2. The line indicates the mean value of the batch and the dots the standard deviation. 59
4.7 Summary of test results related to the value of $\mathcal{G}_{IIc}$(M1ENF), where $\mathcal{G}_{IIc}$ is the area below the CL. J_{ENF} and J_{ELS} are the J-integral values found in [70]. 60
4.8 Average cohesive laws of the different test configurations. 60

4.9 Representative R-curves of M1 specimens for ENF and ELS test results, found in [70]. The J values are related to the $\mathcal{G}_{IIc}$ (M1ENF). 61

5.1 Experimental setup for DCB specimens at different temperature (a) -55°C, (b) Room temperature and (c) 80°C. 67
5.2 Experimental load-displacement curves from DCB tests on A1 bonded joints. 70
5.3 Experimental load-displacement curves from DCB tests on A2 bonded joints. 71
5.4 R-Curve results from DCB tests on A1 bonded joints. 72
5.5 R-Curve results from DCB tests on A2 bonded joints. 73
5.6 J-integral vs opening displacement of DCB tests on A1 bonded joints. . 74
5.7 J-integral vs opening displacement of DCB tests on A2 bonded joints. . 75
5.8 Fractured surfaces of tested A1 bonded joints. The end of the pre-crack region and the final crack propagation during the test are indicated with IN and END, respectively, for each fractured surface. Units are in mm. 77
5.9 Fractured surfaces of tested A2 bonded joints. The end of the pre-crack region and the final crack propagation during the test are indicated with IN and END, respectively, for each fractured surface. Units are in mm. 78
5.10 Summary of the DCB results. 79

6.1 Experimental setup for ELS specimens tested at: (a) -55°C, (b) 80°C and (c) room temperature (RT). 83
6.2 Representation of load introduction in ELS test configuration. 84
6.3 Experimental load-displacement curves from A1 ELS tests. 86
6.4 Experimental load-displacement curves from A2 ELS tests. 87
6.5 R-Curve results from A1 ELS tests. 88
6.6 R-Curve results from A2 ELS tests. 89
6.7 J-integral vs opening displacement of A1 ELS results. 90
6.8 J-integral vs opening displacement of A2 ELS results. 91
6.9 Summary of the ELS results. All the values are normalized with RT results. 92
6.10 Fractured surface pictures of tested ELS A1 specimens. The end of the pre-crack region and the final crack propagation during the test are indicated with IN and END, respectively, for each fractured surface. . . 93
6.11 Fractured surface pictures of tested ELS A2 specimens. The end of the pre-crack region and the final crack propagation during the test are indicated with IN and END, respectively, for each fractured surface. . . 94

7.1 A sketch of multilinear cohesive laws with four line segments used to fit the obtained J-integral of (a) DCB and (b) ELS results. 97

7.2 Representative load-displacement curves of DCB and ELS tests for A1 and A2 configurations under different environmental conditions (L: non-aged and W: wet-aged). 98
7.3 DCB results of the non-aged A1 specimens with (a) the J-integral curves obtained from RT specimens, (b) 80ºC, (c) -55ºC and (d) the cohesive laws obtained from fitting the average J-integral curves. 99
7.4 DCB results of the non-aged A2 specimens with (a) the J-integral curves obtained from RT specimens, (b) -55ºC and (c) the cohesive laws obtained from fitting the average J-integral curves. 99
7.5 DCB results of the wet-aged A1 specimens with (a) the J-integral curves obtained from RT specimens, (b) 80ºC, (c) -55ºC and (d) the cohesive laws obtained from fitting the average J-integral curves. 100
7.6 DCB results of the wet-aged A2 specimens with (a) the J-integral curves obtained from RT specimens, (b) 80ºC, (c) -55ºC and (d) the cohesive laws obtained from fitting the average J-integral curves. 101
7.7 ELS results of the non-aged A1 specimens with (a) the J-integral curves obtained from RT specimens, (b) -55ºC and (c) the cohesive laws obtained from fitting the average J-integral curves. 102
7.8 ELS results of the non-aged A2 specimens with (a) the J-integral curves obtained from RT specimens, (b) -55ºC and (c) the cohesive laws obtained from fitting the average J-integral curves. 103
7.9 ELS results of the wet-aged A1 specimens with (a) the J-integral curves obtained from RT specimens, (b) 80ºC, (c) -55ºC and (d) the cohesive laws obtained from fitting the average J-integral curves. 104
7.10 ELS results of the wet-aged A2 specimens with (a) the J-integral curves obtained from RT specimens, (b) 80ºC, (c) -55ºC and (d) the cohesive laws obtained from fitting the average J-integral curves. 104
7.11 DCB results summary normalized by the room temperature result for each configuration. 106
7.12 ELS results summary normalized by the room temperature result for each configuration. 106
7.13 Summary of the non-aged and wet-aged specimens tested at RT where the results are normalized with the non-aged case. 108

8.1 A mixed-mode multilinear cohesive law. 112
8.2 A sketch of a multilinear cohesive law with four line segments. 115
8.3 The non-aged cohesive laws for two interface types A1 and A2 116
8.4 Experimental load-displacement results of DCB specimens in dash lines with the finite element results in solid lines. 118
8.5 Experimental load-displacement results of ELS specimens in dash lines with the finite element results in solid lines. 119

8.6 Load-displacement response of the (a) MMB 20%, (b) MMB 50%, and (c) MMB 70% tests for different ageing and temperatures. 120
8.7 Dimensions and test setup of the skin-stringer specimen found in [52]. 121
8.8 Load-displacement curves of the simulated skin-stringer specimens under different environmental conditions for two configurations A1 and A2. 122

9.1 Schematic illustration of environmental conditions influences on the simplified cohesive laws. 127

A.1 Finite element model of half of the DCB and its boundary conditions. . 131

List of Tables

2.1 Summary of LEFM-based data reduction expressions used in the ENF test [70]. 24
2.2 Summary of LEFM-based data reduction expressions used in the ELS test [70]. 25
2.3 Summary of J-integral data reduction methods for the DCB, ELS and ENF tests. 26

3.1 Required parameters for the implementation of each alternative. 42
3.2 Elastic properties of the ply and interface properties. 44

4.1 Specimen configurations. 56
4.2 Summary of the average fracture toughness of the ENF tests related to the M1ENF value. 59
4.3 Summary of the average fracture toughness of the ELS tests related to the M1ENF value (Table 4.2). 59

5.1 Specimen configurations tested. 66
5.2 Summary of results of DCB tests on A1 bonded joints. 76
5.3 Summary of results of DCB tests on A2 bonded joints. 76

6.1 Specimen configurations tested. 82
6.2 A1 ELS tests results summary. 92
6.3 A2 ELS tests results summary. 92

8.1 Elastic properties of the ply used in the MMB simulations [52]. 119

Contents

Declaration v

List of Publications xiii

1 Introduction and objectives 1
- 1.1 Overview . . . 1
- 1.2 Motivation . . . 3
- 1.3 Objectives . . . 3
- 1.4 Thesis Layout . . . 4

2 Literature review 7
- 2.1 Introduction . . . 7
- 2.2 Bonded joints . . . 7
  - 2.2.1 Adhesive joint failure . . . 10
- 2.3 Effect of environmental conditions . . . 11
  - 2.3.1 Effect of moisture . . . 11
  - 2.3.2 Effect of temperature . . . 15
  - 2.3.3 Effect of combined moisture and temperature . . . 16
- 2.4 Modeling of bonded joints . . . 17
- 2.5 Experimental characterization of bonded Joints . . . 19
- 2.6 Data reduction methods . . . 22
  - 2.6.1 Linear Elastic Fracture Mechanics . . . 22
  - 2.6.2 J-integral approach . . . 25
- 2.7 Experimental methods to obtain the cohesive laws . . . 26

I Methodology to obtain cohesive laws 33

3 An efficient method to extract a Mode I cohesive law 35
- 3.1 Introduction . . . 35
- 3.2 A direct method based on Dugdale's condition to obtain the load-displacement curve . . . 35
- 3.3 Inverse Method to obtain the cohesive law . . . 40
- 3.4 Validation of the Direct and the inverse methods . . . 44
  - 3.4.1 Validation of the Direct Method . . . 44

3.4.2 Validation of the Inverse Method 46
3.5 FPZ analysis for different material systems 46
3.5.1 Cohesive law on delamination tests 47
3.5.2 J-δ curves for bonded joints 48

4 The influence of mode II test configuration on the cohesive law 51
4.1 Introduction 51
4.2 Analytical method to obtain the cohesive law from a mode II fracture test 51
4.3 Experimental set-up and test specimens 56
4.4 Results and discussion 57

II Experimental work 63

5 Effect of environmental conditioning on pure mode I fracture behaviour 65
5.1 Introduction 65
5.2 Methodology 65
5.2.1 Material and specimen configuration 65
5.2.2 Test and instrumentation 66
5.2.3 Data reduction methods 68
5.3 Results 69
5.4 Discussion 78

6 Effect of environmental conditioning on mode II fracture behaviour 81
6.1 Introduction 81
6.2 Methodology 81
6.2.1 Material and specimen configuration 81
6.2.2 Test and instrumentation 82
6.2.3 Data reduction methods 84
6.3 Results 85
6.4 Discussion 94

7 Effect of environment conditioning on the cohesive laws 97
7.1 Introduction 97
7.2 Methodology 97
7.3 Results 98
7.4 Discussion 105

III Cohesive zone model 109

8 Simulation of bonded joints under different temperature and ageing conditions 111

8.1 Introduction . . . 111
8.2 Model formulation . . . 111
8.2.1 Damage model . . . 111
8.2.2 Effect of temperature and ageing on the CL . . . 114
8.3 Finite element models and numerical results . . . 114
8.3.1 Calibration of the cohesive law . . . 115
8.3.2 Validation examples . . . 117
8.3.3 Simulation of MMB bonded joints with environmental effects 119
8.3.4 Simulation of a skin stringer substructure . . . 121

IV Conclusions and future work 123

9 Conclusions and future work 125
9.1 Main Conclusions . . . 125
9.1.1 Methodology to obtain cohesive laws . . . 125
9.1.2 Effect of temperature and ageing . . . 126
9.1.3 Simulation of bonded joints under different temperature and ageing conditions . . . 127
9.2 Future work . . . 127

V Annex 129

A Obtaining the non-dimensional parameters 131

B Cohesive laws dependence fitting matrices 133

Bibliography 135

Abstract

Cohesive zone models are widely used for modelling delamination and bonded joints under different loading conditions. However, existing formulations do not consider the influence of environmental effects on the mechanical properties. The main difficulty is the obtention of the cohesive law. To measure the cohesive law, experimental methods have been developed in the literature, but most of existing approaches are tedious and expensive because they require the use of additional measurement techniques to measure the J-integral and the crack opening displacements. Moreover, their application is not straightforward when testing under extreme conditions using environmental chambers.

The objective of this dissertation is to derive efficient methods to measure the cohesive law and study the influence of the environmental conditions on the cohesive law parameters. Three main developments have been done.

Firstly, an objective inverse method has been developed to extract the cohesive law from experimental load-displacement data. The method combines a model based on Dugdale's condition with an inverse method to represent the fracture process zone of mode I. The comparison of the method with other methods available in the literature show a good agreement. However, the method presented reduces the instrumentation needed during the test and can be also used when testing under environmental conditions.

Secondly, the influence of the mode II test configuration on the cohesive law of bonded joints is discussed. The inverse method developed for mode I is adapted for End-Notched Flexure and End-Load Split test configurations. The analysis of the experimental data confirms the independence of the cohesive law with the test configuration.

Thirdly, the influence of environmental conditions on the fracture behaviour of two types of adhesively bonded joints is experimentally studied for Mode I and Mode II tests. Two types of adhesively bonded joints, wet-aged and non-aged, were tested at various temperatures (-55ºC, room temperature and 80ºC). Wet-aged specimens were exposed to accelerated ageing in an environmental chamber at 70ºC/85 RH

for four years; meanwhile, the non-aged specimens were stored in the laboratory under controlled conditions at room temperature. The results obtained show that accelerated ageing reduces the fracture properties of bonded joints under mode I and mode II, while the exposure to high temperature has a slight effect on the response. Conversely, freezing temperature leads to more brittle behaviour and a reduction in the fracture toughness.

The dependence of the cohesive laws on the testing temperature and ageing is also analysed. The inverse method presented has been used to extract the cohesive law under different environmental conditions. An increase on the testing temperature has a slight effect on the area under the Mode I cohesive law. Conversely, the energy dissipation in Mode II tests increases for higher temperature due to an increase on the ductility of the adhesive. On the other hand, freezing temperatures cause brittle behaviour and reduces the fracture toughness. Moreover, the presence of moisture has been proven to cause significant degradation of the fracture response of the joints.

Finally, a phenomenological expression that describes the effect of temperature and ageing on the cohesive law shape is formulated. Using this expression, a constitutive cohesive zone model is enhanced to simulate the influence of the environmental conditions on the mechanical response. The constitutive model is implemented in the commercial FE program ABAQUS by means of a user element subroutine. The implementation is verified for different temperature and ageing conditions. Moreover, different combinations of environmental conditions and loading scenarios are simulated to verify the efficiency of the enhanced formulation.

Resum

Els models de zona cohesiva s'utilitzen per simular delaminació i el comportament mecànic de les unions adhesives. Tot i això, les formulacions existents no consideren la influència dels efectes ambientals en les propietats mecàniques. La principal dificultat és l'obtenció de la llei cohesiva. Existeixen métodes per mesurar la llei cohesiva, però la majoria són tediosos i costosos perquè requereixen de l'ús de tècniques instrumentals adicionals per mesurar la integral J i els desplaçaments d'obertura de fissures. A més, no és senzilla la seva aplicació quan es fan proves en condicions extremes utilitzant cambres ambientals.

L'objectiu d'aquesta tesi és obtenir mètodes eficients per mesurar la llei cohesiva i estudiar la influència de les condicions ambientals en els paràmetres d'aquesta. S'han realitzat tres aportacions principals:

En primer lloc, s'ha desenvolupat un mètode invers per extreure la llei cohesiva a partir de dades experimentals de desplaçament i càrrega. El mètode combina un model basat en la condició de Dugdale amb un mètode invers per representar la zona de procés de fractura en mode I. La comparació del mètode amb altres mètodes disponibles a la literatura mostra un bon ajust. Cal destacar però que el mètode presentat redueix la instrumentació necessària durant l'assaig i es pot utilitzar també en assajos amb diferents condicions ambientals.

En segon lloc, es discuteix la influència de la configuració de l'assaig en mode II sobre la llei cohesiva. El mètode invers desenvolupat per al mode I s'ha adaptat a les configuracions ENF i CELS. L'anàlisi de les dades experimentals confirma la independència de la llei cohesiva amb la configuració de l'assaig.

En tercer lloc, la influència de les condicions ambientals en el comportament de fractura de dos tipus d'unions adhesives (envelliment higrotèrmic i sense envelliment) s'estudia experimentalment per a assajos de mode I i mode II. Les probetes amb envelliment higrotèrmic van estar exposades a un envelliment accelerat en una cambra ambiental a 70ºC / 85 RH durant quatre anys; les provetes no envellides es van guardar al laboratori en condicions controlades a temperatura ambient. Els assajos s'han realitzat a diverses temperatures (-55ºC, temperatura ambient i 80ºC).

Els resultats obtinguts mostren que l'envelliment accelerat redueix les propietats de fractura en mode I i mode II de les unions, mentre que l'exposició a alta temperatura té un lleuger efecte sobre la resposta. Per contra, a baixes temperatures s'observa un comportament més fràgil i una reducció de la tenacitat a la fractura.

També s'analitza la dependència de les lleis cohesives de la temperatura i l'envelliment. El mètode invers presentat s'ha utilitzat per extreure la llei cohesiva en diferents condicions ambientals. Un augment de la temperatura de l'assaig té un lleuger efecte a la zona de la llei cohesiva en Mode I. Per contra, la dissipació d'energia a les proves en mode II augmenta a l'augmentar la temperatura a causa d'un augment de la ductilitat de l'adhesiu. D'altra banda, les baixes temperatures provoquen un comportament fràgil i redueixen la tenacitat de la fractura també en mode II. A més, s'ha comprovat que la presència d'humitat provoca una degradació significativa de la resposta a la fractura de les unions.

Finalment, es formula una expressió fenomenològica que descriu l'efecte de la temperatura i l'envelliment en la llei cohesiva. Mitjançant aquesta expressió, s'actualitza la formulació d'un model de zona cohesiva constitutiva per simular la influència de les condicions ambientals en la resposta mecànica. El model constitutiu s'implementa en el programa FE comercial ABAQUS mitjançant una subrutina d'elements d'usuari. La implementació es verifica per a diferents condicions de temperatura i envelliment. A més, es simulen diferents combinacions de condicions ambientals i escenaris de càrrega per verificar l'eficàcia de la formulació millorada.

Resumen

Los modelos de zona cohesiva se utilizan para simular delaminación y el comportamiento mecánico de las uniones adhesivas. Sin embargo, las formulaciones existentes no consideran la influencia de los efectos ambientales en las propiedades mecánicas. La principal dificultad es la obtención de la ley cohesiva. Existen métodos para medir la ley cohesiva, pero la mayoría son tediosos y costosos porque requieren del uso de técnicas instrumentales adicionales para medir la integral J y los desplazamientos de apertura de fisuras. Además, no es sencilla su aplicación cuando se realizan pruebas en condiciones extremas utilizando cámaras ambientales.

El objetivo de esta tesis es obtener métodos eficientes para medir la ley cohesiva y estudiar la influencia de las condiciones ambientales en los parámetros de la misma. Se han realizado tres aportaciones principales:

En primer lugar, se ha desarrollado un método inverso para extraer la ley cohesiva a partir de datos experimentales de desplazamiento y carga. El método combina un modelo basado en la condición de Dugdale con un método inverso para representar la zona de proceso de fractura en modo I. La comparación del método con otros métodos disponibles en la literatura muestra un buen ajuste. Cabe destacar pero que el método presentado reduce la instrumentación necesaria durante el ensayo y se puede utilizar también en ensayos con diferentes condiciones ambientales.

En segundo lugar, se discute la influencia de la configuración del ensayo en modo II sobre la ley cohesiva. El método inverso desarrollado para el modo I se ha adaptado a las configuraciones ENF y CELS. El análisis de los datos experimentales confirma la independencia de la ley cohesiva con la configuración del ensayo.

En tercer lugar, la influencia de las condiciones ambientales en el comportamiento de fractura de dos tipos de uniones adhesivas (envejecimiento higrotérmico y sin envejecimiento) se estudia experimentalmente para ensayos de modo I y modo II. Las probetas con envejecimiento higrotérmico estuvieron expuestas a un envejecimiento acelerado en una cámara ambiental a 70ºC / 85 RH durante cuatro años; las probetas no envejecidas se guardaron en el laboratorio en condiciones controladas a temperatura ambiente. Los ensayos se han realizado en varias temperaturas (-

55ºC, temperatura ambiente y 80ºC). Los resultados obtenidos muestran que el envejecimiento acelerado reduce las propiedades de fractura en modo I y modo II de las uniones, mientras que la exposición a alta temperatura tiene un ligero efecto sobre la respuesta. Por el contrario, a bajas temperaturas se observa un comportamiento más frágil y una reducción de la tenacidad a la fractura.

También se analiza la dependencia de las leyes cohesivas de la temperatura y el envejecimiento. El método inverso presentado se utiliza para extraer la ley cohesiva en diferentes condiciones ambientales. Un aumento de la temperatura del ensayo tiene un ligero efecto en la zona de la ley cohesiva en Modo I. Por el contrario, la disipación de energía en las pruebas en modo II aumenta al aumentar la temperatura a causa de un aumento de la ductilidad del adhesivo. Por otra parte, las bajas temperaturas provocan un comportamiento frágil y reducen la tenacidad de la fractura también en modo II. Además, se ha comprobado que la presencia de humedad provoca una degradación significativa de la respuesta a la fractura de las uniones.

Finalmente, se formula una expresión fenomenológica que describe el efecto de la temperatura y el envejecimiento en la ley cohesiva. Mediante esta expresión, se actualiza la formulación de un modelo de zona cohesiva para simular la influencia de las condiciones ambientales en la respuesta mecánica. El modelo constitutivo se implementa en el programa FE comercial ABAQUS mediante una subrutina de elementos de usuario. La implementación se verifica para diferentes condiciones de temperatura y envejecimiento. Además, se simulan diferentes combinaciones de condiciones ambientales y escenarios de carga para verificar la eficacia de la formulación mejorada.

1 Introduction and objectives

1.1 Overview

The fact that Greta Thunberg, the best known environmental activist on climate change at present, used an electric sailboat to cross the Atlantic Sea to assist the Climate Action Summit 2019 in New York [1] uncovers the colossal impact the air transport has on the climatic change. The conclusion is obvious: new aircraft designs need to be environmentally more sustainable. In other words, there is a need for more efficient and less contaminating engines and lighter but also durable structures, the industry has to optimize the development times and resources needed in the design and the manufacturing of new products by using more sophisticated numerical tools.

To obtain more efficient lightweight structures, it is necessary to develop stronger materials but also more efficient assembling systems. In this respect, in a basic search on adhesives, one can easily find the virtues of a bonded joint against conventional methods (e.g. mechanical fasteners). Being the weight reduction one of the most appreciated attributes, especially by the aeronautical industry. For civil aircraft, bonding of composites is well-established for various secondary joints. Airbus A380 features bonded joints, for instance, in the rear pressure bulkhead, the ailerons, the vertical tailplane and the radome as illustrated in Fig. 1.1 [2]. However, to achieve their full implementation in aircraft primary structures, the mechanical response of a bonded joint under environments different from "as received" conditions must be understood, as well as, how the passing of time (under these environments) changes their mechanical properties.

On the aim of investigating the fracture behaviour of aircraft structures, from material characterization tests at a coupon level to full-scale structures, as shown in Fig. 1.2, the scientific community has developed many fracture tests which can be found in the literature. However, these tests are extensive and expensive testing programs especially at the coupon level and the element level. Consequently, the finite element framework is widely used to move from physical testing to numerical simulations which reduce the number of physical tests.

Cohesive Zone Models (CZM) are widely used for modelling bonded joints. The main difficulty concerning the use of CZM is the obtention of the interface cohesive law. To measure the cohesive law of bonded joints, experimental methods have been

Fig. 1.1.: Usage of adhesive bonding in the Airbus A380 [2].

developed which are tedious and expensive because they require the use of additional measurement techniques in addition to the basic test outputs (load and displacement) to measure the J-integral and the crack opening displacement, essential parameters to obtain the cohesive law. Moreover, the crack tip opening displacement can be extremely difficult to measure in specimens tested in an environmental chamber, e.g., tests at high or cryogenic temperatures.

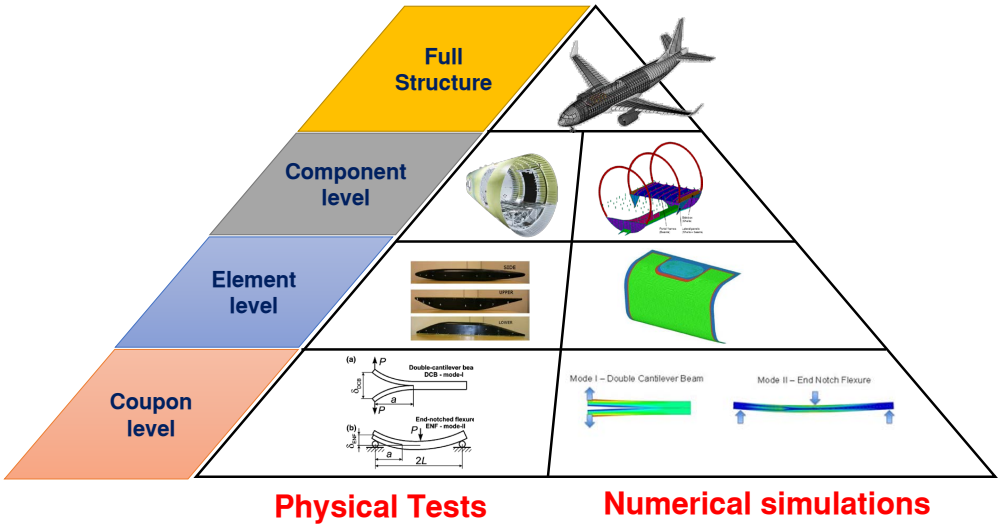

Fig. 1.2.: Building block approach for testing and numerical simulation.

The work done in this thesis focuses on the fracture behaviour of adhesively bonded joints under two different failure modes (mode I and mode II).

1.2 Motivation

The environmental variations have a meaningful impact on the mechanical properties of bonded joints, specially temperature and humidity [3, 4]. The exposure to high temperatures affects both chemical and physical properties of the adhesive, changing the bond strength [5]. Furthermore, the existence of moisture in bonded joints may affect the interface between the adherend and the adhesive in addition to the physical and chemical properties of the adhesive itself [6]. The exposure to a combination of moisture and temperature leads to more damage than to an individual condition [7–9].

Meanwhile, the use of CZM has become an essential tool to capture the response of the composite under different loading modes. CZM has been proved as a good method to simulate interlaminar fracture. However, the experimental determination of the cohesive law and its dependence on the environmental effects is still an open issue. In other words, the existing techniques in literature, to define the cohesive law, require very high-resolution equipment to capture the opening displacements that can be extremely difficult while testing in an environmental chamber.

1.3 Objectives

Based on the proposed motivations, the main objective for this thesis is to find an efficient methodology to investigate the fracture behaviour of bonded joints under different environmental conditions (temperature and ageing). To achieve this global objective, several sub-objectives need to be accomplished.

- The first sub-objective focuses on developing a method to obtain the cohesive laws of bonded joints based on the basic test output (load and displacement) for both mode I and mode II.
- Study the effect of environmental changes on the fracture behaviour of bonded joints.
- Obtain the dependencies of the cohesive laws on the environmental changes (temperature and ageing).
- Combine the effect of environmental changes with the cohesive zone model.

1.4 Thesis Layout

Figure 1.3 shows a flowchart illustrating the procedure followed to achieve the previous objectives. In Chapter 2 a general review on bonded joints and the effect of environmental changes on the fracture properties of bonded joints is presented (focusing on the effect of temperature and thermal ageing). Also, a review of the methods available to model bonded joints and the experimental measurement of the parameters required by the models is included. Then, a detailed review is done on the various methods to define the cohesive laws, one of the main properties needed to model the interface and essential to understand the fracture behaviour of the adhesively bonded joints.

Based on the analysis done in Chapter 2, this thesis is divided into three main parts: analytical, experimental and finite element modelling. In part I, an efficient method to obtain the cohesive laws is presented for both mode I (using the Double Cantilever Beam test) and mode II (using End-Notched Flexure and End-Load Split tests) in addition to the influence of the mode II test configuration on the cohesive law is discussed. This part extends from Chapter 3 to Chapter 4.

In part II, the influence of different environmental conditions (focusing on the effect of temperature and ageing) on the fracture behaviour of secondary bonded adhesive joints is experimentally investigated under mode I and mode II tests, in Chapters 5 and 6. In Chapter 7, the experimental results are analysed using the methodology developed in Chapters 3 and 4 to obtain the cohesive laws.

Once the cohesive laws as a function of the environmental conditions are obtained, a cohesive zone model is implemented, in Chapter 8, using commercial software to simulate bonded joints under different temperature and ageing conditions.

Finally, in Chapter 9, conclusions are drawn, and topics for future work are suggested.

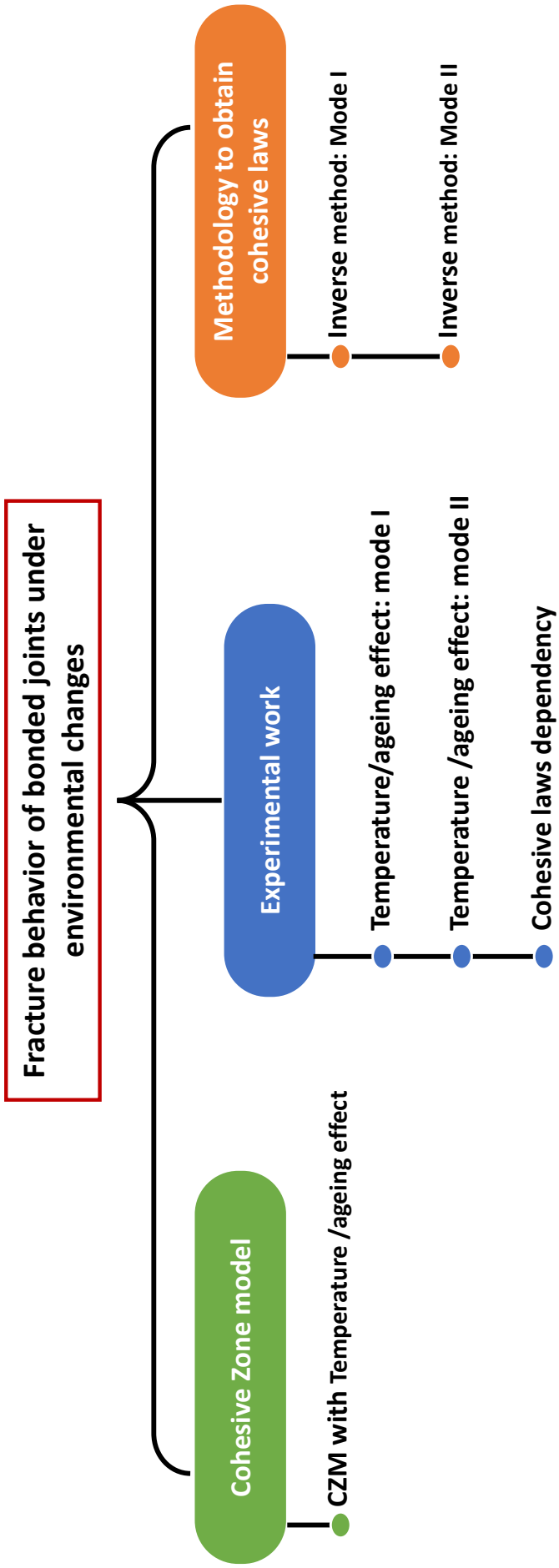

Fig. 1.3.: Flowchart showing the tasks done during this work.

Literature review

2

2.1 Introduction

Adhesively bonded joints are increasingly used in many applications, such as aerospace, automotive, marine and civil constructions, to reduce carbon fingerprint. This is because of several advantages that adhesive joints have over other joining methods, like welding, bolting and riveting, such as a high strength to weight ratio and the ability to join different materials. They also provide a load redistribution which increase the joint stiffness and present a uniform stress distribution, Fig. 2.1, in addition to higher strength-to-weight ratios, better fatigue behaviour and reduction of the maintenance costs [10].

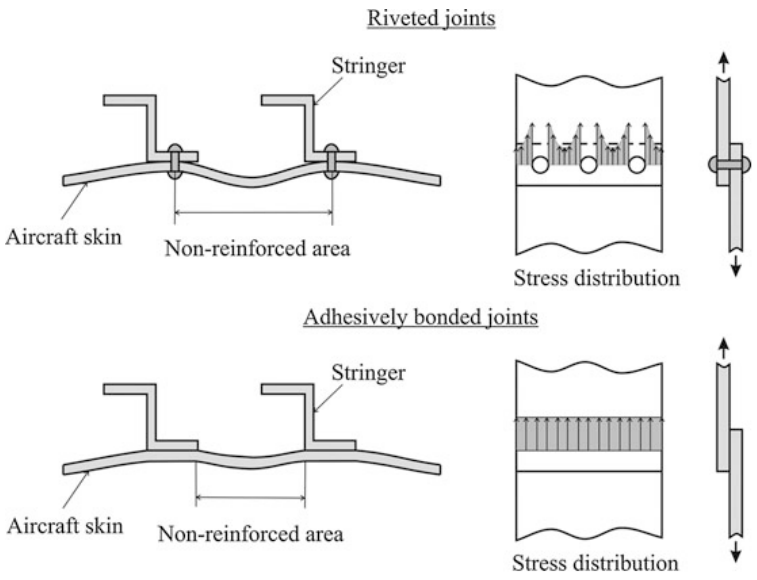

Fig. 2.1.: Improved stiffness (left) and stress distribution (right) of adhesively bonded joints in relation to riveted joints [11].

2.2 Bonded joints

Adhesive bonded joints commonly consist of two adherends and an adhesive material that produces bond interactions between the adhesive and the adherend. For structural bonded joints, the internal loads act on one adherend and transfer the load to the other substrate through the adhesive interface, therefore, larger bonding areas are required [12].

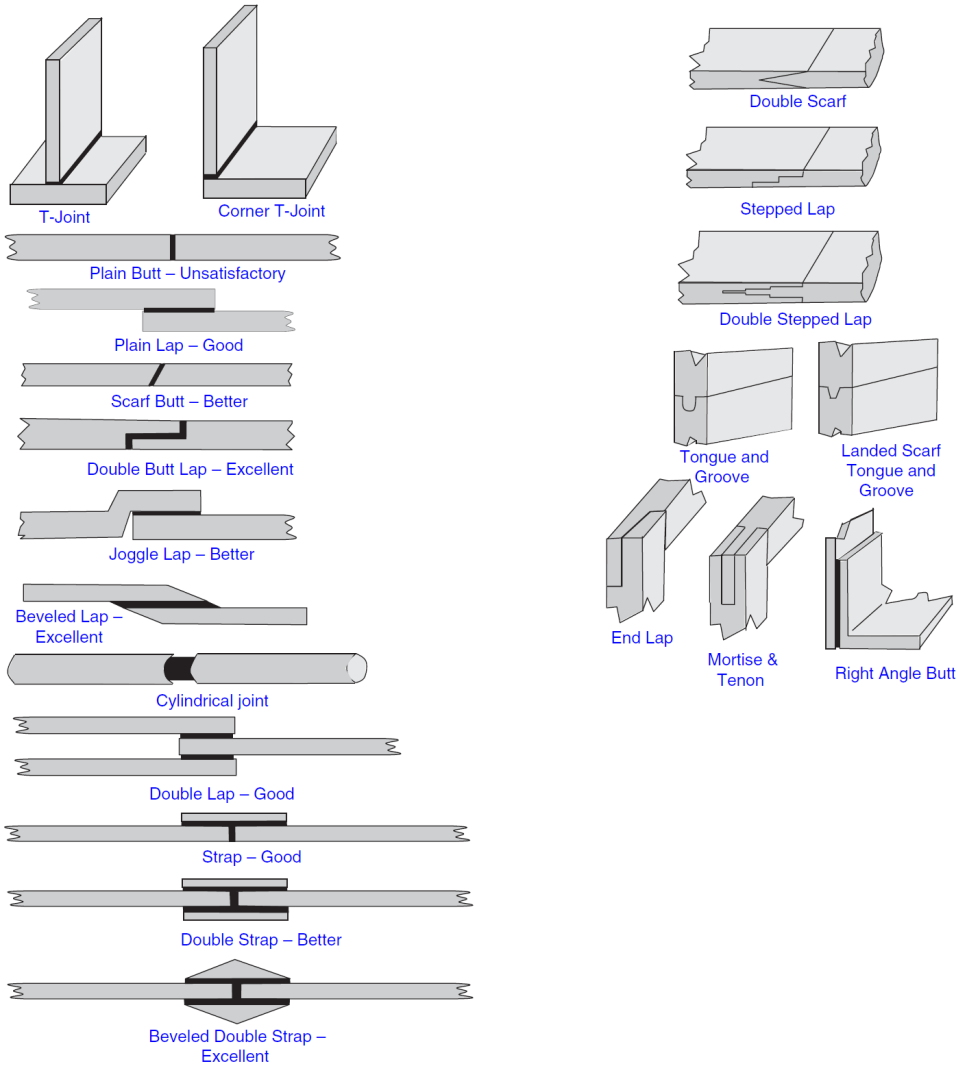

Fig. 2.2.: Bonded joint configurations [12].

Fig. 2.2 summarizes the most used bonded joint configurations. Lap joints (single lap, double lap, butt scarf lap, double lap scarf) provide larger bonding areas while in the case of butt joints and T-joints the bonding regions are smaller and limited to the wall thickness of the part. Therefore, the lap joints provide higher strength. Besides, the mechanical properties of the adhesive and adherends play an essential role in bonded joints design.

Concerning aeronautical structures made of composites, bonded joints are formed between composite substrates following one of the three manufacturing bonding processes, namely co-curing, co-bonding and secondary bonding. Fig. 2.3 shows the schemes of the aforementioned three bonding processes between composite components [7]. The co-bonding process is used when one substrate is cured with the adhesive, while the second substrate is cured together with the adhesive layer.

The secondary bonding process is used to join two or more pre-cured adherends. Finally, it is possible to have multi-material bonding by joining composites to metal.

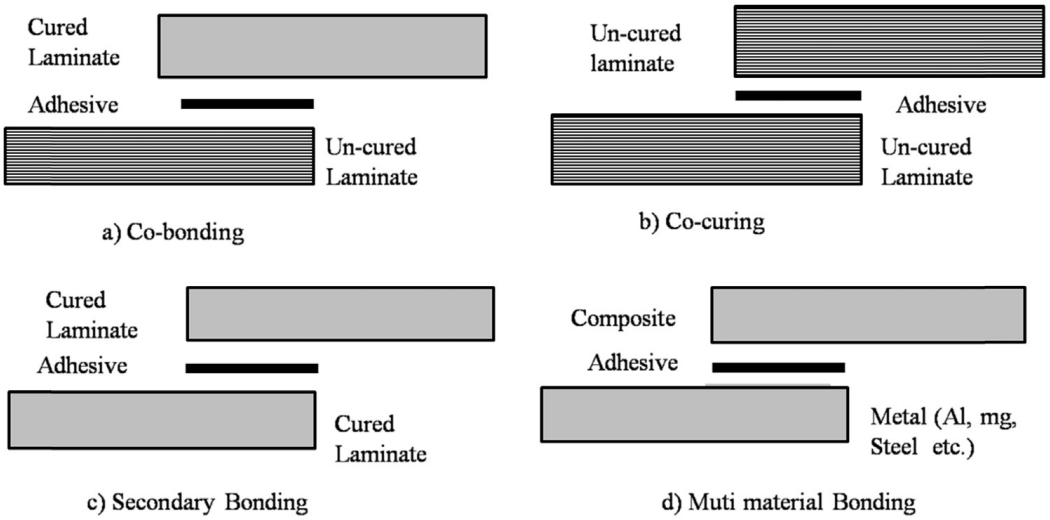

Fig. 2.3.: Schematic of the common manufacturing bonding processes between composite components [7].

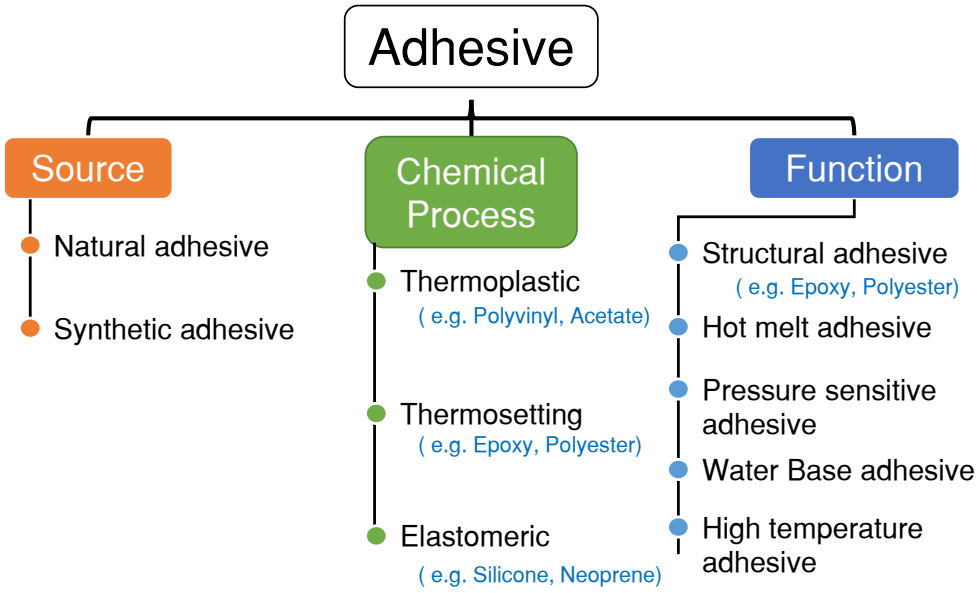

Fig. 2.4.: Adhesive classification extracted from [12, 13].

The adhesive type is the primary responsible of the bonded joint behaviour. Therefore, the selection of adhesive type, from a large number of adhesives on the market, is essential to fulfil the requirements that the joint needs to meet. It is convenient to group the adhesives according to their common characteristics to facilitate the selection process. Indeed, adhesives can be grouped into several classifications, including the adhesive source, the function and the chemical process, as shown in Fig. 2.4. One of the most important structural adhesives is epoxy which is durable

and brittle; however, it can be formulated to be flexible and/or tough without tensile strength loss [13]. Epoxy adhesives are widely used to bond a large variety of adherends, and they can be cured under different temperatures: room temperature or elevated temperature, and that can be used under dry or wet conditions where the service temperature range is -55°C to 121°C in the aircraft industry.

2.2.1 Adhesive joint failure

Design of bonded joints is usually based on the failure analysis of the joint, which can be performed using the stress analysis together with a set of strength-based failure criteria corresponding to the specific failure modes of the composite bonded joints [14]. When conducting an experimental test, or during commissioning of a structural component, different types of failures can occur within the adherends and/or the adhesive, as shown in Fig. 2.5. Adhesives are more susceptible to failure due to tensile strain than pure shear and compression. A failure inside the adhesive is called cohesive failure. On the other hand, the crack may progress towards the adherend causing interlaminar delamination (interlaminar failure) which is a failure due to the deficiency of composite adherends subjected to interlaminar shear and/or transverse normal peel stresses. Moreover, the interface may fail between the adhesive and adherent (adhesive failure). The aforementioned failure modes can occur individually or in a combination of different failure modes.

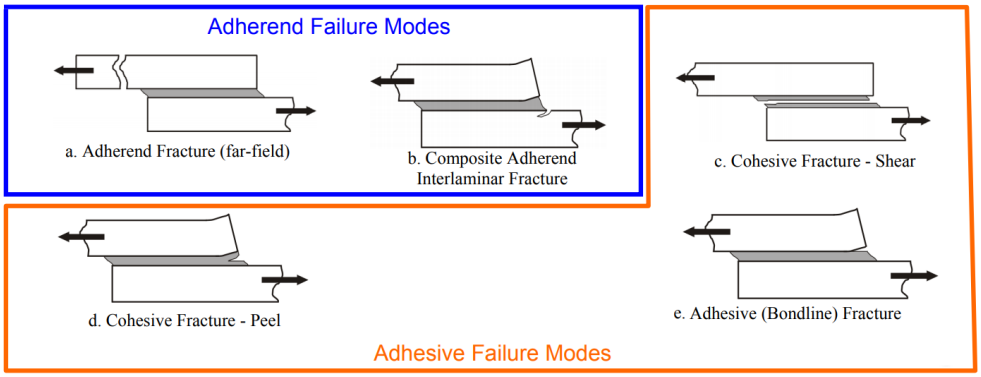

Fig. 2.5.: Failure modes in adhesively bonded joints [14].

At the microscopic level, the adhesive fails by the formation of a damage zone ahead of the crack tip [15]. The size and shape at the damage zone are quite changeable, depending on both the resin toughness and the stress state (mode I, mode II, mixed-mode I-II). There are three ways of applying a load to enable a crack to propagate, see Fig. 2.6:

Mode I: in this mode a tensile stress is generated and the cracks take a direction perpendicular to the plane of the adhesive.

Mode II: a shear is generated in the plane of the adhesive that follows the direction of the propagation and perpendicular to the crack front.

Mode III: a shear is generated in the plane of the adhesive that follows a perpendicular direction to that of the propagation and parallel to the crack front.

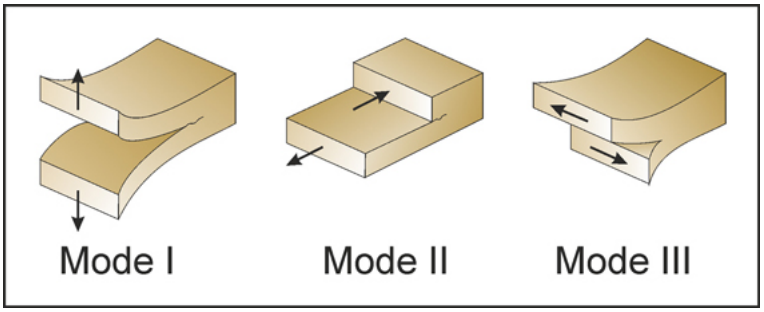

Fig. 2.6.: Mode I, mode II, and mode III crack propagation modes.

In adhesive joints with composite adherends, a combination of modes I and II, called mixed mode propagation I-II, is often produced. The damage zone ahead of the crack tip for mode II or mode III loading is larger than for mode I loading [16]. A much slower decaying of the stress field ahead of the crack tip for the shear modes of loading is responsible for this difference [16].

2.3 Effect of environmental conditions

The environmental conditions have a meaningful impact on the mechanical properties of bonded joints. The main environmental threats are related to the effect of temperature and moisture absorption (humidity) [3, 4] which can affect the strength and durability of the joints. Fig. 2.7 shows the main natural factors, such as: moisture, temperature, fire, UV (ultra violet) radiation, etc., which influence the durability of adhesively bonded joints. Only temperature and humidity are discussed in detail in the following subsections, as they are considered the most important.

2.3.1 Effect of moisture

The presence of moisture has been proven to cause significant degradation of the bonded joint strength [4, 17–21]. The adherends can absorb water from the environment during the manufacturing process, i.e. pre-bond moisture [22–25], or, during the service life, because the bonded joint will be exposed to different environmental conditions picking up moisture. Fig. 2.8 shows the moisture absorption locations and mechanisms in fiber reinforced polymer (FRP) composites [26]. Whichever the case, the humidity can linger in the composite for years.

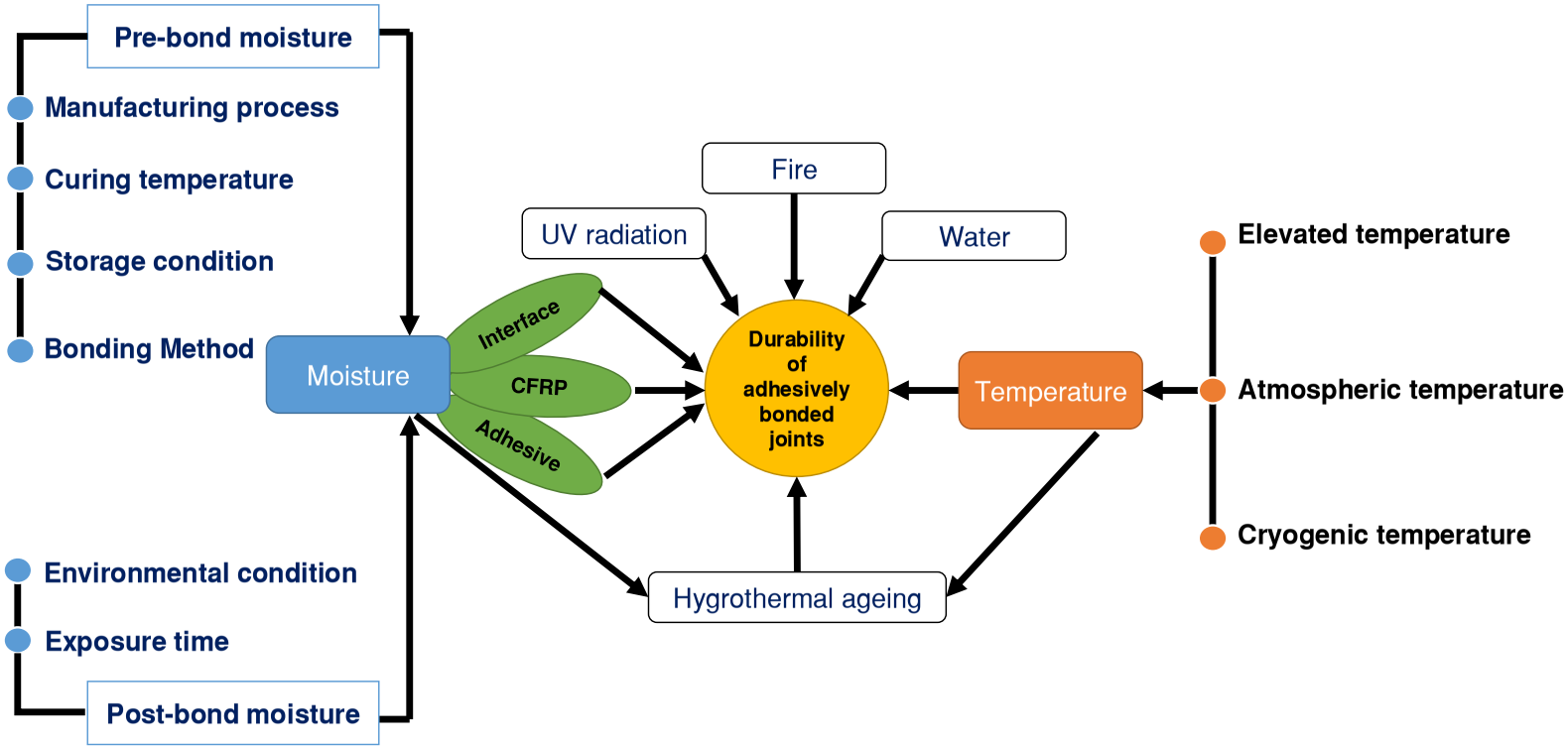

Fig. 2.7.: Diagram of environmental parameters influencing the durability of adhesively bonded joints [7].

The moisture absorbed in a polymeric material can lead to a wide range of effects, both reversible and irreversible, including plasticization, swelling, and degradation. Furthermore, the existence of moisture in bonded joints may affect the interface between the adherend and the adhesive in addition to the physical and chemical properties of the adhesive itself [6].

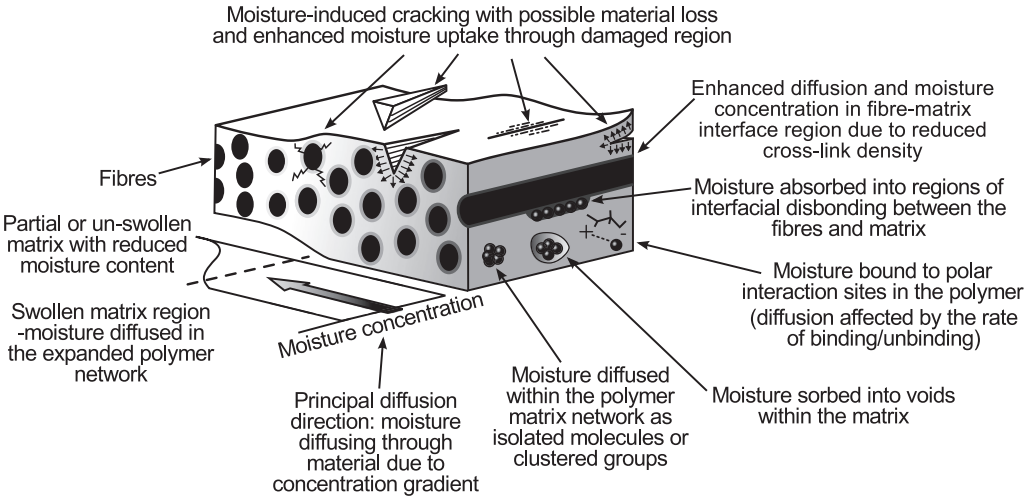

Fig. 2.8.: Summary of moisture sorption locations and mechanisms [26].

There are many works that investigate the effect of moisture on the strength of bonded joints [17–21]. Heshmati et al. [27] summarized the effect of the presence of moisture on the strength of adhesively bonded FRP/steel joints exposed to different moisture and temperature conditions, where the strength values are normalized regarding the average strength of the unaged joints, as shown in Fig. 2.9. In all cases, the strength of the joints degraded with the exposure time.

Some studies have been found to investigate the fracture behaviour analysis of composites exposed to different environmental conditions. However, these studies focus on the investigation of specimens exposed to an ageing process for a time less than one year. Fernandes et al. [4] studied the effect of the relative humidity on the fracture response of composite bonded joints made with carbon-epoxy laminate and structural adhesive (Araldite 2015) using the double cantilever beam test. The specimens were subjected to ageing conditions (55% and 75% of relative humidity (RH) and immersion in distilled water (IW)) for four months. They found that increasing the relative humidity between 55% and 75% has a sparse effect on the fracture response, while a substantial reduction occurs for immersed specimens. Moreover, the increase of the relative humidity causes an increase in the brittleness.

LaPlante and Lee-Sullivan [28] investigated the behaviour of cured FM300 epoxy exposed to partial and full moisture saturation. They noticed that as the moisture content increased the fracture toughness decreased. Katnam et al. [29] observed

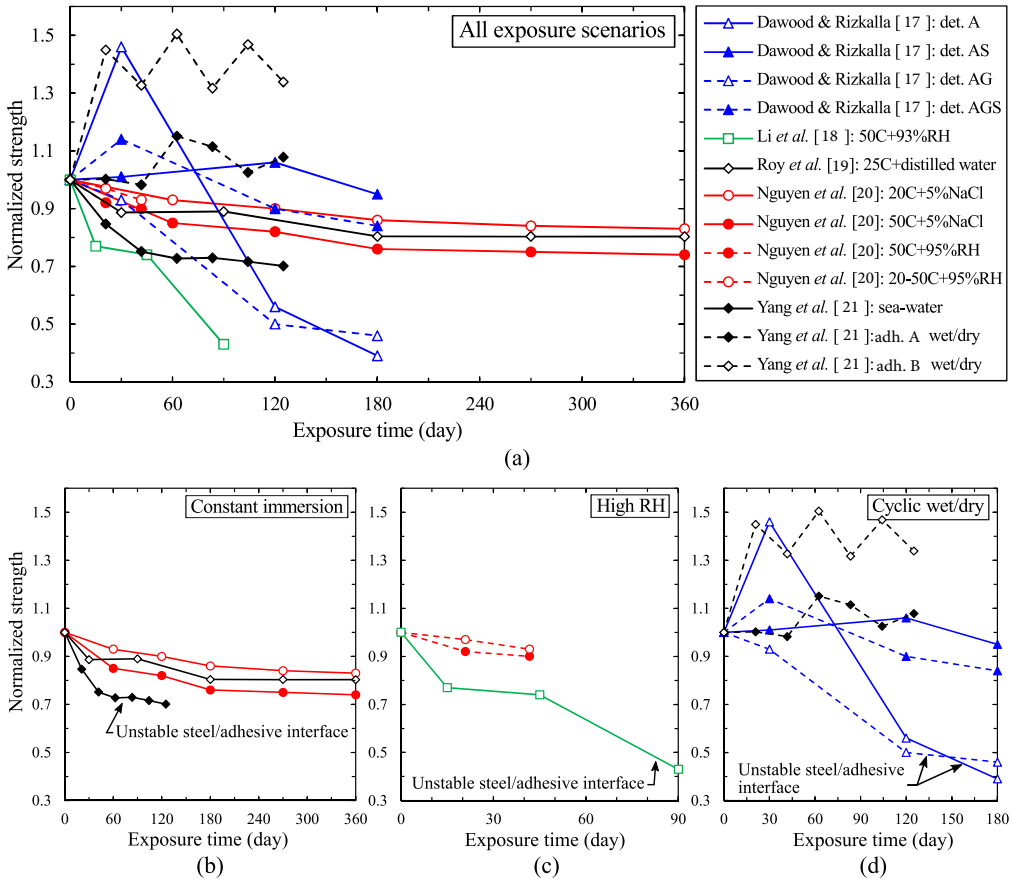

Fig. 2.9.: Comparison of strength variation in bonded FRP/steel joints with increasing exposure duration in moist conditions [27]. The details A, AS, AG and AGS found in [17], refer to the adhesive interface components (A: adhesive, S: Silane and G: glass fibre embedded in the adhesive).

that the fracture energy of adhesive FM73 immersed in de-ionised water at 50°C, decreased by about 16%. Alessi et al. [30] studied the influence of hydrothermal ageing conditioning on the fracture response of a carbon-epoxy laminate under mode I. They found that the fracture toughness of the tested specimens showed minimal variation with all ageing conditions. Arenas et al. [31] examined the fracture behaviour of aluminium-composite adhesive joints, subjected to water and motor oil, under mode II loading. The exposure to these environments caused a reduction in the failure load. Liljedahl et al. [32] investigated the effect of long-term durability on adhesively bonded of aluminium, composites and dissimilar substrates, subjected to different hygrothermal environments (80%RH and 70°C, 96%RH and 50°C, and immersion in de-ionised and tap water, both at 50°C). It is noticed that the failure load decreased with the increase of moisture content. Gledhill and Kinloch [33] studied the influence of water on structural adhesive/steel joints. They noticed a considerable reduction on the strength, especially for those joints exposed to high temperature.

2.3.2 Effect of temperature

One of the aerospace industry particular requirements is that adhesives have to withstand high temperatures keeping their structural integrity. The curing process, the coefficients of thermal expansion and changes of adhesive mechanical properties with temperature are the main factors that may affect the adhesive joint strength when subjected to different temperatures than the room temperature. The exposure to high temperatures affects both chemical and physical properties of the adhesive changing the bond strength [5]. Also the composite substrate itself may be affected by temperature changes. Coronado et al. [34] studied the fractography of specimens tested under temperature ranges from -60ºC to 90ºC, using a scanning electron microscope. Fig. 2.10 shows the obtained micrographs for each temperature. It is shown that the river markings, that separate the fibres, indicate the matrix brittleness in the case of low temperature while a ductile behaviour was noticed for testing at high temperature.

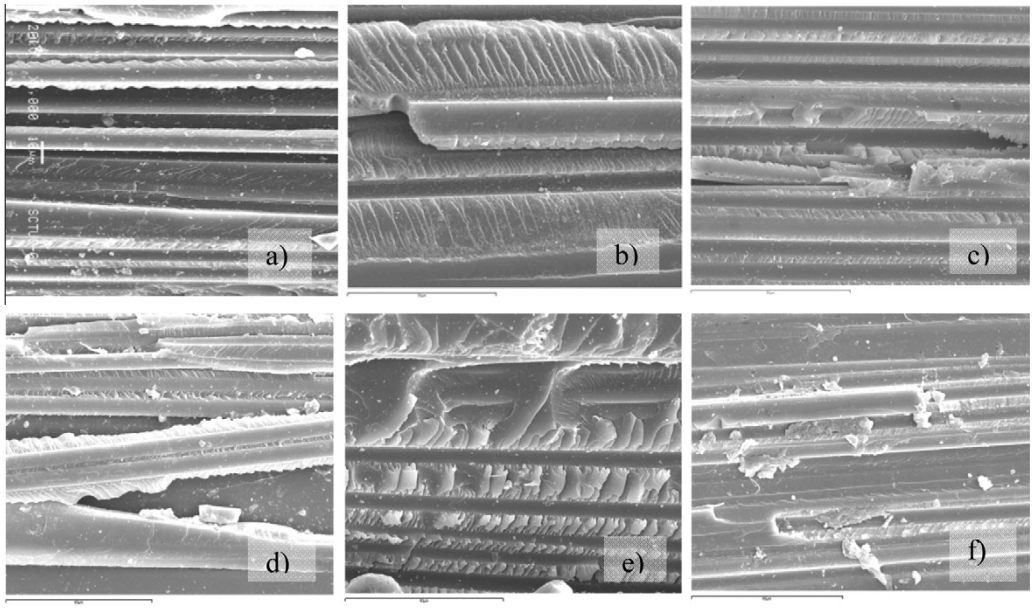

Fig. 2.10.: Fracture surface of fatigue tested AS4/3501 specimens: (a) 20 °C, (b) 50 °C, (c) 90 °C (d) 0 °C, (e) -30 °C and (f) -60 °C (×1000) [34].

High temperatures play a key role in decreasing the adhesive strength, also low temperatures because of high thermal stresses and the brittleness of the adhesive [35–37]. Banea et al. [38] studied the influence of the elevated temperature on the adhesive strength and fracture toughness of adhesive using two different test configurations, tensile and pure mode I double cantilever beam (DCB) tests. They tested specimens at room and high temperatures around the glass transition temperature (Tg) (100, 150 and 200°C). The temperature near the Tg monotonically decreases the ultimate stress. If the specimens are exposed to a temperature higher than Tg, the adhesive strength and the fracture toughness are significantly reduced [38, 39].

Charalambous et al. [40] tested asymmetric cut-ply coupons to characterise the temperature effects on the mixed-mode fracture toughness under selected temperature range (-50°C, room temperature, 50°C and 80°C). They found that testing at 80°C increased the ductility of the matrix that mainly leads to a major increase on the inter-laminar fracture toughness. On the other hand, testing at a temperature range of -50°C to 50°C has no significant effect on the material response.

Coronado et al. [41] studied the influence freezing temperatures have on the mode I fracture of two different epoxy resin matrix testing specimens at (-60°C, -30°C, 0°C and at room temperature) following different estimated in-flight aircraft temperatures. They found that the fracture toughness decreased with the temperature decrease. The XN1244 mechanical properties of the adhesive established by Banea et al. [42] show the effect of high temperature on the tensile strength. The tensile strength is decreased with temperature when the test was done with temperatures below Tg. Ojeda et al. [43] offered an excellent database of the most common adhesives used in aerospace structures including the variation of the bond strength and the adhesive modulus as a function of temperature. Hysol9394 or Hysol9360 are recommended for high-temperature applications whereas EC2216, Hysol9309.3 and Hysol9361 are useful for their use at low temperatures.

Banea and Silva [44] tested two different adhesives, Sikaflex 55 and room temperature vulcanising (RTV) silicon rubber, at temperatures ranging from -40 to 90°C and from -50 to 300°C, respectively. Regarding Sikaflex 55, the shear strength was slightly decreased by the temperature increase while the adhesive was stiffer with the temperature decrease. In the case of RTV adhesive, the increase of temperature until 300°C decreased the lap shear strength while the adhesive failed dramatically after this temperature.

Temperature not only affects the fracture toughness value but also affects the failure scenarios of adhesive joints. The failure scenarios of adhesive joints changed from brittle failure at low temperature to ductile failure at high temperature [36, 37, 45]. During the environmental conditioning, temperature played an important role in the degradation of the properties of the bonded joint [46].

2.3.3 Effect of combined moisture and temperature

Moisture absorption at elevated temperatures (hygrothermal ageing) is one of the common methods to accelerate ageing to predict the performance of composites exposed to environmental changes where the temperature is one of the driving factors for moisture absorption. The combined effect of moisture and temperature conditions is more damaging than the effect of each condition [7, 27]. Nevertheless, a limited number of studies focus on the fracture behaviour of adhesively bonded joints exposed to hygrothermal ageing. For example, the work presented in section 2.3.1

used different procedures to accelerate moisture absorption such as hydrothermal immersion or hygrothermal exposure.

Through the studies mentioned in section 2.3.1, the adhesive joints were exposed to hygrothermal or hydrothermal ageing for a time around a year. However, it is not known the behaviour of composites that are exposed to aggressive environmental conditions for a long time (e.g. the exposure to hygrothermal for more than one year).

2.4 Modeling of bonded joints

Adhesively bonded joints can be simulated using various finite element framework methodologies. Among them, the Virtual Crack Closure Technique (VCCT) and the Cohesive Zone Method are the ones that have enjoyed a greater success. The VCCT technique is based on Linear Elastic Fracture Mechanics (LEFM) and Irwin's hypotheses. It assumes that when a crack extends by a small quantity, the energy released in the process is equivalent to the work required to close the crack to its initial length [47]. The components of the energy release rate can be calculated from the nodal forces and displacements obtained from the solution of a finite element model [48]. Once the energy released per unit area reaches a critical value, the crack will propagate. Although the VCCT method allows the simulation of the separation of different interfaces, it has a few disadvantages. The method is based on LEFM and it can not be applied without a pre-existing initial crack to predict the onset of the crack front when the energy release rate reaches a critical value.

Under the framework of damage mechanics, another method to simulate adhesive interfaces is the CZM. It is based on the existence of a damaged region ahead of the crack tip instead of a sharp defect. The Cohesive Zone Model, first proposed by Dugdale [49] and Barenblatt [50], considers that closure stresses are present at the non-linear zone to represent the material resistance. Dugdale [49] assumed a constant cohesive stress distribution equal to the yield strength of the material σ_{ys} (Fig. 2.11-a) while Barenblatt [50] modelled the stress as a function $q(x)$ to represent the forces of the molecular cohesion (Fig. 2.11-b). In both models, the damaged region is of considerable size compared with the problem dimensions and it is called the Fracture Process Zone (FPZ).

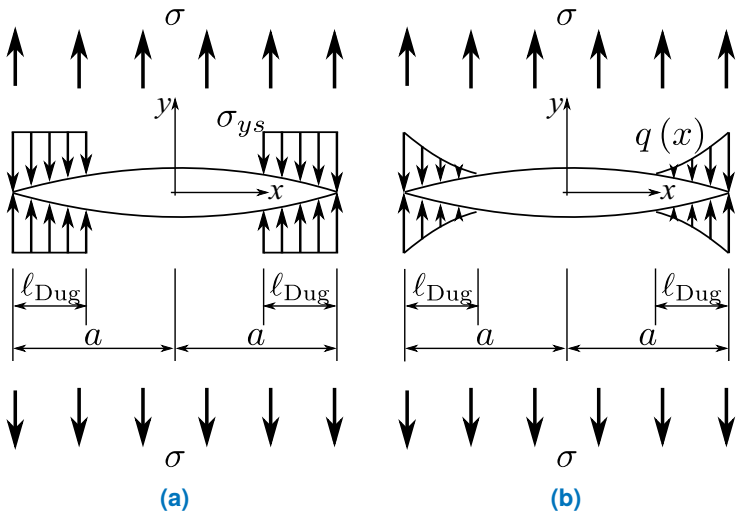

Fig. 2.11.: Dugdale's (a) and Barenblatt's (b) cohesive zone models.

Cohesive zone models are usually modelled with interface finite elements connecting plane or three-dimensional solid elements [51]. The interface elements should be placed at the interfaces where damage is prone to occur which means that critical regions must be identified in advance. In bonded joints, these regions can be identified as the interfaces between the adhesive and the adherends (in the case of an adhesive failure), as well as in the middle of the adhesive (in the case of a cohesive failure). Interface elements include a softening relationship between stresses and relative displacements at the interface (i.e. between the two element faces) in order to simulate a smooth degradation of the material properties. The cohesive elements have the advantage to predict both damage initiation and propagation without the requirement of an existing pre-crack.

Cohesive zone models relate the cohesive stress to the displacement jumps along a damage length at an interface where a crack may initiate. The cohesive law of the element governs the behaviour of the FPZ, where the damage initiates once the traction stress reaches the interfacial strength, while new crack surfaces are formed when the area under the traction-separation relation reaches a critical value equal to the fracture toughness. Generally, the interface properties are different for the three failure modes: mode I (in normal direction), mode II (in-plane direction) and mixed mode I-II, which need to be implemented to define the cohesive law for any value of the mixed-mode ratio.

Cohesive zone models have been proven to be an excellent approach to simulate adhesive bonded joints under a finite element framework. However, combining the environmental effects within the cohesive zone model is still an open issue. Moreover, the existing cohesive zone models, implemented in the commercial FE

program ABAQUS using user element subroutines, are formulated using various idealized shapes of cohesive laws, e.g. bilinear [15, 52], trapezoidal [53] and exponential [54], which require measuring more parameters from the experimental tests (see section 2.5) than only fracture toughness or the J-integral (see section 2.6). These shapes of the cohesive laws are too simple to model composite structures in the presence of a large FPZ due to plastic deformation or fibre bridging. This issue can be solved by making the shape of the cohesive law more complex. Recently, Jensen et al. [55] formulated a constitutive model of an interface in the commercial FE program ANSYS, as a multilinear cohesive law with an arbitrary number of line segments. In addition to the issues as mentioned above, the experimental determination of the cohesive law and its dependence on the environmental effects still has not been solved. The available methods to determine the cohesive laws experimentally or analytically are presented in section 2.7.

2.5 Experimental characterization of bonded Joints

In recent years, adhesively bonded joints have markedly raised their applicability in many applications, such as aircraft structures. For safety reasons, experimental characterization of the fracture behaviour of the different components of the structure is required, from a coupon level right through to a full-scale structure. Therefore, fracture toughness is one of the most relevant parameters used in the design and certification of composite structures.

Over the last few decades, the scientific community has developed many tests to study the fracture behaviour of bonded joints and delamination under different loading modes (mode I, mode II and mixed mode I-II). Concerning mode I, the DCB test is commonly used to characterize the fracture toughness under pure mode I which follows well-established standard test procedures and is universally accepted by the scientific community [56–58]. A schematic of the DCB test is shown in Fig. 2.12. The following notations are used in Fig. 2.12: δ is the displacement of the specimen at the loading point, L and 2L are the span length, the crack length is given by a, and the applied load is given by F. The single point loading condition of the DCB provides the ability to use a compliance calibration based data reduction procedure, which is preferred because these methods are based on LEFM assumptions and to avoid crack length measuring. However, most of the bonded joints have non-linear effects due to the formation of FPZ. Consequently, bonded joint analysis falls outside the scope of LEFM.

With regards to mode II, a large number of test configurations, Fig. 2.12, have been developed on the evaluation of mode II fracture resistance, such as: End Notched

Flexure (ENF) [59], End Loaded Split (ELS) [60], Cantilever Beam Enclosed Notch (CBEN) [61], Centre Notched Flexure (CNF) [62], Stabilized End Notched Flexure (SENF) [63], Transverse Crack Tension (TCT) [64], Curvature Driven Delamination (CDD) [65], four-point End Notched Flexure (4ENF) [66], or Compact Edge Notched Shear (CENS) [67]. Among all this tests, the ones that have enjoyed greater success are the ENF, SENF, ELS and 4ENF (Fig. 2.12). There is not an international consensus on how experimentally evaluate the mode II fracture resistance and only two standards, based on LEFM assumptions, have been developed: the ASTM D7905M [68] and the ISO15114 [69], the ENF and ELS test configurations respectively. Pérez-Galmés et al. [70] compared several mode II test methodologies (ELS, ENF, 4ENF and MMB) intending to obtain a reliable mode II fracture toughness test procedure for structural adhesives. The authors concluded that the ENF test is simple, but the propagation region must be large enough to allow the fracture process zone to fully develop while MMB and 4ENF tests are more complex and profoundly affected by the friction at the adhesive layer. From the experimental results, the authors [70] found that ELS test is the best candidate for testing adhesives as it provides stable and large propagation regions.

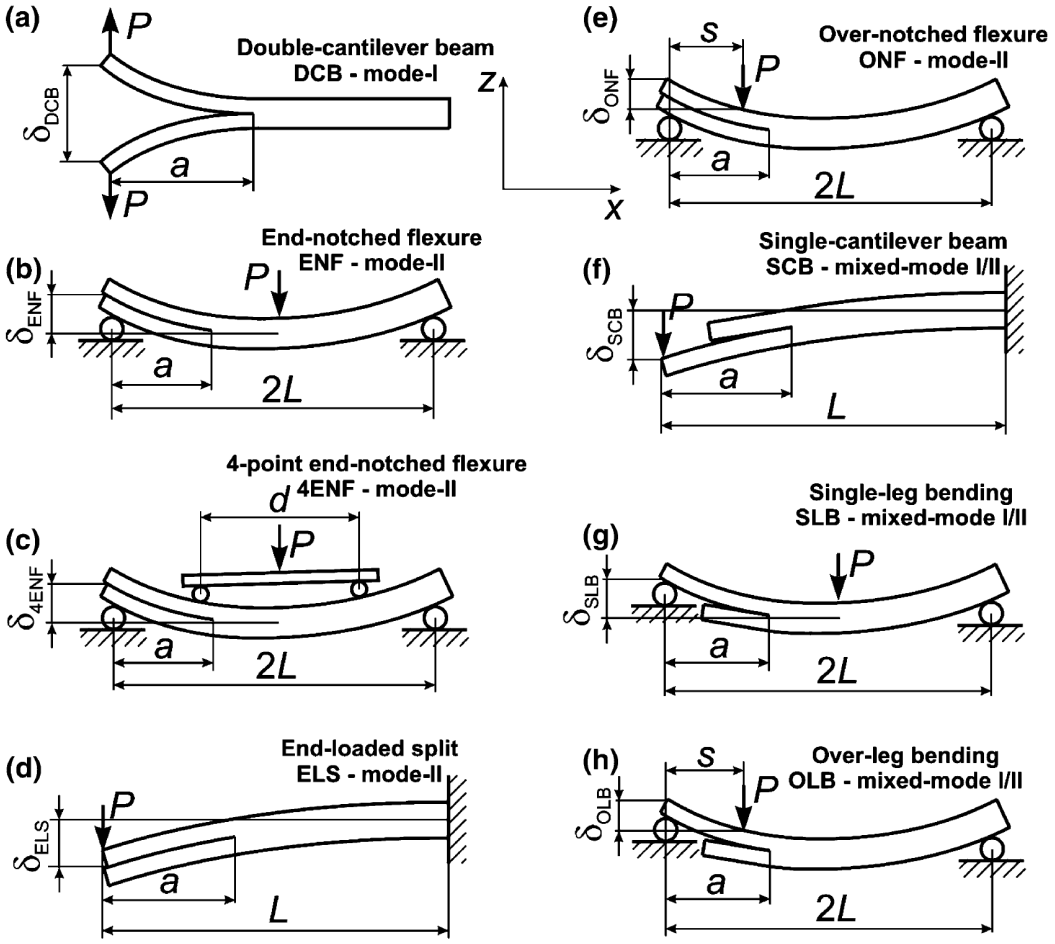

Fig. 2.12.: Schematic illustration of the DCB, ENF, 4ENF, ELS, ONF, SCB, SLB and OLB specimens [71].

2.6 Data reduction methods

This section describes the methods used to determine the fracture properties of bonded joints under Mode I and Mode II. Methods based on Linear Elastic Fracture Mechanics and methods based on the J-integral approach are presented.

2.6.1 Linear Elastic Fracture Mechanics

The fundamental hypothesis behind LEFM is that the nonlinear deformation at the crack front or FPZ is small in comparison to any of the dimensions of the specimen (width, thickness and crack length). The LEFM-based data reduction method has been extensively used in the characterization of delamination in FRP. However, the interlaminar fracture of adhesively bonded joints may involve large FPZs. In those cases involving large scale fracture, the use of an LEFM-based data reduction method for the fracture toughness characterization is fundamentally flawed.

Griffith [72, 73] introduced the theory of the energy balance between the elastic energy of the body and the potential energy release rate (ERR) available for an increment of crack surface extension, defined as $\mathcal{G}$. In common fracture toughness tests, the engineering approach for ERR expression reads:

$$\mathcal{G} = \frac{F^2}{2b}\frac{\partial C}{\partial a} \tag{2.1}$$

where F is the load, b is the specimen width, a is the crack length and C is the compliance (i.e. the ratio between deflection and applied load, U/F), which usually depends on the crack length. There are two main approaches to find this compliance. The first approach is the closed form solution provided by the Beam Theory (BT) approach that depends on the geometry of the specimen. The second approach is to measure the compliance through an additional experimental test (named as Compliance Calibration (CC) test).

Concerning bonded joints, and based on equation (2.1) the ISO25217 test standard describes two data reduction methods to obtain the mode I fracture toughness ($\mathcal{G}_{Ic}$) [57]: the Corrected Beam Theory (CBT) and the Experimental Compliance Method (ECM).

The Corrected Beam Theory data reduction method [57] leads to the following equation:

$$\mathcal{G}_{Ic} = \frac{3F\,U}{2b(a+|\Delta|)} \tag{2.2}$$

where F is the applied load, U the corresponding displacement, b the specimen width and a is the corrected crack length for crack tip rotation and deflection. Δ is the negative x-axis intercept of the compliance cubic root ($C^{1/3}$) versus the crack length (a) curve.

The Experimental Compliance Method [57] reads:

$$\mathcal{G}_{Ic} = \frac{n\,F\,U}{2b\,a} \tag{2.3}$$

where n is the slope of the logarithm of the compliance versus the logarithm of the crack length.

Another approach is the area method (AREA) proposed by Hashemi et al. [74] which based on the area under the load-displacement curve (i.e. total energy dissipated) with respect to the total amount of cracked area formation. The fracture toughness is obtained through the following equation [74]:

$$\mathcal{G}_{Ic} = \frac{A}{b\,\Delta a} \tag{2.4}$$

where Δa and b are the crack growth and the specimen width, respectively, while A is the dissipated area under the load-displacement curve.

Regarding Mode II, Pérez-Galmés et al. [70] summarized the most used data reduction methods for ENF and ELS tests, shown in Tables 2.1 and 2.2 respectively. The geometric parameters are the crack length (a), half span length (L), width (W) and half specimen thickness (H). The load is defined as P, the displacement as δ and E_{11} and G_{13} are the specimen longitudinal and shear modulus, respectively.

Tab. 2.1.: Summary of LEFM-based data reduction expressions used in the ENF test [70].

Method			Expression for fracture toughness	Ref.
Beam Theory (BT)	Classical Beam Theory (CBT)	Load	$\mathcal{G}_{IIc} = \frac{9P^2a^2}{16W^2H^3E_{11}}$	[75–78]
		Compliance	$\mathcal{G}_{IIc} = \frac{9P^2a^2C_0}{2W(2L^3+3a_0^3)}$	[76, 79, 80]
		Load-displacement	$\mathcal{G}_{IIc} = \frac{9P\delta a^2}{2W(2L^3+3a_0^3)}$	[78, 80–82]
	Modified Beam Theory (MBT)	Load[1]	$\mathcal{G}_{IIc} = \frac{9P^2(a+0.42\chi H)^2}{16W^2H^3E_{11}}F$	[74]
		Compliance	$\mathcal{G}_{IIc} = \frac{9P^2a_1^2C_1}{2W(2L^3+3a_1^3)}$	[83]
		Load-displacement[1]	$\mathcal{G}_{IIc} = \frac{9P\delta(a+0.42\chi H)^2}{2W(2L^3+3(a+0.42\chi H)^3)}F$	[74, 84]
	Timoshenko Beam theory (TBT)	Load	$\mathcal{G}_{IIc} = \frac{9P^2a^2}{16W^2H^3E_{11}}\left[1+0.2\frac{E_{11}}{G_{13}}\left(\frac{H}{a}\right)^2\right]$	[76, 77, 85]
		Load-compliance	$\mathcal{G}_{IIc} = \frac{9P^2a^2C_0}{2W(2L^3+3a^2)}\left[1+0.2\frac{E_{11}}{G_{13}}\left(\frac{H}{a}\right)^2\right]$	[77, 86]
	Corrected Beam Theory with Effective length(CBTE)		$\mathcal{G}_{IIc} = \frac{9P^2(a_e)^2}{16E_{11}W^2H^3}$; $a_e = \left(\frac{8E_{11}WH^3C_c}{3} - \frac{2L^3}{3}\right)^{1/3}$	[87–89]
	Modified Corrected Beam Theory with Effective length(MCBTE)[2]		$\mathcal{G}_{IIc} = \frac{9P^2(a^I)^2}{16E_{11}W^2H^3}$	[90]
	Beam Theory including Bending Rotation (BTBR)[2]		$\mathcal{G}_{IIc} = \frac{P^2(a^{II})^2}{16E_{11}W^2H^3}(1-\chi)$	[90]
Compliance Calibration (CC)	CC1	$\mathcal{G}_{IIc} = \frac{P^2}{2W}\frac{\partial C}{\partial a}\left\{\right.$	$C = C_\alpha + C_\beta a^3$	[76–79, 84, 91]
	CC2		$C = C_\alpha + C_\beta a + C_\gamma a^3$	[77, 84]
	CC3		$C = C_\alpha + C_\beta a + C_\gamma a^2 + C_\delta a^3$	[92, 93]
AREA			$\mathcal{G}_{IIc} = \frac{A10^6}{\Delta a W}$	[74]

[1] F is a correction for large displacements [74] and χ is a crack length correction.
[2] a^{II} and a^I are the crack length taking and without taking into account bending rotation effects, respectively [90].

Tab. 2.2.: Summary of LEFM-based data reduction expressions used in the ELS test [70].

Method		Expression for fracture toughness	Ref.
Beam Theory (BT)	Simple Beam Theory (SBT)[1]	$\mathcal{G}_{IIc} = \frac{9P^2a^2}{4W^2H^3E_{11}}F$	[69]
	Modified Beam Theory Load (MBT Load)	$\mathcal{G}_{IIc} = \frac{9P^2(a+\chi H)^2}{4W^2H^3E_{11}}$	[74, 89, 94]
	Modified Beam Theory Load-displacement (MBT Load-displacement)[1]	$\mathcal{G}_{IIc} = \frac{9P\delta(a+\chi H)^2}{2W[3N(a+\chi H)^3+(L+2\chi H)^3]}F$	[74]
	Corrected Beam Theory using Effective crack length (CBTE)[1,2]	$\mathcal{G}_{IIc} = \frac{9P^2a_e^2}{4W^2H^3E_{11}}F$; $a_e = \left(\frac{1}{3}\left(2WCH^3E_{11} - (L+\Delta_{clamp})^3\right)\right)^{1/3}$	[69, 87, 89, 95]
Compliance calibration (CC)	Compliance Based Beam Method (CBBM)[1]	$\mathcal{G}_{IIc} = \frac{9P^2C_{0c}}{2W(3a_0^3+L^3)}F\left[\frac{C_c}{C_{0c}}a_0^3 + \frac{L^3}{3}\left(\frac{C_c}{C_{0c}} - 1\right)\right]^{2/3}$	[89, 95, 96]
	Experimental Compliance Method (ECM)[1]	$\mathcal{G}_{IIc} = \frac{3P^2a^2m}{2W}$; $C = (C_0 + ma^3)/N$	[69, 87]
	Compliance Calibration Method (CCM)	$\mathcal{G}_{IIc} = \frac{P^2}{2W}\frac{\partial C}{\partial a}$; $C = C_\alpha + C_\beta a^3$	[89]
AREA		$\mathcal{G}_{IIc} = \frac{A10^6}{\Delta aW}$	[74, 87, 97]

[1] Correction factors for large displacements (F) and load-block effects (N) from [69]
[2] Clamp correction, Δ_{clamp}, according to [69].

2.6.2 J-integral approach

The LEFM definition of the Energy Release Rate assumes the existence of a sharp crack. Within the framework of a cohesive zone model, the crack length loses its definition, due to the existence of the FPZ.

An alternative to measuring the energy dissipated inside the FPZ was proposed by Rice [98]. The J-integral is defined as a path-independent contour integral that can be interpreted as a non-linear energy release rate. In the particular case of two-dimensional elastic problem, the J-integral is defined as:

$$J = \int_{\Gamma}(\Phi dx_1 - t_i\frac{\partial u_i}{\partial x_2}ds) \tag{2.5}$$

where J is the energy being dissipated at a given instant inside the FPZ, Φ is the elastic strain density, t_i is the surface traction vector and u_i is the displacement vector. ds is the length increment along the contour path Γ. The surface traction vector is obtained as $t_i = \sigma_{ij}n_j$, where n_j is a unitary vector normal to the path Γ and σ_{ij} is the stress tensor.

Many methods for characterizing the non-linear FPZ based on the J-integral originally defined by Rice [98] have been developed recently for the different fracture tests defined in Table 2.3. Paris and Paris [99] derived the energy release rate for the DCB-specimen using the J-integral based on the work introduced by Rice [98]. Stigh

et al. [100] used the J-integral to develop a method to obtain fracture toughness closed-form solutions for ENF tests. Pérez-Galmés et al. [101] used a closed-form J-integral solution for the ELS test that considers large displacements. Moreover, Pérez-Galmés et al. [70] applied the aforementioned J-integral methods to compare the results of the mode II tests (ELS, ENF, 4ENF, and MMB). Table 2.3 summarizes the J-integral data reduction methods that require measuring the rotation angles (θ) at the load introduction points and at the supports for the DCB, ELS and ENF tests. E is the Young's modulus of the adherends in the fibre direction and G_{12} is the shear modulus,

Tab. 2.3.: Summary of J-integral data reduction methods for the DCB, ELS and ENF tests.

Test method	Expression for the J-integral	Ref.
Mode I, DCB	$J = \frac{2P}{W}\theta$	[99]
Mode II, ENF	$J = \frac{P}{2W}(\theta_1 - 2\theta_2 + \theta_3)$	[100]
Mode II, ELS[1]	$J_{II} = \frac{3}{5}\frac{P^2}{G_{12}W^2H} + \frac{P}{W}(\tan\theta_P - \tan\theta_S) - \frac{EH}{3}\left(\frac{3}{2}\frac{P(L-L_S)}{EWH^2}\right)^2$	[101]

* All the rotations θ_n are arranged from the left to the right, Fig. 2.12.

[1] L is the distance between the load application point, and the clamp tool and L_S is the distance between the clamp tool and a section called $S - S'$ where the rotation θ_S is measured, found in [101].

2.7 Experimental methods to obtain the cohesive laws

Over the last years, many idealised shapes of cohesive law (e.g. linear, bilinear, trapezoidal, parabolic and exponential) have been used to simulate fracture in interfaces using parameters that have been obtained experimentally or numerically [102–104], Fig. 2.13. Campilho et al. [105] showed the great influence the cohesive law shape has on the loading response of ductile interfaces, while it can be ignored for brittle ones. In ductile interfaces, such as in bonded joints, the limiting maximum stress σ^0 does not affect the propagation energy but has a great effect on the initial part of loading response while the fracture process zone is formed. Blackman et al. [106] investigated the use of cohesive zone models using different bonded joint configurations to clarify the influence of maximum traction stress on the loading response. As a result, they obtained different initial responses in the load-displacement curves depending on that parameter. During the fracture process zone formation, most of the bonded joints have a non-linear loading response [107–110], not only in 2D but also in 3D (e.g. the finite width of the specimen have a significant effect on the calculation of the deflection and energy release rate values [111], and the shape of crack front affects the response [112, 113]).

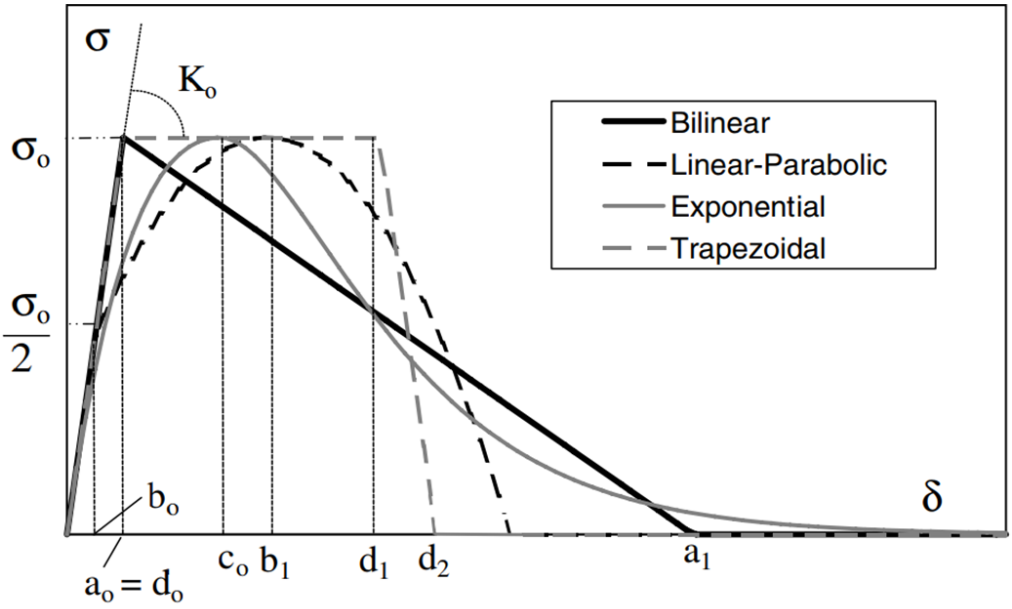

Fig. 2.13.: Idealised shapes of cohesive law.

Measuring the cohesive law experimentally is not straightforward. Different methods have been developed to experimentally determine the cohesive law by measuring the crack tip opening displacement together with the J-integral [114–116]. With regards to mode-I, Sørensen [114] proposed a technique to estimate the cohesive law using the J-integral and measuring the opening displacement at the crack tip. Meanwhile, Andersson and Stigh [117] used the equilibrium of energetic forces acting on a DCB specimen as an experimental method to determine the cohesive law. Leffler et al. [118] determined the adhesive layer shear characteristics based on the work introduced by Andersson and Stigh [117] and derived the energy release rate for the ENF-specimen relation using the J-integral. Stigh et al. [119] proposed the J-integral technique to estimate the shear strength of adhesive layers. In addition, the shape of the cohesive law can be defined using the J-integral technique with the displacement jumps. Fernandes et al. [120] studied the interaction between cohesive zone model and J-integral technique in predicting the experimental behaviour of the ENF tests.

Meanwhile, different methods have been used to capture the crack opening displacement. For example, Stigh et al. [100] measured the opening displacement with a linear variable differential transducer (LVDT). In subsequent works, Walander et al. [121, 122] studied the fracture behaviour of epoxy adhesives using an LVDT to measure the crack tip opening displacement as shown in Fig. 2.14.

Another alternative is to use the 3D Digital Image Correlation (DIC) technique together with J-integral to measure the cohesive laws [123–125]. Fig. 2.15 shows a test setup using the DIC technique. Sarrado et al. [123] used the DIC to capture the

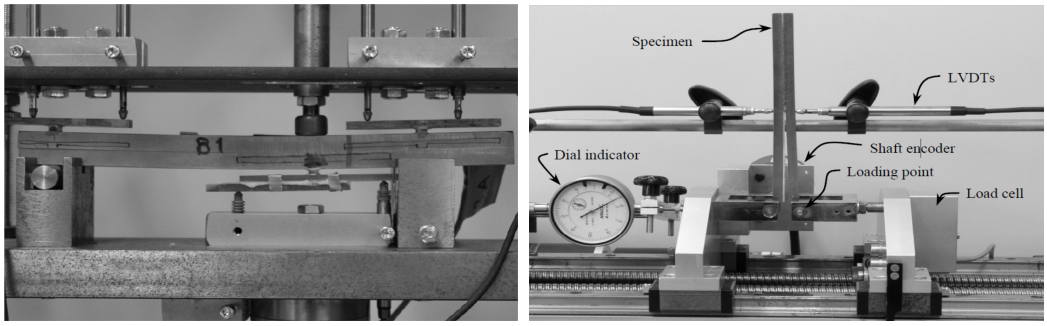

(a) (b)

Fig. 2.14.: (a) ENF and (b) DCB test setup [121] .

displacement jumps within the fracture process zone for DCB, ENF and MMB test specimens from pictures taken at the side of the specimen.

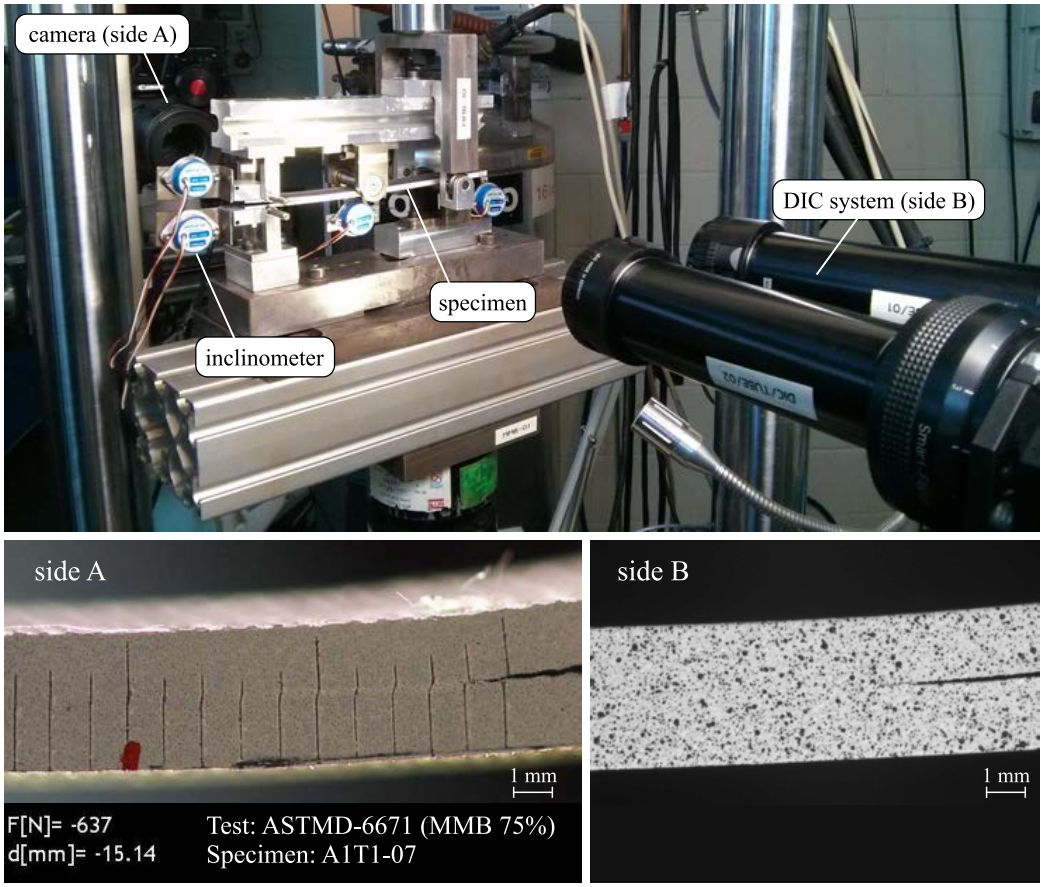

Fig. 2.15.: Experimental setup for an MMB test [123].

The aforementioned techniques require very high resolution equipment to capture the opening displacements, regardless of the method used, e.g. extensometers or DIC. Moreover, the cohesive law can only be estimated during the formation of the fracture process zone. Apart from this, DIC is very expensive and time consuming,

and the crack tip opening displacement can be extremely difficult to measure in specimens tested in an environmental chamber, e.g. tests at high or cryogenic temperatures.

As an alternative to the aforementioned methodologies, Sorensen et al. [126] postulated an inverse numerical technique based on the experimental measurement of crack opening displacement and the energy release rate. The traction-separation law for large-scale bridging has been obtained using an inverse method based on strain data [126, 127]. Donough et al. [128] derived an inverse method assuming an exponential cohesive law using an optimization technique and crack opening displacements. Meanwhile, Arrese et al. [129] presented an analytical method to determine the cohesive law in Mode I from the load-displacement curve; a method based on estimating an effective crack length by taking into account a beam on elastic foundation problem. Pereira et al. [130] performed an inverse procedure using finite element analysis including CZM with an optimization algorithm to determine the mode I cohesive law without a pre-defined shape. This method requires the load-displacement curve and the relation between the strain energy release rate with the equivalent crack length. Consequently, the cohesive law can be determined by minimizing the difference between the numerical and the experimental load-displacement curves. Upadhyaya et al. [131] proposed a numerical–experimental methodology to determine cohesive stresses using the J-integral approach and presented a cohesive layer FEA model to capture the load-displacement curve for known damage parameters. Massabò et al. [132] proposed methods to obtain the bridging laws for mode II in the delamination cracks using the hypothesis of superposition. Wang and Qiao [133] used this hypothesis to analyse the ENF specimen by dividing the problem into two sub-problems: the first being an un-cracked beam under three-point bending, and the second a beam with a mid-plane crack at one end, both of which can be solved by Timoshenko's beam theory [133]. They obtained closed-form equations for the compliance and the fracture toughness of the ENF specimen, however, these equations require measuring the crack length. Arrese et al. [134] presented an analytical approach to define the cohesive law based on determining an effective crack length by taking into account a beam in an elastic foundation problem. Azevedo et al. [135] used an inverse methodology to obtain a triangular cohesive law for adhesive joints where a curve fitting procedure was carried out knowing the G_{IIc} value that can be calculated by the beam theory.

Towards an analytical method to obtain the cohesive laws

Although the methods mentioned above are good alternatives for the direct experimental methods, the majority of the methods still required the opening displacement

to be measured experimentally while the others depend on LEFM assumptions. Consequently, a non-LEFM method that does not require additional measurements rather than the load-displacement curve is required.

Maimí et al. [136] used the Strip Yield Model with a constant characteristic length to obtain the global response of a nonlinear problem, using the superposition of the acting loads on a specimen, as shown in Fig. 2.16.

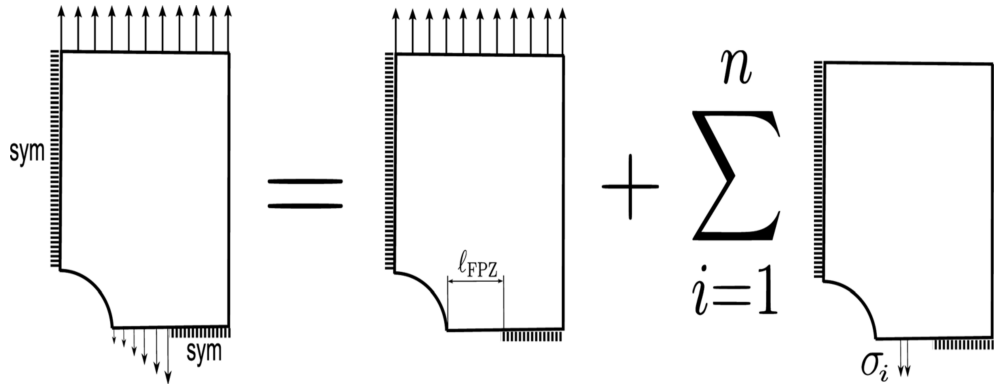

Fig. 2.16.: Strip yield model for the open hole specimen [136].

Dugdale [49] considered that singular stresses cannot be present in the complete model, the stress singularity at the crack tip must be null where the cohesive forces cancel the action of the remote stress at the crack tip. The Dugdale finite stress condition is defined as:

$$K^R + K^{\sigma_c} = 0 \tag{2.6}$$

where K^R is the stress intensity factor (SIF) caused by the remote stress and K^{σ_c} the SIF caused by the cohesive stress at the FPZ. If the cohesive stress profile inside the FPZ is known, there is only one value for the load that satisfies Equation 2.6. Although σ_c is unknown and may change during the FPZ development, it can be discretized as a series of small constant stresses of value equal to σ_i applied at the crack surface. It is possible to express the set of openings δ_i as a superposition of the openings due to each load [136, 137]:

$$\delta_i = \delta_i^R + \delta_i^{\sigma_c} \tag{2.7}$$

where δ_i is the total crack opening displacement. δ_i^R and $\delta_i^{\sigma_c}$ are the crack opening due to the remote stress and the crack openings caused by the cohesive stress profile σ_c, respectively. The solution of Equation 2.7 is obtained from an iterative process and for a given Cohesive Law (CL). Ortega et al. [138] used the solution presented

by Maimí et al. [136], based on the superposition of the problem due to the acting loads as shown in Fig. 2.17, to obtain the translaminar fracture toughness of the compact tension specimens under Mode I using an iterative methodology to obtain the cohesive law for an experimental load-displacement curve.

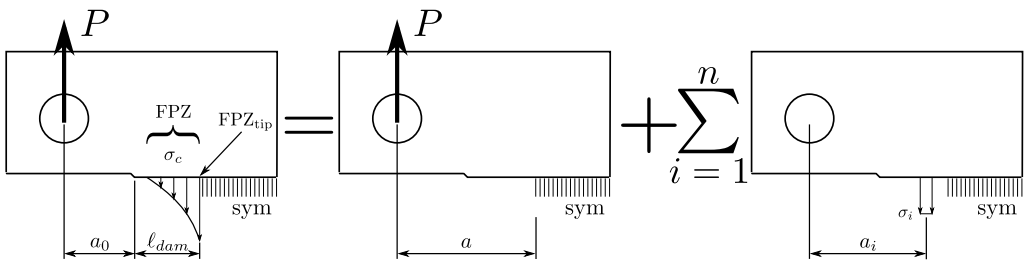

Fig. 2.17.: Compact Tension specimen with a FPZ expressed as a superposition of linear problems [138].

Part I

Methodology to obtain cohesive laws

3 An efficient method to extract a Mode I cohesive law

3.1 Introduction

In this chapter, a new method based on Dugdale's condition [49, 139] is presented to obtain the cohesive laws in DCB specimens from the load-displacement curve only. The model is an extension of the approach developed by Ortega et al. [138] for compact tension specimens. The work consists of four steps: (I) the definition of a direct method to obtain the load-displacement curve from a cohesive law, (II) the validation of the direct and inverse methods with both the LEFM and finite element models, (III) the implementation of an inverse method to obtain the cohesive law from the load-displacement curve, and (IV) the validation of the methodology using the results obtained from previous work [123, 129].

3.2 A direct method based on Dugdale's condition to obtain the load-displacement curve

A DCB specimen, shown in Fig. 3.1, is subjected to a controlled displacement (U) and the corresponding load (F) applied to the upper adherend, meanwhile the other adherend is pinned to the ground. DCB refers to the specimen geometry and not the data reduction found in standards. A study region L_{std}, which embeds a damage zone of length $L_{dam} \leq L_{std}$ is defined. The length L_{dam} is the damaged length of the material, measured from a_0, and combines the FPZ and the traction-free crack surface length, as shown in Fig. 3.1.

To generalize the analysis, the DCB specimen is replaced with an equivalent specimen which has a shorter crack length of 10 times the arm thickness h, to avoid stress singularities at the boundaries, using an additional bending moment (M) to substitute the difference in crack length (x), see Fig. 3.1. The model considers a 2D plane strain problem where the material response lies on the bondline, cohesive failure occurs during crack formation and propagation, there is no effect of the loading system and the adherends deform linear-elastically. Furthermore, the only source of nonlinearity in load-displacement is the interface response.

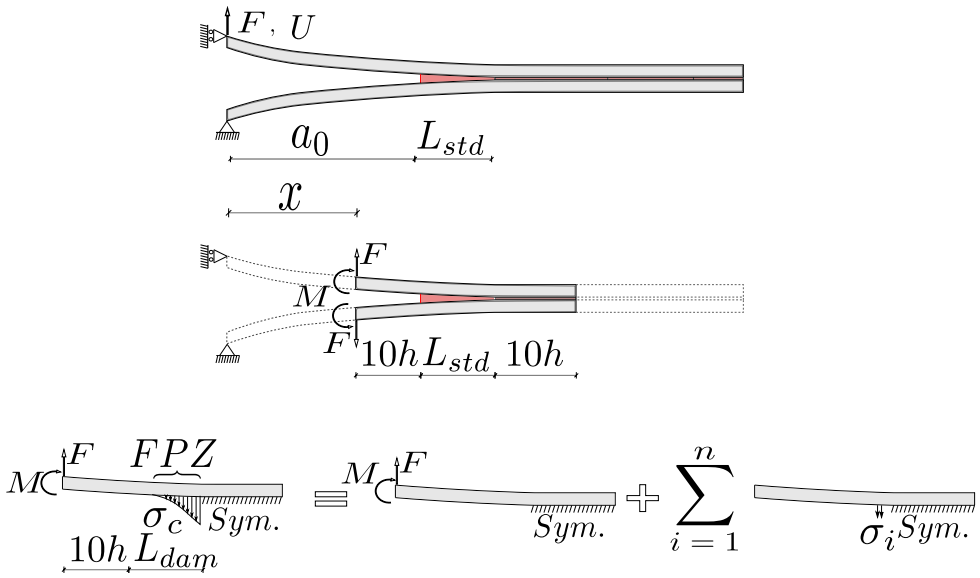

Fig. 3.1.: DCB specimen expressed as a superposition of acting loads.

Dugdale's condition [49, 139] postulates that in the presence of a cohesive zone ahead of a crack tip, the overall stress intensity factor (SIF) vanishes, i.e. the singularity caused by the external loads ($K^F + K^M$) is cancelled by the singularity caused by the cohesive stress (K^{σ_c}). In the case of an equivalent DCB specimen and using the superposition method, this condition reads:

$$K^F + K^M + K^{\sigma_c} = 0 \tag{3.1}$$

where K^F and K^M are the stress intensity factors for the acting loads F and M, respectively, ($M = Fx$). K^{σ_c} is the stress intensity factor caused by the whole cohesive stress (σ_c) profile at L_{dam}, see Fig. 3.1. These stress intensity factors are defined as:

$$K^F = \frac{F}{b\sqrt{h}}\hat{K}^F \tag{3.2}$$

$$K^M = \frac{F\hat{x}}{b\sqrt{h}}\hat{K}^M \tag{3.3}$$

$$K^{\sigma_c} = \sigma_i\sqrt{h}\hat{K}_i^{\sigma} \tag{3.4}$$

where h and b are the arm thickness and width of the specimen, respectively. $\hat{K}^F$ and $\hat{K}^M$ are the non-dimensional forms of the applied load stress intensity factors, and $\hat{K}_i^\sigma$ is the non-dimensional form of the SIF due to a unitary cohesive stress σ_i at position i of L_{dam}. The non-dimensional parameter $\hat{x} = x/h$. The non-linear problem expressed as a superposition of linear problems [138] is shown in Fig. 3.1.

The applied load F can be obtained by substituting Equations (3.2, 3.3 and 3.4) into Equation (3.1) :

$$F = \beta_i \sigma_i b h \tag{3.5}$$

where β_i is a vector that stores the stress relationships at each location of L_{dam}:

$$\beta_i = \frac{\hat{K}_i^\sigma}{\hat{K}^F + \hat{K}^M \hat{x}} \tag{3.6}$$

The opening displacements at L_{dam} can be defined using the superposition:

$$\delta_i = \delta_i^F + \delta_i^M + \delta_i^{\sigma_c} \tag{3.7}$$

where δ_i is the total opening displacement at position i of L_{dam}, δ_i^F is the opening displacement vector due to load F, δ_i^M is the opening displacement vector due to M and $\delta_i^{\sigma_c}$ is the opening displacement vector due to the stress profile σ_c. These parameters can be defined as:

$$\delta_i^F = \frac{F\hat{a}^3}{Eb}\hat{\delta}_i^F \tag{3.8}$$

$$\delta_i^M = \frac{F\hat{x}\hat{a}^3}{Eb}\hat{\delta}_i^M \tag{3.9}$$

$$\delta_i^{\sigma_c} = \frac{\sigma_j h \hat{a}^3}{E}\hat{\delta}_{ij}^\sigma \tag{3.10}$$

where E is the Young's modulus of the adherends in the longitudinal direction and $\hat{a} = a_0/h$. $\hat{\delta}_i^F$ and $\hat{\delta}_i^M$ are the non-dimensional displacements of δ_i^F and δ_i^M, respectively. $\hat{\delta}_{ij}^\sigma$ is the non-dimensional opening displacement at position i of L_{dam} when a unitary load σ_j is applied at position j of L_{dam}.

To this end, the total opening displacement is defined as a function of the cohesive stresses by substituting Equations (3.8, 3.9 and 3.10) into Equation (3.7):

$$\delta_i = f_{ij}\sigma_j \frac{h\hat{a}^3}{E} \tag{3.11}$$

where f_{ij} is expresed as:

$$f_{ij} = (\hat{\delta}_i^F + \hat{\delta}_i^M \hat{x})\beta_j + \hat{\delta}_{ij}^{\sigma} \tag{3.12}$$

In an analogous way, the total displacement at the loading application point of the whole DCB specimen can be obtained by superposition:

$$U = U^F + U^M + U^{\sigma_c} \tag{3.13}$$

where U is the total displacement at the loading application point of the whole DCB specimen, U^F and U^M are the displacements due to load F and momentum M, and U^{σ_c} is the displacement due to the stress profile σ_c at L_{dam}. These parameters can be defined as:

$$U^F = \hat{U}^F \frac{F}{Eb} \tag{3.14}$$

$$U^M = \hat{U}^M \frac{F\hat{x}}{Eb} + \frac{4F\hat{x}^3}{Eb} \tag{3.15}$$

$$U^{\sigma_c} = \hat{U}_i^{\sigma} \frac{h\sigma_i}{E} \tag{3.16}$$

where $\hat{U}^F$, $\hat{U}^M$ and $\hat{U}_i^{\sigma}$ are the non-dimensional displacements of U^F, U^M and U^{σ_c} respectively, reading:

$$\hat{U}^F = \hat{u}^F + \hat{\theta}^F \hat{x} \tag{3.17}$$

$$\hat{U}^M = \hat{u}^M + \hat{\theta}^M \hat{x} \tag{3.18}$$

$$\hat{U}_i^{\sigma} = \hat{u}_i^{\sigma} + \hat{\theta}_i^{\sigma} \hat{x} \tag{3.19}$$

where $\hat{u}^F$, $\hat{u}^M$, $\hat{\theta}^F$ and $\hat{\theta}^M$ are the non-dimensional vertical displacements and rotations at the left end of the equivalent beam when a unitary load or a unitary momentum is applied, respectively. $\hat{u}_i^\sigma$ and $\hat{\theta}_i^\sigma$ are the non-dimensional vertical displacements and rotations at the left end of the equivalent beam when a unitary load σ_i is applied at position i of L_{dam}.

Taking into account Equation (3.5), the total vertical displacement at the load application point can be expressed as a function of the stress profile at L_{dam}:

$$U = \gamma_i \frac{h\sigma_i}{E} \tag{3.20}$$

where:

$$\gamma_i = (\hat{U}^F + \hat{U}^M \hat{x} + 4\hat{x}^3)\beta_i + \hat{U}_i^{\sigma_c} \tag{3.21}$$

Therefore, if σ_i is known, with Equations (3.5 and 3.20) it is possible to obtain load F and displacement U. To obtain σ_i we use the constitutive relationship between the displacements δ_i and the stresses σ_i, expressed by a cohesive law. Additionally, δ_i and σ_i have to satisfy the geometrical relationship defined in Equation (3.11). For a given cohesive law, the procedure to obtain the total displacement U and the load F at the loading application point is summarized in Algorithm 1.

Algorithm 1 Direct method work-flow

Input: Cohesive law (CL)
Output: Load-displacement curve

```
Select an initial damage length L_dam
while L_dam ≤ L_std do
    Assume a constant cohesive stress (σ_c) profile equal to the adhesive traction-separation strength σ^0
    while error > tolerance do
        Calculate the opening displacements using Equation (3.11)
        Update stresses using opening displacements calculated and the CL
        Compute the error between the displacements computed with Equation (3.11) and those computed with the defined CL
    end while
    Calculate F and U using Equations (3.5 and 3.20), respectively
    Increase L_dam
end while
```

To obtain the non-dimensional parameters ($\hat{K}^F$, $\hat{K}^M$, $\hat{K}_i^\sigma$, $\hat{\delta}_i^F$, $\hat{\delta}_i^M$, $\hat{\delta}_{ij}^\sigma$, $\hat{u}_i^F$, $\hat{u}_i^M$, $\hat{u}_i^\sigma$, $\hat{\theta}_i^F$, $\hat{\theta}_i^M$ and $\hat{\theta}_i^\sigma$) the procedure shown in Appendix A is followed.

3.3 Inverse Method to obtain the cohesive law

The cohesive law is measured during FPZ development [138]. Fig. 3.2 shows four instants of this development (named I, II, III and IV). The FPZ is initiated when the stress at the crack tip reaches the strength of the traction separation interface, σ^0. It grows as the displacement is increased, opening the cohesive interface and changing the cohesive stress profile in relation to the CL (instants I and II). When the crack tip reaches the critical opening displacement, δ^c, the FPZ ends its development (instant III). Beyond this point, and if the displacement continues increasing, the process is assumed to enter a steady-state, where the FPZ moves along the crack path (instant IV).

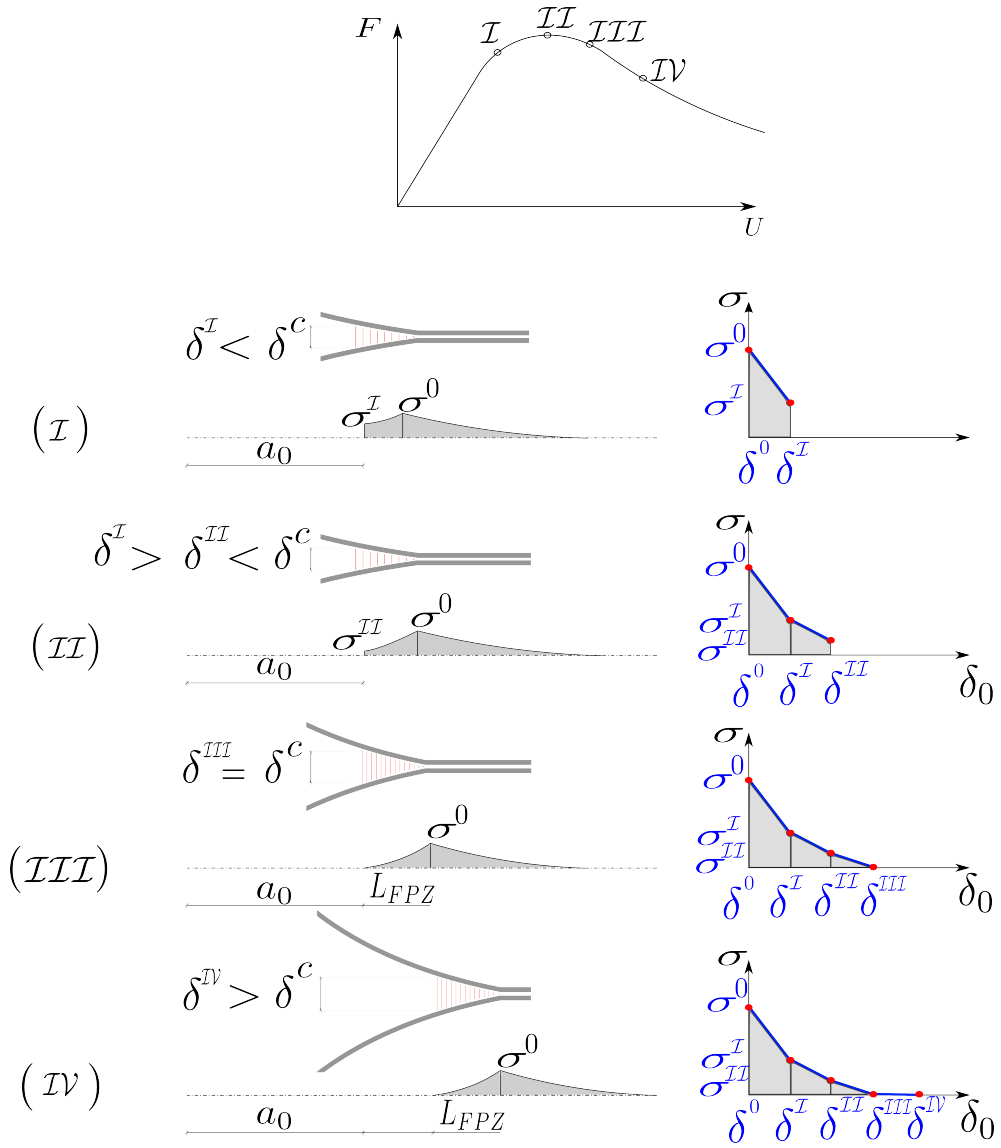

Fig. 3.2.: Damage development and FPZ formation in a DCB test after crack initiation: (I) the FPZ is partially developed; (II) the FPZ increases; (III) the FPZ is fully developed; (IV) crack propagation.

The relationship of the FPZ growth with the CL is shown in Fig. 3.2 for instants I, II, III and IV. At point I of the load displacement curve, the cohesive stresses range from σ^0 to σ^I, with the crack opening being δ^I. Therefore, as stated by Ortega et al. [138], only a part of the CL needs to be known for instant I. At point II, the cohesive crack opening at a_0 increases to δ^{II} whereas the cohesive stress decreases to σ^{II}, therefore to represent instant II the CL must be known until $\delta^{II} - \sigma^{II}$. The same applied for every displacement increase until point IV.

Consequently, each point of the load-displacement curve is observed as having a unique corresponding FPZ state. This property allows a piece-wise CL to be defined by fitting consecutive points into the load-displacement curve. The inverse method takes advantage of the progressive FPZ development process to determine the CL.

First of all, n experimental points from a load-displacement curve are selected in such a way that the first point is the end of the linear part of the load-displacement curve, and the last point is when crack propagation starts (point III of Figure 3.2). For each segment, formed by two consecutive experimental points, an increment of the cohesive law is determined. This adjustment is iteratively done by applying the Direct Method [138]. A step-by-step algorithm to solve the inverse problem is shown in Algorithm 2. Three alternative methods are presented, depending on the initial known variables: (i) cohesive strength (σ^0); (ii) fracture toughness ($\mathcal{G}_{Ic}$), or (iii) neither of them. Table 3.1 indicates the initialization and the definition of the CL in each case.

Algorithm 2 Inverse method work-flow

Input: n experimental points $F_i(U_i)$, arranged as $u_i < u_{i+1}$ + additional input parameter, see Table 3.1
Output: Cohesive Law CL

```
Initialization, see Table 3.1
for i = 1 : n do
    Assume H^i (slope of the CL) or σ^i, see Table 3.1
    while error > tolerance do
        Define a segment of the CL between points i − 1 and i, see Table 3.1
        Compute load displacement curve with Algorithm 1
        At U_i compute the error between P_i experimental and numerical
        if error > tolerance then
            Change H^i or σ^i, see Table 3.1
        end if
    end while
end for
```

The first approach is directly derived from the work of Ortega et al. [138] and depends on knowing a value of σ^0 prior to the test. This value can be determined from a complementary test [140]. The second approach assumes that the fracture toughness is known, in that the measurement of $\mathcal{G}_{Ic}$ is very standardized and can

Tab. 3.1.: Required parameters for the implementation of each alternative.

Alternative	Input	Step 1	Step 3	Step 5	Step 9
(i)	σ^0	$\sigma_0 = \sigma^0$	H^i	$\sigma^i = \sigma^{i-1} - H^i(\delta^i - \delta^{i-1})$	H^i
(ii)	$\mathcal{G}_{Ic}$	-	σ^i	$H^i = \frac{2}{\sigma^i}[\mathcal{G}_{Ic} - \int_0^{\delta^{i-1}} \sigma d\delta]$	σ^i
(iii)	-	-	σ^i	σ^i	σ^i

be applied to the same specimen following one of the procedures defined in the ISO standards (ISO 15024 for mode I delamination tests or ISO 25217 for DCB test on bonded joints). The third approach was developed with the aim to obtain the CL without knowing either σ^0 or $\mathcal{G}_{Ic}$, however, this solution has been shown to be extremely dependent on the first selected point of the load-displacement curve.

Figures 3.3, 3.4 and 3.5 show a schema of the definition of the cohesive law in three steps for each alternative inverse method. At each selected point, the unknown branch of the CL is initialized assuming an initial slope H^i or an initial σ^i. Then, a load-displacement curve (labelled A) is predicted with the Direct Method described in the previous section. As the trial slope overestimates the load for a displacement, the iterative process is continued by changing the slope H^i or σ^i. This process is repeated until the predicted load matches the experimental one within a desired error (labelled C). To automate the process, a numerical Secant method algorithm was implemented. For a more detailed description of the algorithm the reader can refer to Ortega et al. [138].

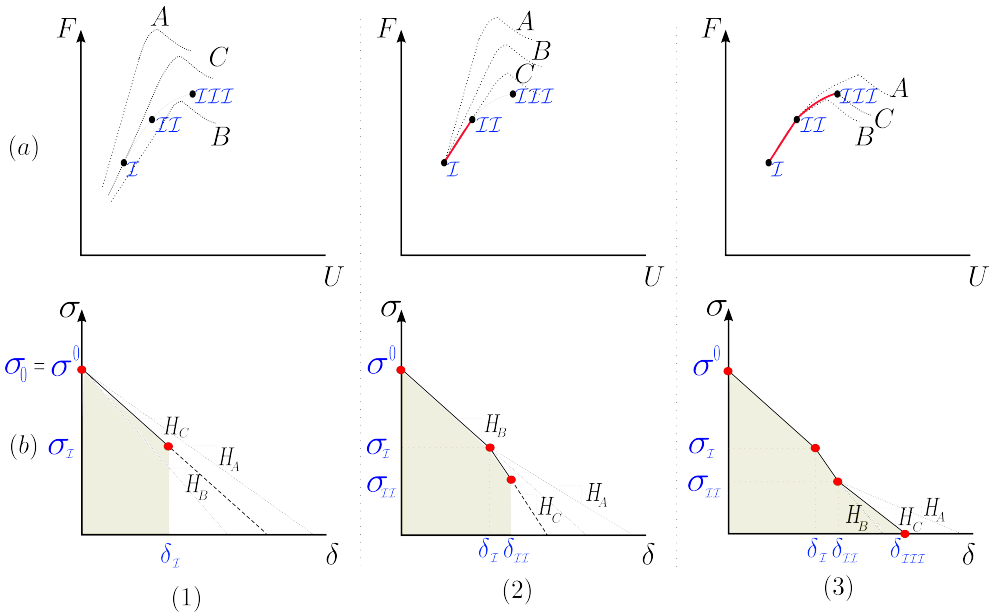

Fig. 3.3.: Inverse method to obtain the CL where σ^0 is known for 3 selected points: Alternative (i).

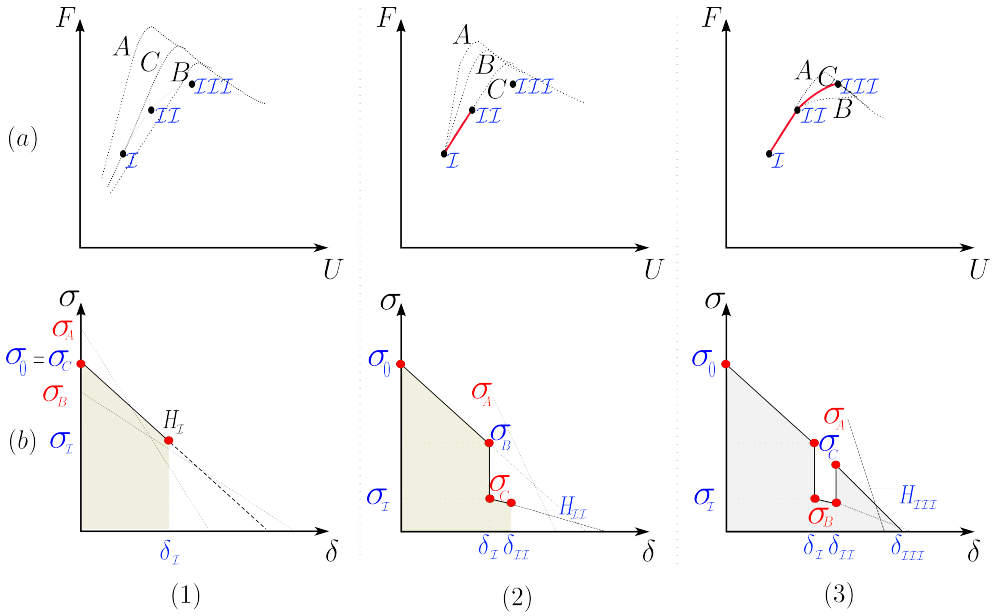

Fig. 3.4.: Inverse Method to obtain the CL where $\mathcal{G}_{Ic}$ is known for 3 selected points: Alternative (ii).

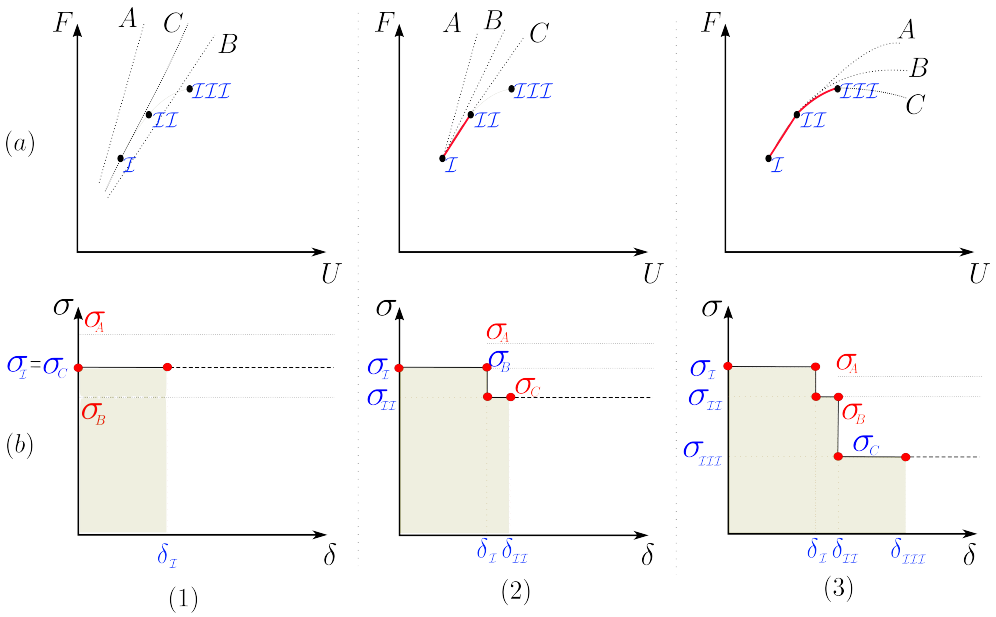

Fig. 3.5.: Inverse Method to obtain the CL where $\mathcal{G}_{Ic}$ and σ^0 are unknown for 3 selected points: Alternative (iii).

3.4 Validation of the Direct and the inverse methods

In this section, the performance of the analytical method is analysed by comparing it to finite element simulations using cohesive elements.

3.4.1 Validation of the Direct Method

To validate the response of the direct method, the commercial software ABAQUS [141] was used to define FE models of DCB specimens using 2D plane strain CPE4I elements for the adherends and 4-node cohesive elements for the interface. The elastic properties of the adherends considered in the simulation, as well as the fracture properties of the interface, are listed in Table 3.2. The cohesive zone model formulated by Turon et al. [52] was used for the cohesive elements. Ten elements were used to model the arm thickness with a maximum element size of 0.25 mm. A sketch of the simulation, the details of the mesh and the boundary conditions are shown in Fig. 3.6. Tie constraints have been used to place the zero thickness cohesive elements in the interface.

Tab. 3.2.: Elastic properties of the ply and interface properties.

E_{11}	$E_{22} = E_{33}$	$G_{12} = G_{13}$	G_{23}	$\nu_{12} = \nu_{13}$	ν_{23}
142.0 GPa	7.8 GPa	4.0 GPa	2.8 GPa	0.25	0.25
$\mathcal{G}_{Ic}$	K_n				σ^0
0.1:1 kJ/m^2	10^6 N/mm^3				1:80 MPa

The comparison of the load-displacement curves obtained from the analytical direct method and the FE simulations for a specimen with $\mathcal{G}_{Ic} = 0.969$kJ/m^2, $a_0 = 25$ mm and σ^0 (5, 10 and 40 MPa), are shown in Fig. 3.7. An excellent agreement between the analytical and FEM results was obtained throughout the entire test, demonstrating that the direct method is perfectly capable of reproducing the load-displacement curve from the elastic response until the end of the test. Moreover, the σ^0 value have a great effect on the initial part of the load displacement curve and has no effect once the crack propagation occurs, in agreement with Blackman et al. [106].

Three instant load levels: A, B and C, with σ^0=5 MPa to show the crack formation effect (see Fig. 3.7) are selected from the FEM. At load level A, the FPZ is still forming while at B it is completely formed and C represents a propagation instant. Fig. 3.8 shows the traction stresses and the opening displacements versus the distance to initial crack obtained using the direct method plotted together with the FE results

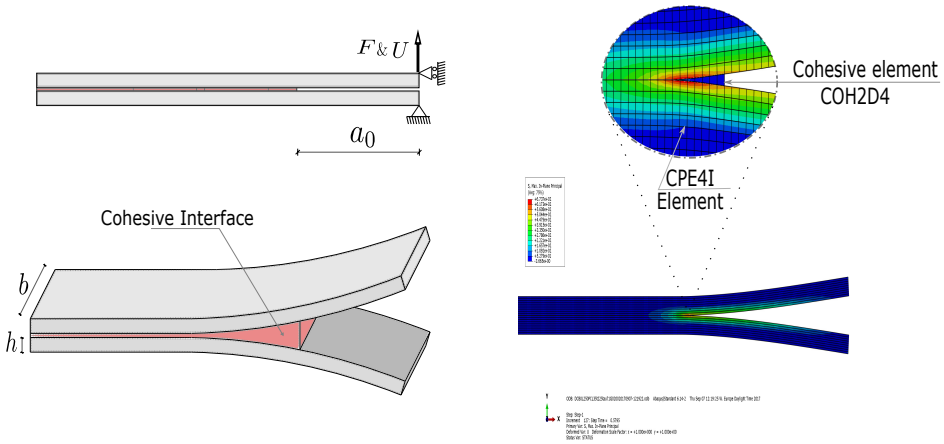

Fig. 3.6.: FEM using zero thickness cohesive elements.

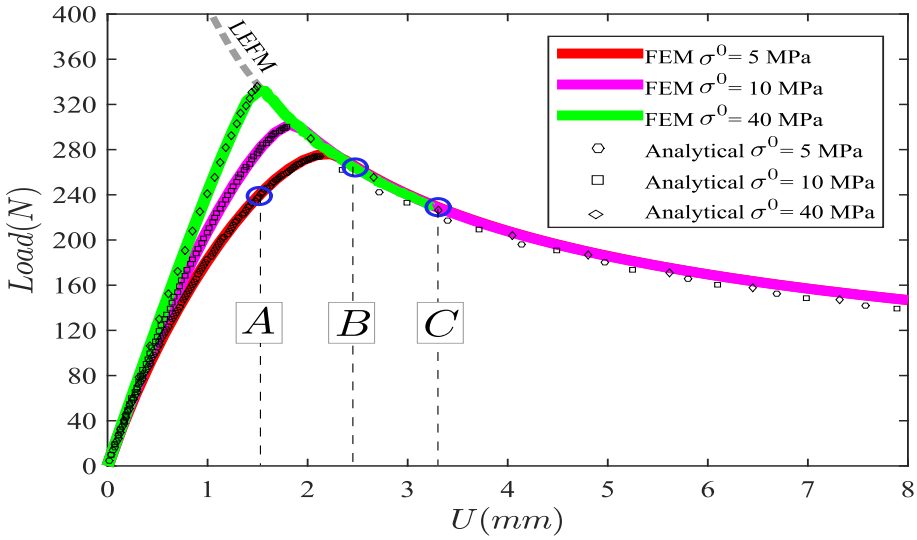

Fig. 3.7.: Analytical and FEM load-displacement curves for $a_0 = 25$ mm, $\mathcal{G}_{Ic} = 0.969\text{kJ/m}^2$ and $h = 2.5$ mm, and strong dependence of the load-displacement with σ^0 in agreement with Blackman et al. [106]. The LEFM curve is generated using the procedure found in [142].

for A, B and C. A good agreement between the analytical and FE results is obtained. Furthermore, the results obtained (Fig. 3.8) represent the behaviour of the FPZ obtained for A, B and C. At load level A, the FPZ is developing along with the stress profile, which goes from 3.25 MPa to σ^0. At B, the FPZ is completely formed, the stress profile goes from 0 to σ^0 and the opening displacement reaches the critical value. From this point onwards, crack propagation occurs where the stresses and the length of the FPZ remain constant. This is observed in Fig. 3.8-a where, once the FPZ is fully developed, the traction profile profile shifts (load level C) along the crack length, whereas the displacement increases monotonically.

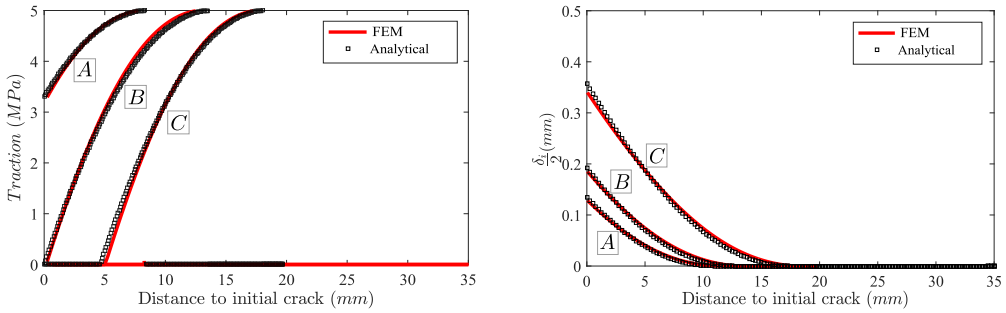

Fig. 3.8.: (a) cohesive stresses and (b) displacement jump profiles in the FPZ for the different load levels labeled A, B and C in Figure (3.7) for σ^0=5 MPa.

3.4.2 Validation of the Inverse Method

A validation of the inverse method is also carried out with FE numerical simulations. A load-displacement curve is created from a numerical simulation of the DCB test by imposing a linear cohesive law, CL ($G_{Ic} = 0.8$ kJ/m^2 and $\sigma^0 = 40$ MPa), an initial crack length $a_0 = 35$ mm, a thickness $t = 2.5$ mm, and the elastic properties listed in Table 3.2 for the adherends. From the load-displacement curve created, seven points were selected for the fit to obtain the CL using the different approaches explained in section 3.3 (Fig. 3.9). Alternatives (i) and (ii) provide accurate results for the CL compared to the one imposed. Alternative (iii) provides an escalated CL with the same $\mathcal{G}_{Ic} = 0.8$ kJ/m^2 and with a σ^0 slightly below that of the imposed one. The shape and the differences may be attributed to the number of selected points because as this number increases a more accurate CL is expected.

3.5 FPZ analysis for different material systems

The experimental data reported by Sarrado et al. [123] and Arrese et al. [129] is used in this section to demonstrate the capability of the model. In addition, in the work of Sarrado et al. [123] and Arrese et al. [129], two different methods to

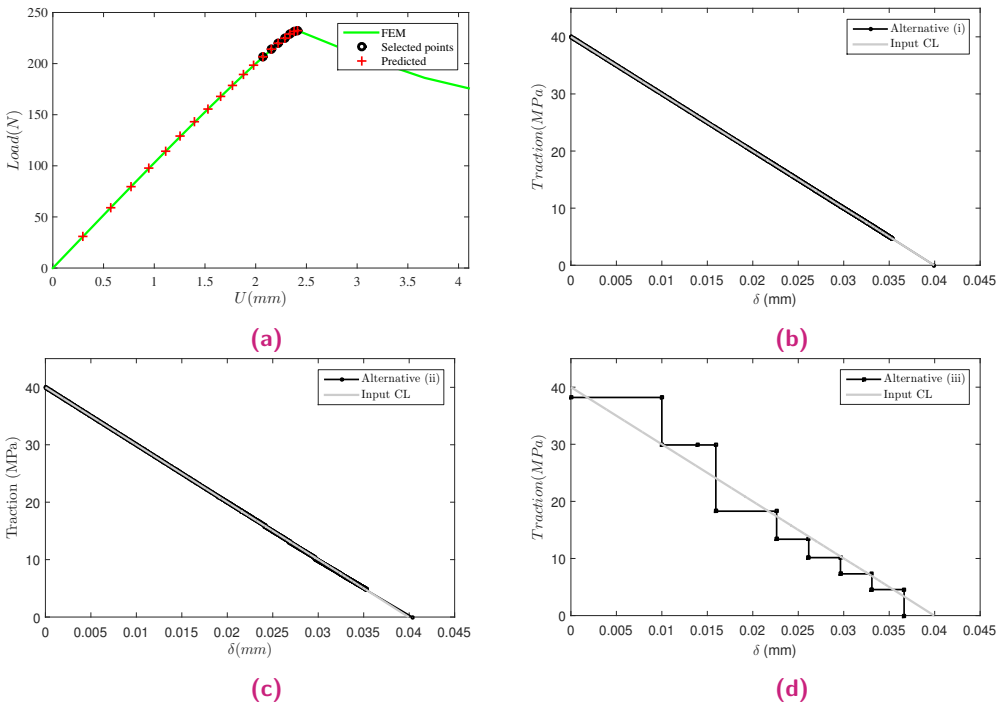

Fig. 3.9.: (a) Predicted load-displacement for FEM and obtained cohesive laws where (b) is Alternative (i), (c) is Alternative (ii) and (d) Alternative (iii), according to Table 3.1.

determine the cohesive law are proposed: a direct and an inverse one, respectively. Both methods are compared to the methodology developed in this chapter.

3.5.1 Cohesive law on delamination tests

The load-displacement curve of a DCB composite specimen (named S1) tested in [129] is plotted in Fig. 3.10-a. As stated by the authors, the fracture process presents bridging during the first 8.00 mm of propagation.

From this data, a CL has been extracted by following the inverse procedure described in section 3.3, with no inputs from the CL (Alternative (iii), see Fig. 3.10-b). For the sake of clarity, the Y-axis is plotted in log scale, so that the bridging contribution can be clearly represented ($\delta > 0.04$ mm). The area enclosed by the obtained CL is 0.451 kJ/m^2; close to the value obtained by Arrese et al. [129] (0.45 kJ/m^2). The predicted load-displacement curve from the direct method described in section 3.2 fits well with the experimental results, Fig. 3.10-a.

Fig. 3.10-c shows the CL obtained from the initial values of the crack tip opening displacement, where there is no bridging contribution ($\delta <= 0.04$ mm). Two obtained CL are compared to the results from Arrese et al. [129]: one obtained from the Alternative (iii) procedure, and, as the energy release rate is known at $\delta = 0.04$

mm, a second one from Alternative (ii). For this latter case, the CL is drawn from six and ten points of the load displacement curve. In all the cases, a good agreement between the CL is obtained, with the same σ^0 and $\mathcal{G}_{Ic}$. Furthermore, the shape of the cohesive law is not substantially affected by the number of selected points.

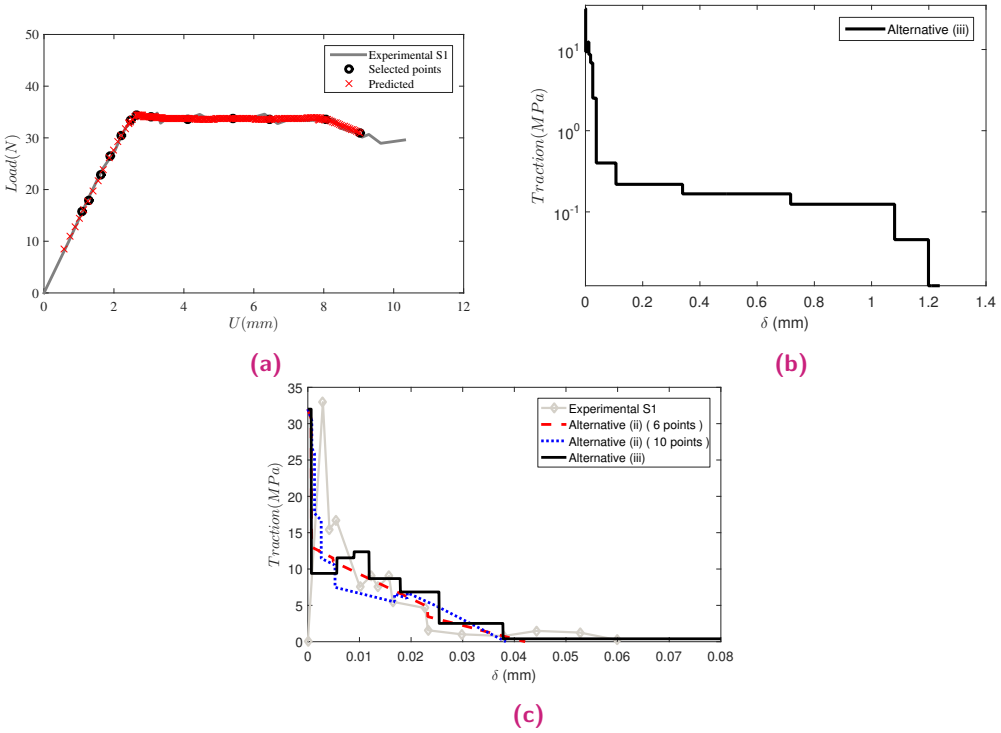

Fig. 3.10.: (a) Load-displacement; (b) CL results from Alternative (iii) with no input parameters in the CL, and; (c) CL obtained from Arrese et al. [129] and the inverse methods developed in section 3.3.

3.5.2 J-δ curves for bonded joints

The inverse method has been used to extract the CL in bonded joints tested by Sarrado et al. [123]. Three types of specimens, termed A2T1, A2T2 and A3T1, were used to study the effect adhesive thickness has on the J-δ curves. A2 and A3 refer to the thickness of each adherend (2.20 and 2.92 mm, respectively), and T1 and T2 to the adhesive layer thickness (0.21 and 0.37 mm, respectively). For a more detailed explanation of the specimen configurations, the reader should refer to Sarrado et al. [123].

The load-displacement curves of the specimens are shown in Fig. 3.11. A set of points was selected from each experimental curve to obtain the J-δ curves. Alternative (iii) was used to obtain the cohesive law as no values of σ^0 or $\mathcal{G}_{Ic}$ were provided by the

authors. Once the cohesive law was obtained, the J value was calculated according to [98] as the following:

$$J = \int \sigma d\delta \tag{3.22}$$

The J-δ curves are plotted in Fig. 3.12, together with the results obtained from the methodology proposed in [123]. A close agreement is observed between them, and the J-δ curves were also extended from what Sarrado et al. [123] proposed. Besides this, good predictions of the load-displacement curves were obtained with the direct method as shown in Fig. 3.11.

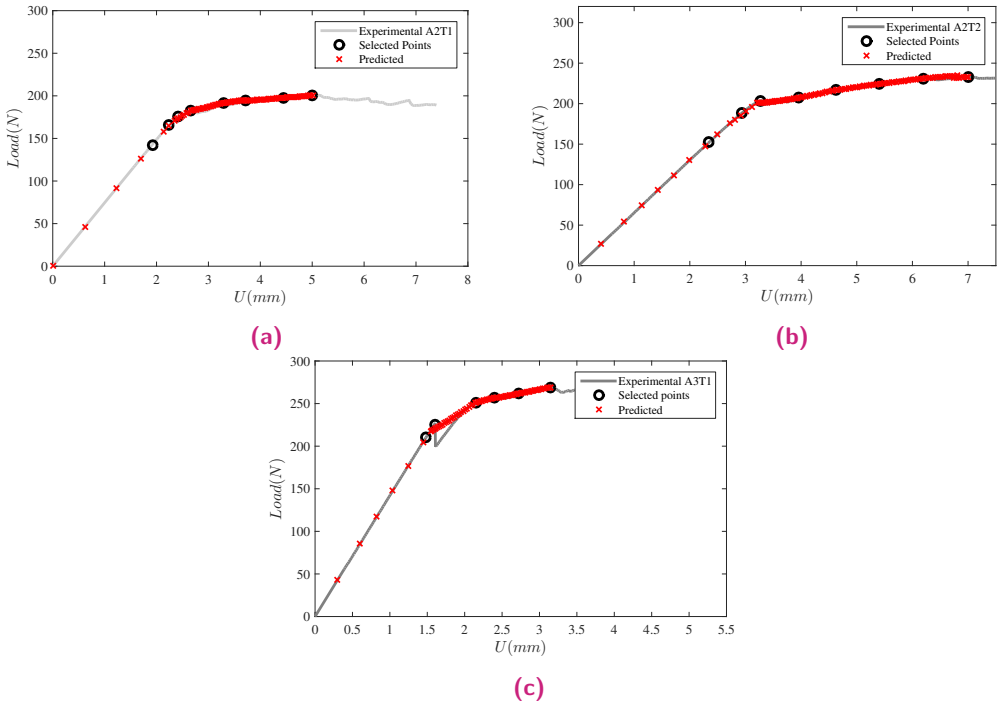

Fig. 3.11.: Experimental load-displacement results from [123] with the selected points used in the CL fitting.

The method proposed by Sarrado et al. [123] was not capable of measuring the complete J-δ curve in specimen A3T1 as there was unstable crack growth during the FPZ formation. Conversely, the inverse method was able to fully represent the J-δ curve by simply omitting the unstable jump, Fig. 3.12-c.

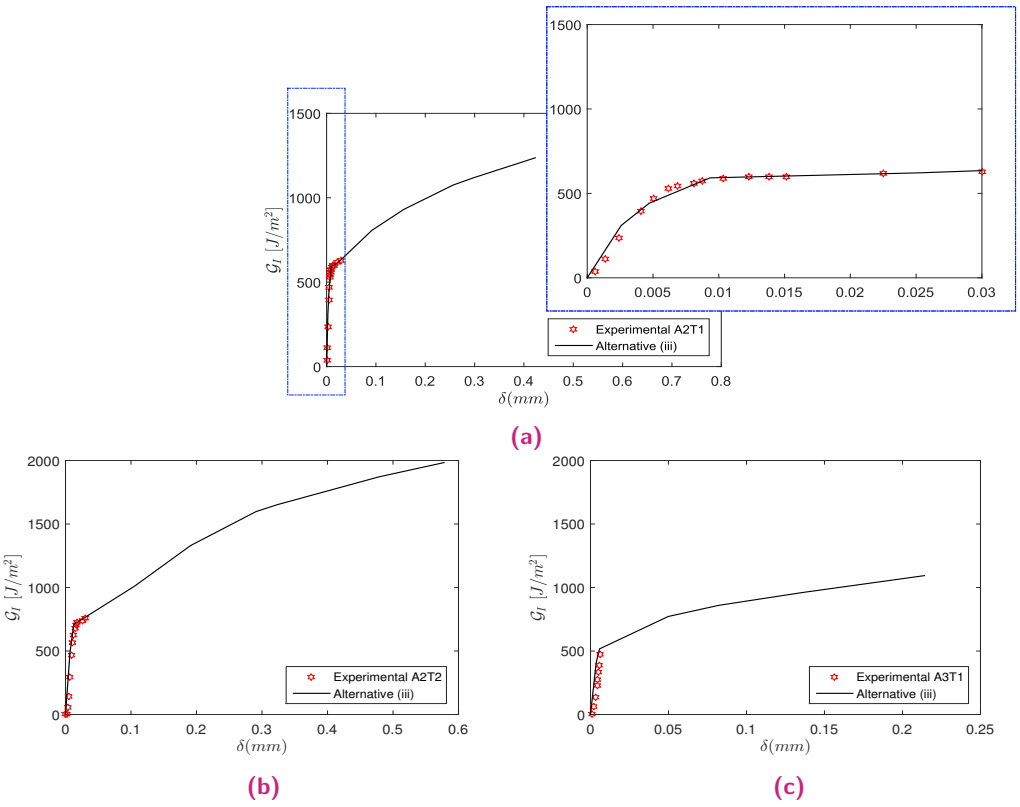

Fig. 3.12.: Comparison between the experimental J-δ curve [123] and the J-δ curve obtained using the inverse method described in section 3.3.

4 The influence of mode II test configuration on the cohesive law

4.1 Introduction

As an extension to the method presented in Chapter 3, a method based on Dugdale's condition [49] has been developed to extract the cohesive law from only the load and displacement data, obtained from the tests for mode II fracture toughness (ENF and ELS). The method combines a direct model to obtain the load-displacement curve from a cohesive law with an inverse method to obtain the cohesive law from the load-displacement curve. The developed method has been used to analyse the experimental data obtained from two test configurations (ENF and ELS) in order to study the influence test configuration cohesive laws have under pure mode II. Finally, the fracture toughness results obtained from the area under the cohesive law are compared to those obtained by a data reduction method based on the J-integral.

4.2 Analytical method to obtain the cohesive law from a mode II fracture test

The analytical method is an extension of the work presented in Chapter 3 for mode I fracture tests. The method is an algorithm that combines a direct model with an iterative procedure to extract the cohesive law for an experimental load-displacement curve. The direct model is an analytical approach to plotting the load-displacement for a given cohesive law. The model is valid under the following hypothesis: it is a 2D plane strain problem where the material response lies on the bondline and the only source of nonlinearity in load-displacement is the interface response.

The method has been applied to the two most popular and standardized mode II tests: the ENF and the ELS. These two mode II test configurations (ENF and ELS) are subjected to controlled displacement (U), and the corresponding load (F) applied as shown in Fig. 4.1. The length L_{dam} is the damaged length of the interface material, measured from a_0, and includes an FPZ and a traction-free crack surface (see Fig. 4.1). The solution of the mode II non-linear problem can be simplified using the principle of superposition [132, 133] and Dugdale's model concept [49]: the overall

stress intensity factor SIF vanishes in the presence of a cohesive zone ahead of a crack tip. In the case of an ENF or ELS specimen, this condition reads:

$$K^F + K^{\tau_c} = 0 \tag{4.1}$$

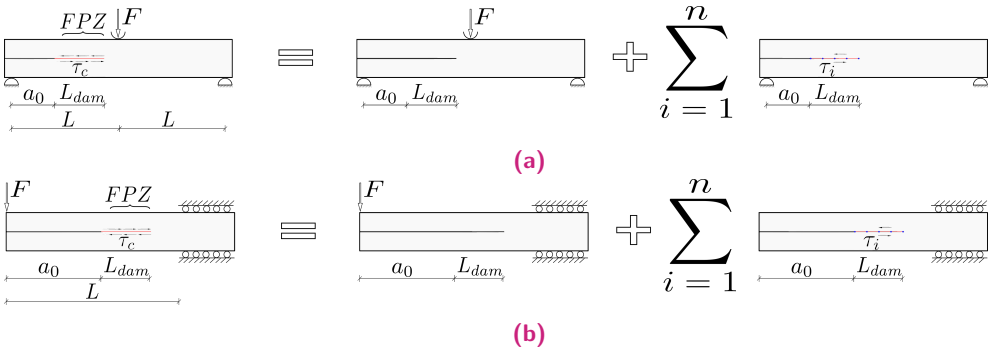

Fig. 4.1.: (a) ENF and (b) ELS specimens expressed as a superposition of acting loads.

where K^{τ_c} is the stress intensity factor caused by the cohesive shear stress profile (τ_c) at L_{dam} and K^F is the SIF due to the external load F, see Fig. 4.1, which can be expressed as:

$$K^F = \frac{F}{b\sqrt{h}}\hat{K^F} \tag{4.2}$$

where b and h are the specimen width and adherend thickness, respectively, $\hat{K^F}$ is the nondimensional form of the SIF caused by a unitary load F, which depends on the geometry. The profile of the shear stresses τ_c at cohesive zone can be discretized by vector τ_i, where each component of this vector produce a nondimensional SIF that depend on the geometry. The total SIF caused by the cohesive shear stress profile is:

$$K^{\tau_c} = \tau_i\sqrt{h}\hat{K_i^\tau} \tag{4.3}$$

where $\hat{K_i^\tau}$ is the nondimensional form of the SIF due to a constant unit cohesive shear stress τ_i applied over a small length at a distance a_i from the loading point F. This SIF depends on the geometry and the location of the cohesive shear stress τ_i. These stress intensity factors can be obtained by numerical methods and, in some

cases, are tabulated in handbooks [143]. The applied load F can be related to the cohesive shear stress by substituting equations (4.2) and (4.3) into equation (4.1):

$$F = \frac{b\,h}{\hat{K}^F}\tau_i \hat{K}_i^{\tau} \tag{4.4}$$

On the aim of defining the cohesive shear stress profile along the FPZ, the shear displacement field must be obtained. The shear displacement field at L_{dam} can be defined as the superposition of the shear displacement caused by the loads as:

$$\delta_i = \delta_i^F + \delta_i^{\tau_c} \tag{4.5}$$

where δ_i is the total shear displacement at position i, δ_i^F is a vector that describes the shear displacements at the cohesive zone caused by the applied load F, and $\delta_i^{\tau_c}$ is the shear displacement caused by the whole shear stress profile τ_c. Furthermore, $\delta_i^{\tau_c}$ and δ_i^F can be defined as:

$$\delta_i^F = \frac{F\hat{a}^2}{Eb}\hat{\delta}_i^F \quad , \quad \delta_i^{\tau_c} = \frac{\tau_j h \hat{a}^2}{E}\hat{\delta}_{ij}^{\tau_c} \tag{4.6}$$

where E is the adherends Young's modulus in the longitudinal direction and $\hat{a} = \frac{a}{h}$ is the non-dimensional form of the crack length. $\hat{\delta}_{ij}^{\tau_c}$ is the non-dimensional form of the shear displacement at position i caused by a unit shear stress at position j inside the cohesive zone and $\hat{\delta}_i^F$ is the non-dimensional form of the shear displacement at position i due to unitary external load F. Again, $\hat{\delta}_{ij}^{\tau_c}$ and $\hat{\delta}_i^F$ are non-dimensional forms that depend on the geometry and can be obtained by numerical methods. At this point, the total shear displacement at position i can be obtained by substituting equations (4.4) and (4.6) into equation (4.5):

$$\delta_i = f_{ij}\tau_j \frac{h\hat{a_i}^2}{E} \tag{4.7}$$

where f_{ij} is expressed as:

$$f_{ij} = \frac{\hat{\delta}_i^F\,\hat{K}_i^{\tau}}{\hat{K}^F} + \hat{\delta}_{ij}^{\tau_c} \tag{4.8}$$

Equation 4.7 relates the shear displacement to the cohesive shear stress. Consequently, it is possible to obtain the cohesive shear stress profile by an iterative process to solve Equation 4.7 for a given cohesive law ($\tau_j(\delta_j)$). The solution algorithm can be found in [138, 144]. Once τ_i is known, the load F and shear displacement profile

for a given CL are obtained using Equations (4.4) and (4.7). Likewise, the total displacement U at the loading point can be defined by the superposition:

$$U = U^F + U^{\tau_c} \tag{4.9}$$

$$U^F = \frac{F\hat{a}^3}{Eb}\hat{U^F} \quad and \quad U^{\tau_c} = \frac{\tau_j h\hat{a}^3}{E}\hat{U^{\tau_c}} \tag{4.10}$$

where U^F and U^{τ_c} are the displacements at the loading application point caused by load F and the cohesive shear stress profile τ_c, respectively, and $\hat{U^{\tau_c}}$ and $\hat{U^F}$ are the normalized forms of vertical displacements U^{τ_c} and U^F, respectively, that also depend on the geometry.

To this end, by knowing the cohesive law of the interface material it is possible to define load F and the total displacement at the loading application point using the following procedure: first, a damage length is selected ($\frac{h}{10^8}, \frac{h}{10^7}, ..., \frac{h}{10}, \frac{h}{5}, ..., 10h$), then Equation (4.7) is solved using an iterative approach for a given CL and, as a result, the shear stress profile τ_j and the shear displacement δ_j at the FPZ are determined. Lastly, load F is obtained through Equation (4.4) and the displacement U is obtained using Equation (4.9). A more detailed description of the procedure can be found in [138, 144].

This procedure can be rewritten as a standard code, provided with the non-dimensional parameters found in Equations (4.4), (4.8) and (4.10), to obtain a load-displacement curve for any CL. To obtain the non-dimensional parameters $\hat{K}^F$, $\hat{K}_i^\tau$, $\hat{\delta}_i^F$, $\hat{\delta}_{ij}^\tau$, $\hat{U}_i^F$ and $\hat{U}_c^\tau$ for each test in Fig. 4.1 (ENF and ELS), a parametric FE model is constructed. In this current chapter, the problems shown in Fig. 4.1 were modelled using ABAQUS [141] with 2D plane strain CPE4I elements with squared element sizes of 0.1 mm, where $F = 1$ N and $\tau_i = 1$ N/mm^2. The values of δ_i^F, δ_i^τ, U_i^F and U_i^τ are extracted directly from the FE results, where $i = 1$: n and n is the number of points located along the interface length. The non-dimensional forms ($\hat{\delta}_i^F$ and $\hat{\delta}_{ij}^\tau$) are calculated using Equation (4.6), likewise, the values of $\hat{U}_i^F$ and $\hat{U}_c^\tau$ are obtained using Equation (4.10). Finally, the values of K^F and K_i^τ were computed using the VCCT method [48, 145, 146] then used to determine the non-dimensional ones using equations (4.2) and (4.3).

Beyond this point, an analytical algorithm is formulated (an iterative process combines the aforementioned direct model) to extract the cohesive law from an experimental load-displacement curve. Ortega et al. [138] proposed that the behaviour of the fracture process zone during the loading process allows the CL to be guessed

through the best fitting of the load-displacement curve where each increase in the fracture process zone length corresponds to a segment of the CL.

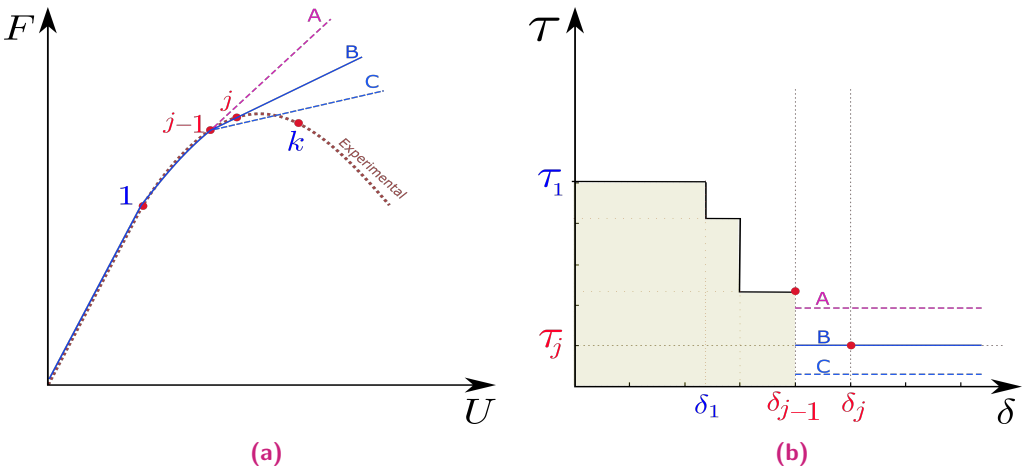

Fig. 4.2.: (a) Example of an F-U curve with the selected points, 1:k, and (b) the corresponding CL.

The algorithm follows the subsequent procedure: first, k points from the load-displacement curve are selected. The first point is selected where the load-displacement curve loses its linearity (point 1 in Fig. 4.2) and the last point is selected when the FPZ is fully developed (point k in Fig. 4.2). It must be mentioned that the selection of point k is somewhat arbitrary, because it is difficult to know in advance the point at which the FPZ is fully developed. However, if this does not occur we can modify the selection of point k, or we can add another point until we see the FPZ totally developed (i.e. an entire CL).

For each load-displacement point (j), a small part of the CL that is located between points $j-1$ and j is defined by assuming an initial τ^j. Then, a load-displacement curve is predicted with the direct model described above. Then, the error between the experimental load at point j and the numerical load at $U(j)$ is computed and the secant-method to minimize this error is used to find the final value of each τ^j. At this point, the corresponding displacement jumps δ_j are also determined by the cohesive shear displacement ahead the crack tip. Furthermore, the fracture toughness can be calculated by the numerical integration of the cohesive law:

$$\mathcal{G}_{II} = \int \tau(\delta) d\delta \tag{4.11}$$

where τ and δ are the stress and displacement jumps at the crack tip, respectively.

4.3 Experimental set-up and test specimens

To prove the usefulness of the method, an experimental testing campaign was carried out where the cohesive law of bonded joints with carbon fiber reinforced polymer adherends was obtained from ENF and ELS tests. The specimens tested were made of two adherends of the same material bonded by an epoxy adhesive. The adherends are CFRP with multidirectional balanced lay-ups ($[0°/0°/+45°/\text{-}45°/+45°/\text{-}45°]_s$). Both the adherends and adhesive are common materials in the aeronautical industry. However, the commercial names of the adherends and adhesive are not listed for reasons of confidentiality. The specimens were cured in an autoclave and secondary bonded. The same adhesive was used in M1 and M2 configurations. The dimensions of the specimens were 210 mm long, 25 mm wide and a total thickness of 4.8 mm. One double layer of polytetrafluoroethylene (PTFE) film was used to form a 60 mm insert. In order to obtain stable crack initiation, a mode I pre-crack was carried out in a test rig designed according to the ISO25217 [147] test standard. The pre-crack propagation was set to have a minimum length of 5 mm. The crack length was measured after the pre-crack test using an optical microscope at both sides. Following the pre-crack, ENF and ELS tests were carried out in accordance with the ISO15114 [148] and ASTM D7905 [149] standards, respectively, to characterize the adhesive joints under pure mode II. Five specimens were tested (ENF and ELS) for each material configuration listed in Table 4.1.

Tab. 4.1.: Specimen configurations.

ID	Test	Adherend Material
M1ENF	ENF	M1
M2ENF		M2
M1ELS	ELS	M1
M2ELS		M2

Fig. 4.3 shows the test setup and the geometry of the specimens for both the ENF and ELS tests. Further details concerning the tests may be found in [70]. The dimensions of the ENF specimens were L = 60 mm and a_0 = 35 mm while the geometry of ELS specimens was L = 100 mm and a_0 = 55 mm. The adhesives used allowed larger a_0/L ratios, specially in ENF tests, having more stable tests as shown in [70].

Both mode I pre-crack and mode II tests were run under displacement control in an electromechanical MTS testing machine equipped with a 10 kN load cell. During the test, the displacement rate was 1 and 2 mm/min for ENF and ELS tests respectively, in order to ensure a quasi-static crack growth [148, 149]. The crack length was visually tracked using a Canon 550D camera with a macro length lens affixed on a travelling fixture following the vertical marks, each at 1 mm, on the edge of the

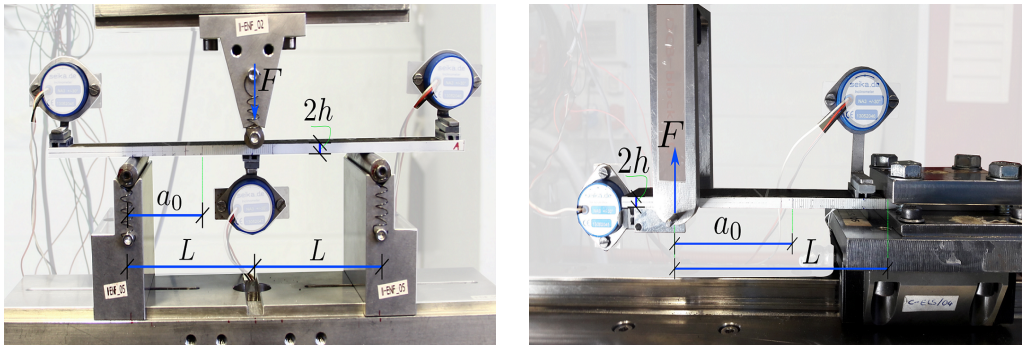

(a) (b)

Fig. 4.3.: (a) ENF and (b) ELS geometry and test fixtures.

specimen. The displacement and the force recorded from the test machine, the crack length and the rotational angle measured with capacitive inclinometers were synchronized and acquired in real-time using a data acquisition system. Neither the crack length nor the rotational angle were used in obtaining the cohesive law, but to obtain the fracture toughness according to [70] for comparison purposes.

4.4 Results and discussion

To investigate the influence of the mode II test configuration on the shape of CL, the results from the ENF and ELS configurations tested in [70] are presented and a comparison is made between the extracted CL and the J-integral measurements obtained by Pérez-Galmés et al. [70].

Fig. 4.4 shows the load-displacement curves of the four specimen configurations tested: two tests (ENF and ELS) and two adherends (M1 and M2). Five specimens for each configuration were tested. The load-displacement data were used to extract the cohesive laws for all the specimens using the analytical method.

Figures 4.5 and 4.6 show the average cohesive laws, extracted from ELS and ENF load-displacement curves, respectively, plotted together with the Standard Deviation (SD) for each crack opening displacement. In spite of having high values of standard deviation in the load-displacement curves, the cohesive law shape is the same for the specimens from the same batch. A full CL is not obtained from the ENF tests because in the last points of the CL the crack tip is close to the loading point which comes to zero stress ($\delta > 0.2$ mm). On the contrary, a complete cohesive law is obtained from the ELS tests as shown in Fig. 4.5 because in this latter case the specimens exhibit a larger propagation region as stated in [70].

The fracture toughness ($\mathcal{G}_{IIc}$) is computed by the numerical integration of the obtained cohesive law. The values of $\mathcal{G}_{IIc}$ are summarized in Table 4.2 for the ENF

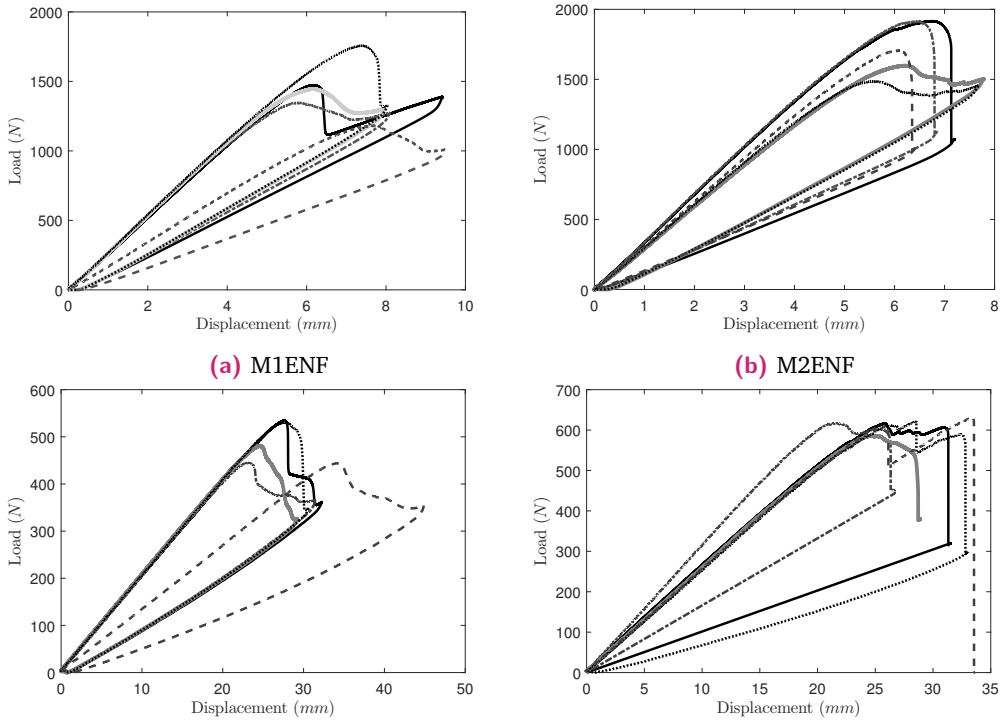

(a) M1ENF (b) M2ENF

(c) M1ELS (d) M2ELS

Fig. 4.4.: Experimental load-displacement curves, tested in [70], that were used to extract the cohesive laws.

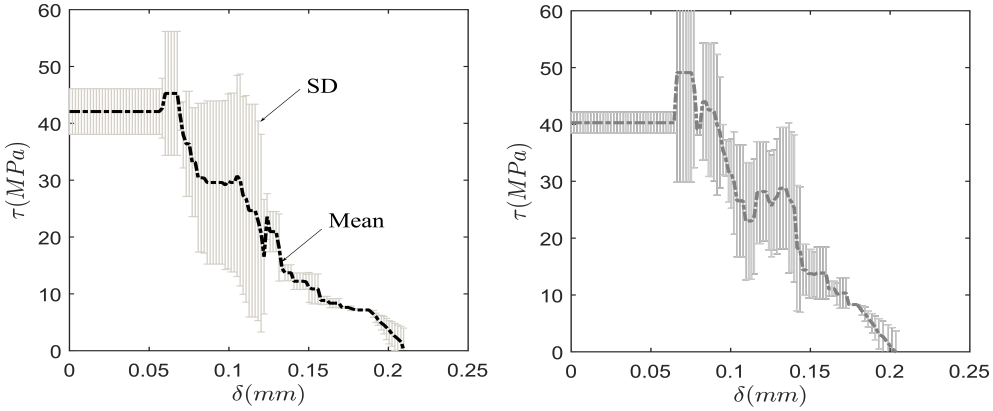

(a) M1ELS (b) M2ELS

Fig. 4.5.: Cohesive laws extracted from ELS test results for the material M1 and M2. The line indicates the mean value of the batch and the dots the standard deviation.

tests and Table 4.3 for the ELS tests. Each table shows the results of M1 and M2 materials, all related to a reference value ($\mathcal{G}_{IIc}$ of M1ENF). The tables also include the fracture toughness values obtained in [70] with the J-integral data reduction method.

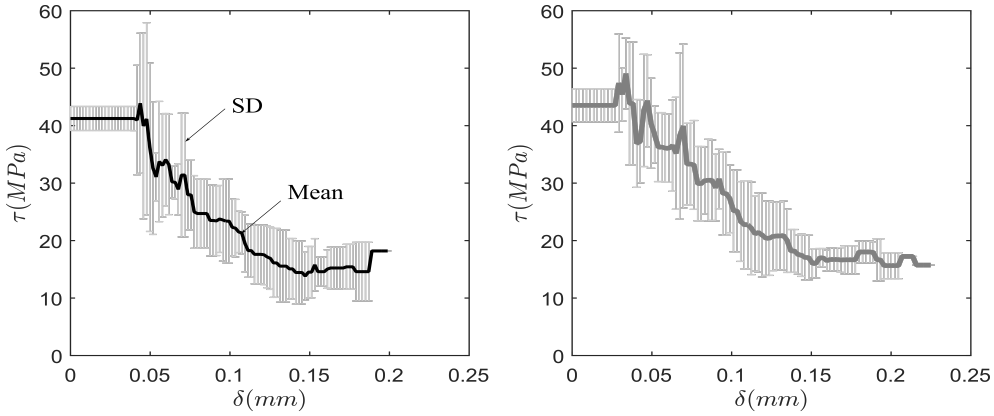

Fig. 4.6.: Cohesive laws extracted from ENF test results for the material M1 and M2. The line indicates the mean value of the batch and the dots the standard deviation.

Tab. 4.2.: Summary of the average fracture toughness of the ENF tests related to the M1ENF value.

ID		$\mathcal{G}_{IIc}{}^{b}$	$J_{ENF}{}^{a}$
M1ENF	Average	1.00	0.99
	SD	0.21	0.17
M2ENF	Average	1.10	0.98
	SD	0.21	0.22

[a] The J-integral value computed in [70].
[b] The area below the CL, Equation (4.11).

Tab. 4.3.: Summary of the average fracture toughness of the ELS tests related to the M1ENF value (Table 4.2).

ID		$\mathcal{G}_{IIc}{}^{b}$	$J_{ELS}{}^{a}$
M1ELS	Average	1.06	1.00
	SD	0.04	0.17
M2ELS	Average	1.16	1.06
	SD	0.16	0.07

[a] The J-integral value computed in [70].
[b] The area below the CL, Equation (4.11).

The calculated fracture toughness values have differences of less than 20 % with respect to the reference value. Fig. 4.7 shows the related values of fracture toughness with respect to the reference value, where $\mathcal{G}_{IIc}$ is the area below the CL calculated by

Equation (4.11) and the J-integral values (J_{ENF} and J_{ELS}) are found in [70]. The large SD obtained is partially explained because each batch tested has specimens from different panels [70]. Overall, a good agreement between the analytical method and the J-integral [70] results for both campaign materials is obtained with a 10% maximum difference between the results of the CL and the J-integral.

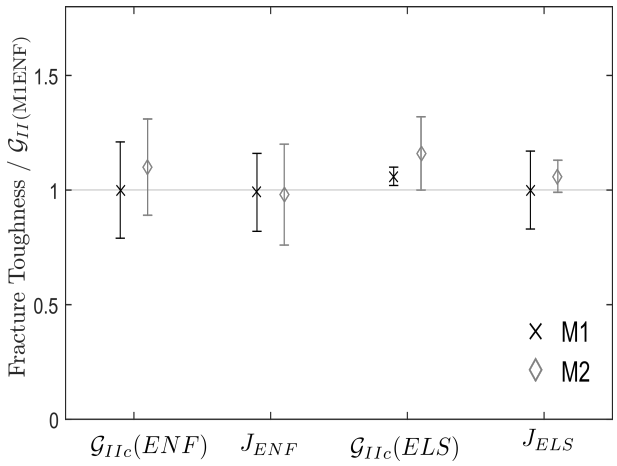

Fig. 4.7.: Summary of test results related to the value of $\mathcal{G}_{IIc}$(M1ENF), where $\mathcal{G}_{IIc}$ is the area below the CL. J_{ENF} and J_{ELS} are the J-integral values found in [70].

The average cohesive laws of the different test configurations and materials are plotted together in Fig. 4.8. For each test configuration, a good agreement between the average cohesive laws is obtained, acquiring close cohesive law shapes until a δ around 0.15 mm.

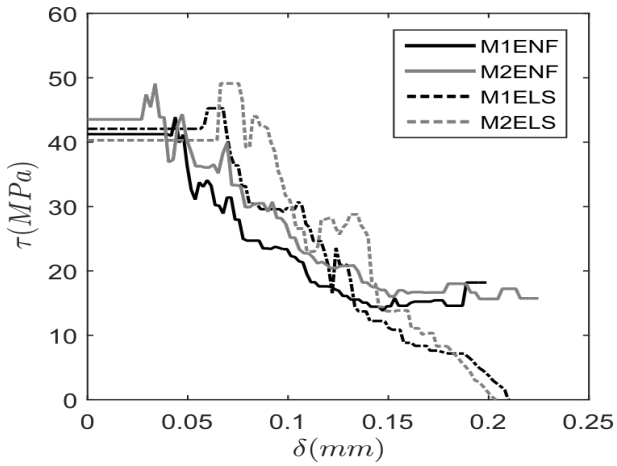

Fig. 4.8.: Average cohesive laws of the different test configurations.

In order to explain this difference, two representative R-curves of the M1 adherend for each ENF and ELS test, obtained from [70], are plotted together in Fig. 4.9. The values of the J-integral calculated by Pérez-Galmés et al. [70] are related to the results of the M1ENF configuration. The difference between the R-curves starts to

appear after a certain value of equivalent crack length (about 50 mm). At this point, the ENF specimen starts to gain more energy after a short plateau. This behaviour is also noticed in the load-displacement curves where the same occurs for the ENF tests, i.e., after a short propagation the load increases. This behaviour clarifies the differences between the cohesive law shapes of the ENF and ELS configurations, seen in Fig. 4.8 after a 0.15 mm opening displacement. The authors suggest that the reason for this behaviour is the proximity of the crack tip to the loading point, which affects the ENF results.

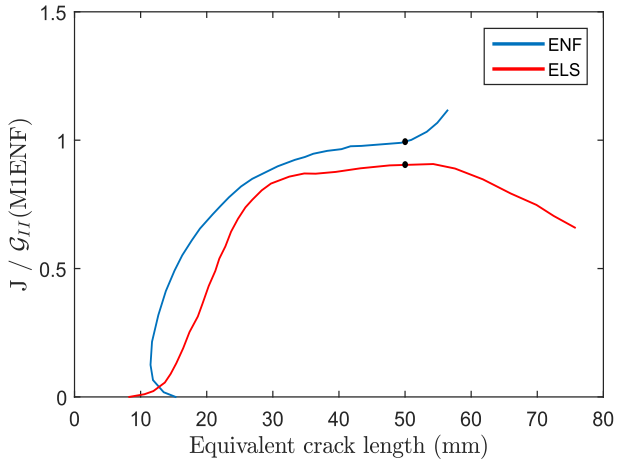

Fig. 4.9.: Representative R-curves of M1 specimens for ENF and ELS test results, found in [70]. The J values are related to the $\mathcal{G}_{IIc}$ (M1ENF).

Part II

Experimental work

5 Effect of environmental conditioning on pure mode I fracture behaviour

5.1 Introduction

In the current chapter, the effect of both temperature and accelerated ageing on the mode I fracture behaviour of two bonded joints configurations is investigated with the DCB test. Three groups of specimens were tested: as received, non-aged and wet-aged. The first group (as received) was tested at room temperature just after the manufacturing process while the second and the third groups (non-aged and wet-aged) were tested after four years at three different temperatures (-55°C, Room Temperature (RT) and 80°C). The wet-aged specimens were stored in an environmental chamber during four years to simulate a long exposure to harsh climatic changes while the non-aged specimens were kept under a controlled laboratory condition at room temperature. The degradation of the bonded joints is quantified with the fracture toughness and qualitative analyses from the images of the fractured surfaces. Two different methodologies were used to measure the fracture toughness: classical data reduction methods and an inverse approach.

The pages that may be part of an article are extracted.

6 Effect of environmental conditioning on mode II fracture behaviour

6.1 Introduction

This chapter introduces an experimental study on the effect of the exposure to accelerated ageing and temperature changes on the mode II fracture behaviour of adhesively bonded joints made with two different configurations of adhesively bonded joints (non-aged and wet-aged). ELS tests were performed at three different temperatures (-55°C, Room Temperature (RT) and 80°C). After testing, the obtained results were analysed, and the fracture toughness obtained using classical methodologies were compared to the results obtained using the methodology found in chapters 3 and 4.

The pages that may be part of an article are extracted.

7 Effect of environment conditioning on the cohesive laws

7.1 Introduction

Based on the results presented in Chapters 5 and 6, the effect of both temperature and ageing is investigated on the cohesive laws of bonded joints under mode I and mode II of loading using specimens made with two different types of adhesives. Double Cantilever Beam (DCB) and End Load Split (ELS) specimens (non-aged and wet-aged) were performed at different temperatures (-55°C, RT and 80°C). An efficient method has been used to extract the full shape of the cohesive law from the experimental load-displacement curves and afterwards we adjust it to a geometrical function.

The pages that may be part of an article are extracted.

Part III

Cohesive zone model

8 Simulation of bonded joints under different temperature and ageing conditions

8.1 Introduction

Existing cohesive zone formulations do not account for environmental effects. In this chapter, a new formulation of a cohesive zone model that includes the effects of temperature and ageing on the cohesive law shape is presented. The current approach is an extension of the formulation proposed by Turon et al. [155] using a multilinear cohesive law with an arbitrary number of line segments [55]. The dependence of the cohesive law with temperature and ageing is included in the formulation. The numerical model is validated by comparing the results of simulations of pure-mode fracture toughness tests and the available experimental work in Part II. Finally, the efficiency of the model was tested under different loading using two types of adhesively bonded joints (wet-aged and non-aged) tested under three temperatures (-55°C, RT and 80°C).

The pages that may be part of an article are extracted.

Part IV

Conclusions and future work

9 Conclusions and future work

9.1 Main Conclusions

The main objective of the present thesis is to provide a methodology to study bonded joints exposed to different environmental conditions. The current work focuses on the fracture behaviour of bonded joints subjected to different temperature and ageing conditions. The completion of this main objective has been pursued by the development of three main contributions. The first contribution of the work is to develop an efficient method to obtain the cohesive laws of bonded joints subjected to mode I and mode II loading cases. The second contribution is the experimental investigation of bonded joints, for better understanding the influence of different environmental conditions on the cohesive laws. Finally, the cohesive laws as a function of temperature and ageing have been combined into a cohesive zone model to simulate the effect of environmental changes in the mechanical behaviour.

In light of the results and the discussions introduced in the previous chapters, the following conclusions can be drawn.

9.1.1 Methodology to obtain cohesive laws

A novel inverse methodology to extract the cohesive law for DCB specimens has been proposed. It allows the CL to be estimated from a single load-displacement curve without using any additional measurement, thus drastically reducing the cost and complexity of the test. The formulation of the method is implemented in two steps: a direct method to represent the load-displacement curve for a given cohesive law, and an inverse method to extract the cohesive law from experimental load-displacement data. The methodology implemented has been compared to LEFM analytical results, finite element numerical results, and two sets of experimental data. The method has shown a good agreement with the analytical, numerical and experimental results.

Similarly, an inverse methodology to obtain the cohesive law of the mode II tests was developed from an experimental load-displacement curve without any optical measurements. This method is based on the inverse method developed for mode I.

With the aim of proving the objectiveness of the method, bonded joints with adherends made with two materials were tested using ENF and ELS tests. The ana-

lytical method was used to extract the cohesive laws from the experimental load-displacement curves of the ENF and ELS configurations. The obtained cohesive laws show a good agreement not only with regards to the area enclosed by the CL, but also the shape of the cohesive law. This behaviour leads to the conclusion that, for the bonded joint configurations tested, the cohesive law is a material property and is independent of the test configuration. The fracture toughness obtained based on the J-integral closed form are in agreement with the fracture toughness provided by the CL. The developed method has the advantage of representing the behaviour of the fracture process zone for both ENF and ELS tests.

9.1.2 Effect of temperature and ageing

The effect of temperature and accelerated ageing on the fracture toughness of two types of secondary bonded joints was studied in this work. Two types of adhesively bonded joints (wet-aged and non-aged) were tested using the DCB and ELS test configurations at various temperatures (-55°C, RT and 80°C). From the analysis of the results, temperature plays a vital role in the definition of the fracture mode and propagation response of the bonded interface. The predominant fracture mode of all the tested specimens is cohesive failure while adhesive failure was observed in -55°C tests and delamination failure was noticed in the DCB wet-aged specimens. Moreover, when testing at high-temperature the fracture process zone length increases. The ageing process has a significant influence on the adhesive joint fracture response. The fracture toughness of the wet-aged specimens was significantly degraded, especially in the case of material system A2.

Finally, an inverse method was used to extract the cohesive laws and the J-integral using the experimental load-displacement curves. Then, the results obtained were compared with other data reduction methods, and a good agreement was obtained. For the DCB tests, some differences were obtained at -55°C. A stick-slip behaviour was observed and the cohesive law was not fully obtained. The analysis of the obtained cohesive laws shows that exposure to the different environmental conditions affect the cohesive laws of the studied bonded joints differently. As a conclusion, Fig. 9.1 shows a schematic sketch of these effects for Mode I and Mode II, respectively. It can be observed that ageing mainly affected the cohesive law by reducing the fracture energy while the exposure to high temperature or freezing temperature also influences the shape of the cohesive law.

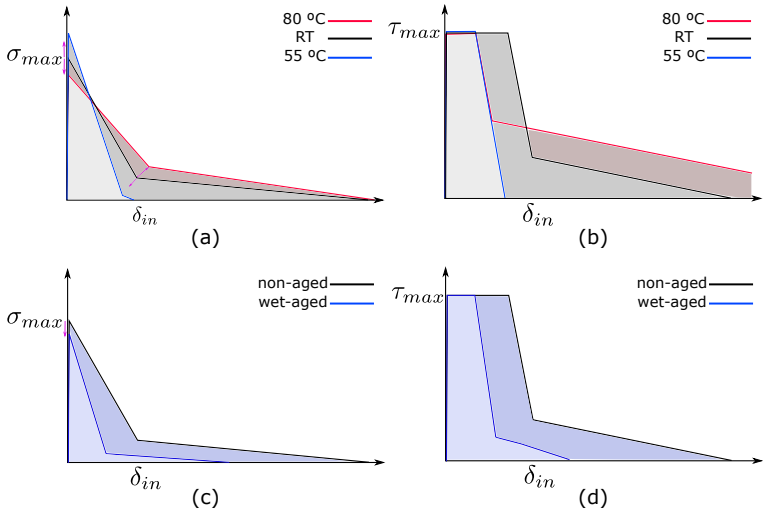

Fig. 9.1.: Schematic illustration of environmental conditions influences on the simplified cohesive laws.

9.1.3 Simulation of bonded joints under different temperature and ageing conditions

A new formulation for cohesive elements, based on the work of Turon et al. [155] and Jensen et al. [55] has been proposed to simulate bonded joints subjected to different environmental conditions. In the original formulation, it is not allowed to add the effect of environmental changes while only the bi-linear cohesive law can be used. The new formulation presented a cohesive zone model with a multilinear cohesive law as a function of the temperature and ageing.

The new formulation has been used to simulate different configurations of adhesively bonded joints tested under different temperatures (-55°C, RT and 80°C) and exposed to different ageing conditions. The finite element numerical results have been compared to the available experimental work done by the authors. Good correlation was observed between model predictions and experimental data. Besides, using the current formulation allows to model structures with initial crack or without initial crack.

9.2 Future work

The following topics are suggested for possible developments:

- The proposed inverse method considered a 2D plane strain problem where the material response lies on the bondline. Further research could be devoted to

extend the method to combine the sources of the non-linearity not only in 2D but also in 3D such as the finite width of the specimen.

- As shown in this thesis, the proposed methodology has only been applied to measure the cohesive laws of bonded joints made from fibre-reinforced polymers. The method could be applied to various quasi-brittle materials such as concrete, polymer materials, metallic glasses and also other bio-materials.

- In the current work, the influence of environmental changes has been studied on the fracture behaviour of bonded joints under mode I and mode II while intensive research work could be introduced using MMB.

- This thesis shows the importance of long term ageing on the material degradation. Therefore, a more comprehensive test campaign can be performed for different ageing times (1,2,3,5 years) in order to obtain the cohesive laws as a function of time.

- The dependence of the cohesive laws with the temperature and ageing is defined using linear relations due to the reduced number of test data. An extensive test campaign under several temperatures, and exposed to different level of relative humidity can be performed to define more accurate expressions.

- Although The new formulation for cohesive elements was successfully verified, MMB test data can be useful to validate the model.

Part V

Annex

A

Obtaining the non-dimensional parameters

A parametric FE model is constructed for the half of the DCB specimen which has the arm thickness h and length of $(10h + L_{std} + 10h)$, shown in Figure A.1, using ABAQUS script [141] with 2D plane strain CPE4I elements with squared element size of 0.1 mm. The load F and moment M were applied to the left edge of the model while stress σ_i was applied to the element edges located at the studied length L_{std}, with $F = 1$ N, $M = 1$ N.mm and $\sigma_i = 1$ N/mm^2, and a symmetric boundary condition applied as shown in Fig. A.1. The values of δ_i^P, θ_i^P and u_i^P are extracted directly from the FE results where the superscript P refers to the acting loads F, M or σ_i where $i = 1{:}\ n$ and n is the number of integration points located along the studied length. The non-dimension form of $\hat{\delta}_i^P$ is calculated using Equations (3.8), (3.9) and (3.10). Likewise, the values of $\hat{\theta}_i^P$ and $\hat{u}_i^P$ are obtained. To obtain $\hat{K}_i^P$, Equations (3.2), (3.3) and (3.4) were applied where the values of K_i^P were computed using the VCCT method [48, 145, 146, 157]. In this work, $h = 2.50$ mm and $n = 200$ where $L_{std} = 20$ mm to cover the expected FPZ.

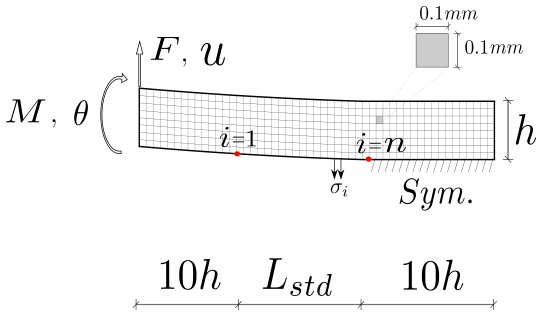

Fig. A.1.: Finite element model of half of the DCB and its boundary conditions.

B Cohesive laws dependence fitting matrices

The fitting matrices ($\mathcal{B}|^{*}_{\star}$, $\mathcal{C}|^{*}_{\star}$ and $\gamma|^{*}_{\star}$), obtained using Equations 8.11 and 8.5, are presented. The subscript $\star$ refers to the material type (A1 or A2) and the superscript $*$ refers to the values in the case of mode I or mode II.

$$\mathcal{B}|^{I}_{A1} = \frac{1}{10000}\begin{bmatrix} -20 & -12 & - & - \\ -73 & 125 & 21 & -1 \\ -68 & 125 & 20 & 100 \\ -61 & 125 & 20 & 111 \\ -50 & 125 & 20 & 115 \end{bmatrix} \quad , \quad \mathcal{B}|^{II}_{A1} = \frac{1}{10000}\begin{bmatrix} 0.1 & -7.5 & - & - \\ 0.1 & -1.3 & 0.1 & 70.5 \\ 0.1 & 75.3 & 0.1 & 55.4 \\ 0.1 & 75.3 & 0.1 & 55.4 \\ 0.1 & 125 & 0.1 & 94.2 \end{bmatrix} \tag{B.1}$$

$$\mathcal{C}|^{I}_{A1} = \frac{1}{1000}\begin{bmatrix} 1496.1 & 795.6 & 0 & 0 \\ -184.3 & 1000 & -459.9 & -37.3 \\ -262.5 & 1000 & -175.2 & 838 \\ -736.8 & 1000 & -171.1 & 910.3 \\ 316.4 & 1000 & -169.6 & 938 \end{bmatrix}$$

$$, \tag{B.2}$$

$$\mathcal{C}|^{II}_{A1} = \frac{1}{1000}\begin{bmatrix} -10.2 & 1108.1 & 0 & 0 \\ -10.2 & -39216.2 & -0.8 & 781.4 \\ 0.5 & 733.4 & -0.8 & 816.6 \\ 0.3 & 2561.1 & 36.7 & 529.1 \\ 0.3 & 4249.3 & -1.3 & 831.8 \end{bmatrix}$$

$$\gamma|^{I}_{A1} = \begin{bmatrix} -0.1273 & 0 \\ -0.2309 & -0.6 \\ -0.1841 & 0.3591 \\ -0.1131 & 0.4644 \\ 0.0073 & 0.5048 \end{bmatrix} \quad , \quad \gamma|^{II}_{A1} = \begin{bmatrix} -0.088 & 0 \\ -0.088 & -0.3712 \\ -0.378 & -0.2853 \\ -0.855 & 1.012 \\ 29999 & 0.5411 \end{bmatrix} \tag{B.3}$$

$$\mathcal{B}|^{I}_{A2} = \frac{1}{10000}\begin{bmatrix} 0.1 & -24 & 0 & 0 \\ 0.1 & -1604 & 0.1 & 70 \\ 0.1 & -1626 & 0.1 & 104 \\ 0.1 & -1671 & 0.1 & 109 \\ 0.1 & -1821 & 0.1 & 111 \end{bmatrix} \quad , \quad \mathcal{B}|^{II}_{A2} = \frac{1}{10000}\begin{bmatrix} 0 & -17 & 0 & 0 \\ 0 & -44 & 0 & 97 \\ 0 & -95 & 0 & 102 \\ 0 & -32 & 0 & 89 \\ 0 & 125 & 0 & 98 \end{bmatrix} \tag{B.4}$$

$$\mathcal{C}|^{I}_{A2} = \frac{1}{1000}\begin{bmatrix} -5.6 & 312.4 & 0 & 0 \\ 1.2 & 401.5 & -9.2 & 691.3 \\ 1.4 & 452.4 & -47.4 & 889.5 \\ 1.8 & 607.3 & -162 & 906.2 \\ 1000 & -14567.4 & 1000 & 912.1 \end{bmatrix}$$

$$, \tag{B.5}$$

$$\mathcal{C}|^{II}_{A2} = \frac{1}{1000}\begin{bmatrix} -203.5 & 623.2 & 0 & 0 \\ -1.3 & 1547.6 & -205.2 & 1352.9 \\ 1.2 & 1114.1 & -1.5 & 1439.8 \\ 0.2 & -258.7 & 0.5 & 1178.5 \\ 3.1 & 1000 & 0.5 & 999.2 \end{bmatrix}$$

$$\gamma|^{I}_{A2} = \begin{bmatrix} -0.3785 & 0 \\ 0.054 & -0.5292 \\ 0.0518 & -0.6296 \\ 0.0471 & -0.6425 \\ 0.0316 & -0.6476 \end{bmatrix} \quad , \quad \gamma|^{II}_{A2} = \begin{bmatrix} -0.1253 & 0 \\ -0.0127 & -0.8302 \\ -0.1219 & -0.8242 \\ -0.633 & -0.6587 \\ 199 & -0.5274 \end{bmatrix} \tag{B.6}$$

Bibliography

[1] Oliver Milman. „'Let's do it now': Greta Thunberg crosses Atlantic and calls for urgent climate action". In: *The Guardian* (Aug. 28, 2019) (cit. on p. 1).

[2] DN Markatos, KI Tserpes, E Rau, et al. „The effects of manufacturing-induced and in-service related bonding quality reduction on the mode-I fracture toughness of composite bonded joints for aeronautical use". In: *Composites Part B: Engineering* 45.1 (2013), pp. 556–564 (cit. on pp. 1, 2).

[3] RL Fernandes, MFSF de Moura, and RDF Moreira. „Effect of temperature on pure modes I and II fracture behavior of composite bonded joints". In: *Composites Part B: Engineering* 96 (2016), pp. 35–44 (cit. on pp. 3, 11, 79, 80, 95, 105).

[4] RL Fernandes, MFSF De Moura, and RDF Moreira. „Effect of moisture on pure mode I and II fracture behaviour of composite bonded joints". In: *International Journal of Adhesion and Adhesives* 68 (2016), pp. 30–38 (cit. on pp. 3, 11, 13, 80, 95, 105, 107).

[5] ST Amancio-Filho and JF Dos Santos. „Joining of polymers and polymer–metal hybrid structures: recent developments and trends". In: *Polymer Engineering & Science* 49.8 (2009), pp. 1461–1476 (cit. on pp. 3, 15).

[6] MD Banea and Lucas FM da Silva. „Adhesively bonded joints in composite materials: an overview". In: *Proceedings of the Institution of Mechanical Engineers, Part L: Journal of Materials: Design and Applications* 223.1 (2009), pp. 1–18 (cit. on pp. 3, 13, 107).

[7] S Budhe, MD Banea, S De Barros, and LFM Da Silva. „An updated review of adhesively bonded joints in composite materials". In: *International Journal of Adhesion and Adhesives* 72 (2017), pp. 30–42 (cit. on pp. 3, 8, 9, 12, 16).

[8] Shufeng Liu, Xiaoquan Cheng, Qian Zhang, et al. „An investigation of hygrothermal effects on adhesive materials and double lap shear joints of CFRP composite laminates". In: *Composites Part B: Engineering* 91 (2016), pp. 431–440 (cit. on p. 3).

[9] Ye Zhang, Anastasios P Vassilopoulos, and Thomas Keller. „Effects of low and high temperatures on tensile behavior of adhesively-bonded GFRP joints". In: *Composite Structures* 92.7 (2010), pp. 1631–1639 (cit. on p. 3).

[10] Jack R Vinson. „Adhesive bonding of polymer composites". In: *Polymer Engineering & Science* 29.19 (1989), pp. 1325–1331 (cit. on p. 7).

[11] Lucas FM Da Silva, Andreas Öchsner, and Robert D Adams. „Introduction to adhesive bonding technology". In: *Handbook of adhesion technology* (2018), pp. 1–7 (cit. on p. 7).

[12]Michael J Troughton. *Handbook of plastics joining: a practical guide*. William Andrew, 2008 (cit. on pp. 7–9).

[13]Erol Sancaktar. „Classification of adhesive and sealant materials“. In: *Handbook of Adhesion Technology* (2018), pp. 283–317 (cit. on pp. 9, 10).

[14]Phil Yarrington, James Zhang, Craig Collier, and Brett Bednarcyk. „Failure analysis of adhesively bonded composite joints“. In: *46th AIAA/ASME/ASCE/AHS/ASC Structures, Structural Dynamics and Materials Conference*. 2005, p. 2376 (cit. on p. 10).

[15]Albert Turon, Pedro P Camanho, Josep Costa, and Carlos G Dávila. „An interface damage model for the simulation of delamination under variable-mode ratio in composite materials“. In: (2004) (cit. on pp. 10, 19).

[16]Albert. Turon Travesa. *Simulation of delamination in composites under quasi-static and fatigue loading using cohesive zone models*. 2007 (cit. on p. 11).

[17]Mina Dawood and Sami Rizkalla. „Environmental durability of a CFRP system for strengthening steel structures“. In: *Construction and Building Materials* 24.9 (2010), pp. 1682–1689 (cit. on pp. 11, 13, 14, 107).

[18]Shan Li, Hui Tao Ren, Yi Yan Lu, and Mu Huan Shi. „Environmental degradation of carbon fiber reinforced polymer (CFRP) and steel bond subjected to hygrothermal aging and loading“. In: *Materials Science Forum*. Vol. 675. Trans Tech Publ. 2011, pp. 559–562 (cit. on pp. 11, 13, 107).

[19]Tien-Cuong Nguyen, Yu Bai, Xiao-Ling Zhao, and Riadh Al-Mahaidi. „Durability of steel/CFRP double strap joints exposed to sea water, cyclic temperature and humidity“. In: *Composite Structures* 94.5 (2012), pp. 1834–1845 (cit. on pp. 11, 13, 107).

[20]Yang Yong-xin, Yue Qing-rui, and Peng Fu-ming. „Experimental research on bond behavior of CFRP to steel“. In: *Int. Symp. Bond Behav. FRP Struct.(BBFS 2005)*. 2005, pp. 419–24 (cit. on pp. 11, 13, 107).

[21]Annette Roy, Elena Gontcharova-Benard, Jean-Louis Gacougnolle, and Peter Davies. „Hygrothermal effects on failure mechanisms of composite/steel bonded joints“. In: *Time dependent and nonlinear effects in polymers and composites*. ASTM International, 2000 (cit. on pp. 11, 13, 107).

[22]Joseph Mohan, A Ivanković, and Neal Murphy. „Effect of prepreg storage humidity on the mixed-mode fracture toughness of a co-cured composite joint“. In: *Composites Part A: Applied Science and Manufacturing* 45 (2013), pp. 23–34 (cit. on p. 11).

[23]DN Markatos, KI Tserpes, E Rau, K Brune, and Sp Pantelakis. „Degradation of mode-I fracture toughness of CFRP bonded joints due to release agent and moisture pre-bond contamination“. In: *The Journal of Adhesion* 90.2 (2014), pp. 156–173 (cit. on p. 11).

[24]KI Tserpes, DN Markatos, K Brune, et al. „A detailed experimental study of the effects of pre-bond contamination with a hydraulic fluid, thermal degradation, and poor curing on fracture toughness of composite-bonded joints“. In: *Journal of Adhesion Science and Technology* 28.18 (2014), pp. 1865–1880 (cit. on p. 11).

[25]S Budhe, A Rodríguez-Bellido, J Renart, JA Mayugo, and J Costa. „Influence of pre-bond moisture in the adherents on the fracture toughness of bonded joints for composite repairs“. In: *International Journal of Adhesion and Adhesives* 49 (2014), pp. 80–89 (cit. on p. 11).

[26] David A Bond and Paul A Smith. „Modeling the transport of low-molecular-weight penetrants within polymer matrix composites“. In: *Applied Mechanics Reviews* 59.5 (2006), pp. 249–268 (cit. on pp. 11, 13).

[27] Mohsen Heshmati, Reza Haghani, and Mohammad Al-Emrani. „Environmental durability of adhesively bonded FRP/steel joints in civil engineering applications: state of the art“. In: *Composites Part B: Engineering* 81 (2015), pp. 259–275 (cit. on pp. 13, 14, 16).

[28] Gabriel LaPlante and Pearl Lee-Sullivan. „Moisture effects on FM300 structural film adhesive: Stress relaxation, fracture toughness, and dynamic mechanical analysis“. In: *Journal of Applied Polymer Science* 95.5 (2005), pp. 1285–1294 (cit. on p. 13).

[29] KB Katnam, JP Sargent, AD Crocombe, H Khoramishad, and IA Ashcroft. „Characterisation of moisture-dependent cohesive zone properties for adhesively bonded joints“. In: *Engineering Fracture Mechanics* 77.16 (2010), pp. 3105–3119 (cit. on p. 13).

[30] Sabina Alessi, Giuseppe Pitarresi, and Giuseppe Spadaro. „Effect of hydrothermal ageing on the thermal and delamination fracture behaviour of CFRP composites“. In: *Composites Part B: Engineering* 67 (2014), pp. 145–153 (cit. on p. 14).

[31] JM Arenas, C Alía, R Ocaña, and JJ Narbón. „Degradation of adhesive joints for joining composite material with aluminum under immersion in water and motor oil“. In: *Procedia Engineering* 63 (2013), pp. 287–294 (cit. on p. 14).

[32] CDM Liljedahl, AD Crocombe, MA Wahab, and IA Ashcroft. „Modelling the environmental degradation of adhesively bonded aluminium and composite joints using a CZM approach“. In: *International Journal of Adhesion and Adhesives* 27.6 (2007), pp. 505–518 (cit. on p. 14).

[33] RA Gledhill and AJ Kinloch. „Environmental failure of structural adhesive joints“. In: *The journal of adhesion* 6.4 (1974), pp. 315–330 (cit. on p. 14).

[34] P Coronado, A Argüelles, J Viña, V Mollón, and I Viña. „Influence of temperature on a carbon–fibre epoxy composite subjected to static and fatigue loading under mode-I delamination“. In: *International Journal of Solids and Structures* 49.21 (2012), pp. 2934–2940 (cit. on p. 15).

[35] RD Adams and V Mallick. „The effect of temperature on the strength of adhesively-bonded composite-aluminium joints“. In: *The Journal of Adhesion* 43.1-2 (1993), pp. 17–33 (cit. on pp. 15, 79).

[36] RD Adams, J Coppendale, V Mallick, and H Al-Hamdan. „The effect of temperature on the strength of adhesive joints“. In: *International Journal of Adhesion and Adhesives* 12.3 (1992), pp. 185–190 (cit. on pp. 15, 16, 95).

[37] Lucas FM Da Silva and RD Adams. „Measurement of the mechanical properties of structural adhesives in tension and shear over a wide range of temperatures“. In: *Journal of Adhesion Science and Technology* 19.2 (2005), pp. 109–141 (cit. on pp. 15, 16, 95).

[38] MD Banea, LFM da Silva, and RDSG Campilho. „Effect of temperature on tensile strength and mode I fracture toughness of a high temperature epoxy adhesive“. In: *Journal of adhesion science and technology* 26.7 (2012), pp. 939–953 (cit. on p. 15).

[39]Mariana D Banea, Lucas FM da Silva, and RDSG Campilho. „Effect of temperature on the shear strength of aluminium single lap bonded joints for high temperature applications“. In: *Journal of Adhesion Science and Technology* 28.14-15 (2014), pp. 1367–1381 (cit. on p. 15).

[40]Georgia Charalambous, Giuliano Allegri, and Stephen R Hallett. „Temperature effects on mixed mode I/II delamination under quasi-static and fatigue loading of a carbon/epoxy composite“. In: *Composites Part A: Applied Science and Manufacturing* 77 (2015), pp. 75–86 (cit. on p. 16).

[41]P Coronado, A Argüelles, J Viña, and I Viña. „Influence of low temperatures on the phenomenon of delamination of mode I fracture in carbon-fibre/epoxy composites under fatigue loading“. In: *Composite Structures* 112 (2014), pp. 188–193 (cit. on p. 16).

[42]MD Banea, LFM Da Silva, and RDSG Campilho. „Mode I fracture toughness of adhesively bonded joints as a function of temperature: experimental and numerical study“. In: *International Journal of Adhesion and Adhesives* 31.5 (2011), pp. 273–279 (cit. on pp. 16, 105).

[43]Cassandra E Ojeda, Eric J Oakes, Jennifer R Hill, Dominic Aldi, and Gustaf A Forsberg. „Temperature effects on adhesive bond strengths and modulus for commonly used spacecraft stuctural adhesives“. In: (2011) (cit. on p. 16).

[44]Mariana D Banea and Lucas FM da Silva. „Mechanical characterization of flexible adhesives“. In: *The Journal of Adhesion* 85.4-5 (2009), pp. 261–285 (cit. on pp. 16, 105).

[45]IA Ashcroft, DJ Hughes, and SJ Shaw. „Mode I fracture of epoxy bonded composite joints: 1. Quasi-static loading“. In: *International Journal of Adhesion and Adhesives* 21.2 (2001), pp. 87–99 (cit. on p. 16).

[46]BC Ray. „Temperature effect during humid ageing on interfaces of glass and carbon fibers reinforced epoxy composites“. In: *Journal of Colloid and Interface Science* 298.1 (2006), pp. 111–117 (cit. on pp. 16, 105).

[47]Pedro Ponces Camanho, C Davila, and MF De Moura. „Numerical simulation of mixed-mode progressive delamination in composite materials“. In: *Journal of composite materials* 37.16 (2003), pp. 1415–1438 (cit. on p. 17).

[48]Ronald Krueger. „Virtual crack closure technique: history, approach, and applications“. In: *Applied Mechanics Reviews* 57.2 (2004), pp. 109–143 (cit. on pp. 17, 54, 131).

[49]Donald S Dugdale. „Yielding of steel sheets containing slits“. In: *Journal of the Mechanics and Physics of Solids* 8.2 (1960), pp. 100–104 (cit. on pp. 17, 30, 35, 36, 51).

[50]Grigory Isaakovich Barenblatt. „The mathematical theory of equilibrium cracks in brittle fracture“. In: *Advances in applied mechanics*. Vol. 7. Elsevier, 1962, pp. 55–129 (cit. on p. 17).

[51]Y Mi, MA Crisfield, GAO Davies, and HB Hellweg. „Progressive delamination using interface elements“. In: *Journal of composite materials* 32.14 (1998), pp. 1246–1272 (cit. on p. 18).

[52]A Turon, EV González, C Sarrado, G Guillamet, and P Maimí. „Accurate simulation of delamination under mixed-mode loading using a cohesive model with a mode-dependent penalty stiffness“. In: *Composite Structures* 184 (2018), pp. 506–511 (cit. on pp. 19, 44, 119, 121).

[53]Viggo Tvergaard and John W Hutchinson. „The relation between crack growth resistance and fracture process parameters in elastic-plastic solids“. In: *Journal of the Mechanics and Physics of Solids* 40.6 (1992), pp. 1377–1397 (cit. on p. 19).

[54]Vinay K Goyal, Eric R Johnson, and Carlos G Davila. „Irreversible constitutive law for modeling the delamination process using interfacial surface discontinuities“. In: *Composite Structures* 65.3-4 (2004), pp. 289–305 (cit. on p. 19).

[55]Simon Mosbjerg Jensen, MJ Martos, Brian Lau Verndal Bak, and Esben Lindgaard. „Formulation of a mixed-mode multilinear cohesive zone law in an interface finite element for modelling delamination with R-curve effects“. In: *Composite Structures* 216 (2019), pp. 477–486 (cit. on pp. 19, 111–113, 127).

[56]BSEN ISO. „15024: 2001“. In: *Fibre-reinforced plastic composites. Determination of mode I interlaminar fracture toughness, GIC, for unidirectional reinforced materials. BSI* (2002) (cit. on p. 19).

[57]ISO-25217. „Determination of the mode 1 adhesive fracture energy of structural adhesive joints using double cantilever beam and tapered double cantilever beam specimens“. In: *Adhesives* (2009) (cit. on pp. 19, 22, 23).

[58]ASTM Standard. „D5228-94, Standard Test Method for Mode I Interlaminar Fracture Toughness of Unidirectional Reinforced Polymer Matrix Composites“. In: *DCB Standard, American Society for Testing and Materials* (1994) (cit. on p. 19).

[59]JD Barrett and RO Foschi. „Mode II stress-intensity factors for cracked wood beams“. In: *Engineering Fracture Mechanics* 9.2 (1977), pp. 371–378 (cit. on p. 20).

[60]Peter Stephen Vanderkley. „Mode I-mode II delamination fractrue toughness of a unidirectional graphite/epoxy composite“. PhD thesis. Texas A&M University, 1981 (cit. on p. 20).

[61]M-L Benzeggagh, Y Prel, and F-X de Charentenay. „Instrumentation of mode I and mode II tests for crack tip strain profile study under static and cyclic loading“. In: *NASA STI/Recon Technical Report A* 86 (1985), pp. 291–312 (cit. on p. 20).

[62]Hironori Maikuma, John W Gillespie Jr, and Dick J Wilkins. „Mode II interlaminar fracture of the center notch flexural specimen under impact loading“. In: *Journal of composite materials* 24.2 (1990), pp. 124–149 (cit. on p. 20).

[63]Kazuro Kageyama, Masanori Kikuchi, and Noboru Yanagisawa. „Stabilized end notched flexure test: characterization of mode II interlaminar crack growth“. In: *Composite Materials: Fatigue and Fracture (Third volume)*. ASTM International, 1991 (cit. on p. 20).

[64]Rudolf Prinz and Michael Gädke. „Characterization of interlaminar mode I and mode II fracture in CFRP laminates“. In: *Proc. of Inter. Conf. on Spacecraft Structures and Mechanical Testing. ESA SP-321*. 1991, pp. 97–102 (cit. on p. 20).

[65]DS Matsumoto, MA Vallance, and SK Gifford. „A new curvature-driven delamination test for measuring the mode II toughness of composites“. In: *Polymer composites* 17.2 (1996), pp. 171–179 (cit. on p. 20).

[66]RH Martin and BD Davidson. „Mode II fracture toughness evaluation using four point bend, end notched flexure test“. In: *Plastics, Rubber and Composites* 28.8 (1999), pp. 401–406 (cit. on p. 20).

[67]Francesco Caimmi, Roberto Frassine, and Andrea Pavan. „A new jig for mode II interlaminar fracture testing of composite materials under quasi-static and moderately high rates of loading“. In: *Engineering fracture mechanics* 73.16 (2006), pp. 2277–2291 (cit. on p. 20).

[68]ASTM Standard. „D7905/D7905M–14“. In: *Standard Test Method for Determination of the Mode II Interlaminar Fracture Toughness of Unidirectional Fiber-Reinforced Polymer Matrix Composites* (2014) (cit. on p. 20).

[69]ISO Standard. „15114 (2014) Fibre-reinforced plastic composites-determination of the mode II fracture resistance for unidirectionally reinforced materials using the calibrated end-loaded split (C-ELS) test and an effective crack length approach“. In: *International Standards Organization, Switzerland* (2014) (cit. on pp. 20, 25).

[70]M Pérez-Galmés, J Renart, C Sarrado, AJ Brunner, and A Rodríguez-Bellido. „Towards a consensus on mode II adhesive fracture testing: Experimental study“. In: *Theoretical and Applied Fracture Mechanics* 98 (2018), pp. 210–219 (cit. on pp. 20, 23–26, 56–61).

[71]András Szekrényes. „Crack stability of fracture specimens used to test unidirectional fiber reinforced material“. In: *Experimental mechanics* 50.4 (2010), pp. 473–482 (cit. on p. 21).

[72]A.A. Griffith. „The Phenomena of Rupture and Flow in solids“. In: *Philosophical Transactions of the Royal Society of London* 221 (1921), pp. 163–198 (cit. on p. 22).

[73]A.A. Griffith. „The theory of rupture“. In: *Proceedings of the First International Conference of Applied Mechanics*. Ed. by C.B. Biereno and J.M. Burgers. 1924, pp. 54–63 (cit. on p. 22).

[74]S. Hashemi, A.J. Kinloch, and J.G. Williams. „The analysis of interlaminar fracture in uniaxial fiber-polymer composites“. In: *Proceedings of the Royal Society A* 427.1872 (1990), pp. 173–199 (cit. on pp. 23–25, 68).

[75]AITM 1.0006:1994. „Carbon Fibre Reinforced Plastics Determination of interlaminar fracture toughness energy (Mode II GIIC-TEST).“ In: *Airbus Industrie Test Method* 2 (), pp. 1–8 (cit. on p. 24).

[76]P. Davies, G.D. Sims, B. R K Blackman, et al. „Comparison of test configurarions for the determination of GIIC : results from an international round robin“. In: *Plastics, Rubber and Composites* 28.September (1999), pp. 432–437 (cit. on p. 24).

[77]T. K. O'Brien, G. B. Murri, and S. A. Salpekar. „Interlaminar Shear Fracture Toughness and Fatigue Thresholds for Composite Materials“. In: *Composite Materials: Fatigue and Fracture ASTM STP 1012, (2nd Volume)*. Ed. by P. A. Lagace. 1989, pp. 222–250 (cit. on p. 24).

[78]Joakim Schön, Tonny Nyman, Anders Blom, and Hans Ansell. „Numerical and experimental investigation of a composite ENF-specimen“. In: *Engineering Fracture Mechanics* 65.4 (2000), pp. 405–433 (cit. on p. 24).

[79]L. A. Carlsson, J. W. Gillespie, and B. R. Trethewey. „Mode II Interlaminar Fracture of Graphite/Epoxy and Graphite/PEEK“. In: *Journal of Reinforced Plastics and Composites* 5.3 (1986), pp. 170–187 (cit. on p. 24).

[80]A.J. Russell and K.N. Street. „Moisture and Temperature Effects on the Mixed-Mode Delamination Fracture of Unidirectional Graphite/Epoxy.“ In: *ASTM STP 876* (1985), pp. 349–370 (cit. on p. 24).

[81]B. D. Davidson, R. Krüger, and M. König. „Effect of stacking sequence on energy release rate distributions in multidirectional DCB and ENF specimens“. In: *Engineering Fracture Mechanics* 55.4 (1996), pp. 557–569 (cit. on p. 24).

[82]P. Davies, H.H. Kausch, J.G. Williams, et al. „Round-robin interlaminar fracture testing of carbon-fibre-reinforced epoxy and PEEK composites“. In: *Composites Science and Technology* 43.2 (1992), pp. 129–136 (cit. on p. 24).

[83]JIS K 7086. „Testing methods for interlaminar fracture toughness of carbon fibre reinforced plastics.“ In: *Japanese Standard association* (1993) (cit. on p. 24).

[84]S. Bhashyam and B.D. Davidson. „Evaluation of data reduction methods for the mixed mode bending test“. In: *Aiaa J.* 35.3 (1997), pp. 546–552 (cit. on p. 24).

[85]L.A. Carlsson, J.W. Gillespie, and R.B. Pipes. „On the Analysis and Design of the End Notched Flexure (ENF) specimen for Mode II Testing“. In: *Journal of Composite Materials* 20.6 (1986), pp. 594–604 (cit. on p. 24).

[86]G. B. Murri and R.H. Martin. „Effect of Initial Delamination on Mode I and Mode II Interlaminar Fracture Toughness and Fatigue Fracture Threshold“. In: *Composite Materials: Fatigue and Fracture (4th Volume), ASTM STP 1156*. Ed. by W. W. Stinchcomb Ashbaugh and N. E. ASTM International, West Conshohocken, PA, 1991, pp. 239–256 (cit. on p. 24).

[87]B. R K Blackman, A.J. Brunner, and J.G. Williams. „Mode II fracture testing of composites: a new look at an old problem“. In: *Engineering Fracture Mechanics* 73.16 (2006), pp. 2443–2455 (cit. on pp. 24, 25).

[88]B. R K Blackman, A.J. Kinloch, and M. Paraschi. „The determination of the mode II adhesive fracture resistance, GIIC, of structural adhesive joints: an effective crack length approach“. In: *Engineering Fracture Mechanics* 72.6 (2005), pp. 877–897 (cit. on p. 24).

[89]M.F.S.F. de Moura and A.B. de Morais. „Equivalent crack based analyses of ENF and ELS tests“. In: *Engineering Fracture Mechanics* 75.9 (2008), pp. 2584–2596 (cit. on pp. 24, 25).

[90]A. Arrese, N. Carbajal, G. Vargas, and F. Mujika. „A new method for determining mode II R-curve by the End-Notched Flexure test“. In: *Engineering Fracture Mechanics* 77.1 (2010), pp. 51–70 (cit. on p. 24).

[91]M.F.S.F. de Moura, R. D S G Campilho, and J. P M Gonçalves. „Pure mode II fracture characterization of composite bonded joints“. In: *International Journal of Solids and Structures* 46.6 (2009), pp. 1589–1595 (cit. on p. 24).

[92]J.J. Polaha, B.D. Davidson, R.C. Hudson, and A. Pieracci. „Effects of Mode Ratio, Ply Orientation and Precracking on the Delamination Toughness of a Laminated Composite.“ In: *Journal of Reinforced Plastics and Composites* 15.2 (1996), pp. 141–173 (cit. on p. 24).

[93]C. Schuecker and B.D. Davidson. „Evaluation of the accuracy of the four-point bend end-notched flexure test for mode II delamination toughness determination“. In: *Composites Science and Technology* 60 (2000), pp. 2137–2146 (cit. on p. 24).

[94]Y. Wang and J. G. Williams. „Corrections for mode II fracture toughness specimens of composites materials“. In: *Composites Science and Technology* 43.3 (1992), pp. 251–256 (cit. on p. 25).

[95]M.F.S.F. de Moura. „Numerical simulation of the ENF test for the mode-II fracture characterization of bonded joints“. In: *Journal of Adhesion Science and Technology* 20.1 (2006), pp. 37–52 (cit. on p. 25).

[96]MAL Silva, JJL Morais, MFSF De Moura, and JL Lousada. „Mode II wood fracture characterization using the ELS test“. In: *Engineering fracture mechanics* 74.14 (2007), pp. 2133–2147 (cit. on p. 25).

[97]AITM1-0068:2014. „Carbon Fibre Reinforced Plastics Determination of mode II fracture toughness energy of bonded joints (GIIC Test).“ In: *Airbus Industries Test Method* 1 (), pp. 1–21 (cit. on p. 25).

[98]James R Rice. „A path independent integral and the approximate analysis of strain concentration by notches and cracks“. In: *Journal of applied mechanics* 35.2 (1968), pp. 379–386 (cit. on pp. 25, 49).

[99]A.J. Paris and P.C. Paris. „Instantaneous evaluation of J and C“. In: *International Journal of Fracture* 38 (1988), pp. 19–21 (cit. on pp. 25, 26).

[100]Ulf Stigh, K Svante Alfredsson, and Anders Biel. „Measurement of cohesive laws and related problems“. In: *ASME 2009 international mechanical engineering congress and exposition*. American Society of Mechanical Engineers. 2009, pp. 293–298 (cit. on pp. 25–27).

[101]Magdalena Pérez-Galmés, J Renart, C Sarrado, A Rodríguez-Bellido, and J Costa. „A data reduction method based on the J-integral to obtain the interlaminar fracture toughness in a mode II end-loaded split (ELS) test“. In: *Composites Part A: Applied Science and Manufacturing* 90 (2016), pp. 670–677 (cit. on p. 26).

[102]G Alfano and M_A Crisfield. „Finite element interface models for the delamination analysis of laminated composites: mechanical and computational issues“. In: *International journal for numerical methods in engineering* 50.7 (2001), pp. 1701–1736 (cit. on p. 26).

[103]Raul DSG Campilho, Marcelo FSF de Moura, Dimitra A Ramantani, and João PM Gonçalves. „Obtaining the cohesive laws of a trapezoidal mixed-mode damage model using an inverse method“. In: *Ciência & Tecnologia dos Materiais* 20.1-2 (2008), pp. 81–86 (cit. on p. 26).

[104]N Chandra, H Li, C Shet, and H Ghonem. „Some issues in the application of cohesive zone models for metal–ceramic interfaces“. In: *International Journal of Solids and Structures* 39.10 (2002), pp. 2827–2855 (cit. on p. 26).

[105]Raul DSG Campilho, Mariana D Banea, JABP Neto, and Lucas FM da Silva. „Modelling adhesive joints with cohesive zone models: effect of the cohesive law shape of the adhesive layer“. In: *International journal of adhesion and adhesives* 44 (2013), pp. 48–56 (cit. on p. 26).

[106]BRK Blackman, H Hadavinia, Anthony J Kinloch, and JG Williams. „The use of a cohesive zone model to study the fracture of fibre composites and adhesively-bonded joints“. In: *International Journal of Fracture* 119.1 (2003), pp. 25–46 (cit. on pp. 26, 44, 45).

[107]Viggo Tvergaard and John W Hutchinson. „The influence of plasticity on mixed mode interface toughness“. In: *Journal of the Mechanics and Physics of Solids* 41.6 (1993), pp. 1119–1135 (cit. on p. 26).

[108]Viggo Tvergaard and John W Hutchinson. „On the toughness of ductile adhesive joints“. In: *Journal of the Mechanics and Physics of Solids* 44.5 (1996), pp. 789–800 (cit. on p. 26).

[109]KS Madhusudhana and R Narasimhan. „Experimental and numerical investigations of mixed mode crack growth resistance of a ductile adhesive joint“. In: *Engineering Fracture Mechanics* 69.7 (2002), pp. 865–883 (cit. on p. 26).

[110]H Li and N Chandra. „Analysis of crack growth and crack-tip plasticity in ductile materials using cohesive zone models“. In: *International Journal of Plasticity* 19.6 (2003), pp. 849–882 (cit. on p. 26).

[111]BD Davidson and RA Schapery. „Effect of finite width on deflection and energy release rate of an orthotropic double cantilever specimen“. In: *Journal of Composite Materials* 22.7 (1988), pp. 640–656 (cit. on p. 26).

[112]Karl-Fredrik Nilsson. „On growth of crack fronts in the DCB-test“. In: *Composites Engineering* 3.6 (1993), pp. 527–546 (cit. on p. 26).

[113]Sylvain Popineau, Benoît Gautier, Pierre Slangen, and Martin ER Shanahan. „A 3D effect in the wedge adhesion test: application of speckle interferometry“. In: *The Journal of Adhesion* 80.12 (2004), pp. 1173–1194 (cit. on p. 26).

[114]Bent F Sørensen. „Cohesive law and notch sensitivity of adhesive joints“. In: *Acta Materialia* 50.5 (2002), pp. 1053–1061 (cit. on p. 27).

[115]Bent F Sørensen and Torben K Jacobsen. „Determination of cohesive laws by the J integral approach“. In: *Engineering fracture mechanics* 70.14 (2003), pp. 1841–1858 (cit. on p. 27).

[116]Bent F Sørensen and Torben K Jacobsen. „Characterizing delamination of fibre composites by mixed mode cohesive laws“. In: *Composites science and technology* 69.3 (2009), pp. 445–456 (cit. on p. 27).

[117]Tobias Andersson and Ulf Stigh. „The stress–elongation relation for an adhesive layer loaded in peel using equilibrium of energetic forces“. In: *International Journal of Solids and Structures* 41.2 (2004), pp. 413–434 (cit. on p. 27).

[118]Karin Leffler, K Svante Alfredsson, and Ulf Stigh. „Shear behaviour of adhesive layers“. In: *International Journal of Solids and Structures* 44.2 (2007), pp. 530–545 (cit. on p. 27).

[119]Ulf Stigh, Anders Biel, and Tomas Walander. „Shear strength of adhesive layers–models and experiments“. In: *Engineering Fracture Mechanics* 129 (2014), pp. 67–76 (cit. on p. 27).

[120]RL Fernandes, RDSG Campilho, ACC Leitão, and JCS Azevedo. „Numerical evaluation of the direct method for cohesive law extraction in shear by the End-Notched Flexure test“. In: *Procedia Engineering* 114 (2015), pp. 94–101 (cit. on p. 27).

[121]Tomas Walander, Anders Biel, and Ulf Stigh. „An evaluation of the temperature dependence of cohesive properties for two structural epoxy adhesives“. In: *19th European Conference on Fracture, Kazan, Russia, Aug. 26-31 2012*. Kazan Scientific Centre of the Russian Academy of Sciences. 2012 (cit. on pp. 27, 28).

[122]Tomas Walander, Anders Biel, and Ulf Stigh. „Temperature dependence of cohesive laws for an epoxy adhesive in Mode I and Mode II loading“. In: *International Journal of Fracture* 183.2 (2013), pp. 203–221 (cit. on p. 27).

[123]Carlos Sarrado, Albert Turon, Josep Costa, and Jordi Renart. „An experimental analysis of the fracture behavior of composite bonded joints in terms of cohesive laws“. In: *Composites Part A: Applied Science and Manufacturing* 90 (2016), pp. 234–242 (cit. on pp. 27, 28, 35, 46, 48–50).

[124]GF Dias, MFSF de Moura, JAG Chousal, and J Xavier. „Cohesive laws of composite bonded joints under mode I loading“. In: *Composite Structures* 106 (2013), pp. 646–652 (cit. on p. 27).

[125]RMRP Fernandes, JAG Chousal, MFSF De Moura, and J Xavier. „Determination of cohesive laws of composite bonded joints under mode II loading“. In: *Composites Part B: Engineering* 52 (2013), pp. 269–274 (cit. on p. 27).

[126]Larissa Sorensen, John Botsis, Th Gmür, and Laurent Humbert. „Bridging tractions in mode I delamination: Measurements and simulations“. In: *Composites Science and Technology* 68.12 (2008), pp. 2350–2358 (cit. on p. 29).

[127]G Pappas, LP Canal, and J Botsis. „Characterization of intralaminar mode I fracture of AS4/PPS composite using inverse identification and micromechanics“. In: *Composites Part A: Applied Science and Manufacturing* 91 (2016), pp. 117–126 (cit. on p. 29).

[128]MJ Donough, AJ Gunnion, AC Orifici, and CH Wang. „Scaling parameter for fatigue delamination growth in composites under varying load ratios“. In: *Composites Science and Technology* 120 (2015), pp. 39–48 (cit. on p. 29).

[129]Ainhoa Arrese, Ana Boyano, Juan De Gracia, and Faustino Mujika. „A novel procedure to determine the cohesive law in DCB tests“. In: *Composites Science and Technology* 152 (2017), pp. 76–84 (cit. on pp. 29, 35, 46–48).

[130]FAM Pereira, MFSF de Moura, N Dourado, et al. „Direct and inverse methods applied to the determination of mode I cohesive law of bovine cortical bone using the DCB test“. In: *International Journal of Solids and Structures* 128 (2017), pp. 210–220 (cit. on p. 29).

[131]Priyank Upadhyaya, Samit Roy, Mohammad H Haque, and Hongbing Lu. „A novel numerical–experimental approach for predicting delamination in high temperature polymer matrix composites“. In: *Composite Structures* 104 (2013), pp. 118–124 (cit. on p. 29).

[132]Roberta Massabò, Daniel R Mumm, and Briann Cox. „Characterizing mode II delamination cracks in stitched composites“. In: *International journal of fracture* 92.1 (1998), pp. 1–38 (cit. on pp. 29, 51).

[133]Jialai Wang and Pizhong Qiao. „Novel beam analysis of end notched flexure specimen for mode-II fracture“. In: *Engineering Fracture Mechanics* 71.2 (2004), pp. 219–231 (cit. on pp. 29, 51).

[134]A Arrese, N Insausti, F Mujika, M Perez-Galmés, and J Renart. „A novel experimental procedure to determine the cohesive law in ENF tests“. In: *Composites Science and Technology* 170 (2019), pp. 42–50 (cit. on p. 29).

[135]JCS Azevedo, RDSG Campilho, FJG da Silva, TMS Faneco, and RM Lopes. „Cohesive law estimation of adhesive joints in mode II condition“. In: *Theoretical and Applied Fracture Mechanics* 80 (2015), pp. 143–154 (cit. on p. 29).

[136]Pere Maimí, Emilio V González, Narcís Gascons, and Lluís Ripoll. „Size effect law and critical distance theories to predict the nominal strength of quasibrittle structures“. In: *Applied mechanics reviews* 65.2 (2013), p. 020803 (cit. on pp. 30, 31).

[137]AM Kabeel, P Maimí, N Gascons, and EV González. „Net-tension strength of double lap joints taking into account the material cohesive law“. In: *Composite Structures* 112 (2014), pp. 207–213 (cit. on p. 30).

[138]A Ortega, P Maimí, EV González, and D Trias. „Characterization of the translaminar fracture cohesive law“. In: *Composites Part A: Applied Science and Manufacturing* 91 (2016), pp. 501–509 (cit. on pp. 30, 31, 35, 37, 40–42, 53, 54).

[139]S Mall and JC Newman. „The Dugdale model for compact specimen“. In: *Fracture mechanics: sixteenth symposium*. ASTM International. 1985 (cit. on pp. 35, 36).

[140]R.D.S.G. Campilho, M.F.S.F. de Moura, and J.J.M.S. Domingues. „Using a cohesive damage model to predict the tensile behaviour of CFRP single-strap repairs“. In: *International Journal of Solids and Structures* 45.5 (2008), pp. 1497–1512 (cit. on p. 41).

[141]ABAQUS. *ABAQUS 6.14 User's Manual*. 2014 (cit. on pp. 44, 54, 117, 131).

[142]S Hashemi, AJ Kinloch, and JG Williams. „The effects of geometry, rate and temperature on the mode I, mode II and mixed-mode I/II interlaminar fracture of carbon-fibre/poly (ether-ether ketone) composites“. In: *Journal of Composite Materials* 24.9 (1990), pp. 918–956 (cit. on p. 45).

[143]Hiroshi Tada, Paul C Paris, and George R Irwin. „The stress analysis of cracks“. In: *Handbook, Del Research Corporation* (1973) (cit. on p. 53).

[144]S. Abdel Monsef, A. Ortega, A. Turon, P. Maimí, and J. Renart. „An efficient method to extract a mode I cohesive law for bonded joints using the double cantilever beam test“. In: *Composites Part B: Engineering* 178 (2019), p. 107424 (cit. on pp. 53, 54).

[145]AB De Morais. „Calculation of stress intensity factors by the force method“. In: *Engineering Fracture Mechanics* 74.5 (2007), pp. 739–750 (cit. on pp. 54, 131).

[146]Qinghua Han, Yaru Wang, Yue Yin, and Danni Wang. „Determination of stress intensity factor for mode I fatigue crack based on finite element analysis“. In: *Engineering Fracture Mechanics* 138 (2015), pp. 118–126 (cit. on pp. 54, 131).

[147]BS ISO. „25217: 2009, Adhesives–Determination of the Mode I Adhesive Fracture Energy of Structural Adhesive Joints Using Double Cantilever Beam and Tapered Double Cantilever Beam Specimens“. In: *British Standard* (2009) (cit. on pp. 56, 66, 68, 69, 79).

[148]ISO 15114: 2014. *Fibre-Reinforced Plastic Composites-Determination of the Mode II Fracture Resistance for Unidirectionally Reinforced Materials Using the Calibrated End-Loaded Split (C-ELS) Test and an Effective Crack Length Approach*. 2014 (cit. on pp. 56, 82–85).

[149]ASTM D7905/D7905M-14. *Standard test method for determination of the Mode II interlaminar fracture toughness of unidirectional fiber-reinforced polymer matrix composites*. 2014 (cit. on p. 56).

[150]J Renart, N Blanco, E Pajares, et al. „Side Clamped Beam (SCB) hinge system for delamination tests in beam-type composite specimens“. In: *Composites Science and Technology* 71.8 (2011), pp. 1023–1029 (cit. on p. 66).

[151]International Organization for Standardization (Ginebra). *ISO 14125: fibre-reinforced plastic composites: determination of flexural properties*. ISO, 1998 (cit. on p. 68).

[152]J Moller, R Hunter, J Molina, et al. „Influence of the temperature on the fracture energy of a methacrylate adhesive for mining applications“. In: *Applied Adhesion Science* 3.1 (2015), p. 14 (cit. on pp. 96, 106).

[153]José M Arenas, Rosa Ocaña, Cristina Alía, Julián J Narbón, and Manuel Islán. „Fracture energy in structural adhesive joints of composite-aluminum under adverse environments conditions“. In: *Journal of Adhesion Science and Technology* 28.2 (2014), pp. 201–214 (cit. on p. 105).

[154]AD Crocombe, YX Hua, WK Loh, MA Wahab, and IA Ashcroft. „Predicting the residual strength for environmentally degraded adhesive lap joints“. In: *International Journal of Adhesion and Adhesives* 26.5 (2006), pp. 325–336 (cit. on p. 105).

[155]A Turon, Pedro Ponces Camanho, J Costa, and CG Dávila. „A damage model for the simulation of delamination in advanced composites under variable-mode loading“. In: *Mechanics of Materials* 38.11 (2006), pp. 1072–1089 (cit. on pp. 111–113, 127).

[156]Ronald Krueger, Isabelle L Paris, T Kevin O'Brien, and Pierre J Minguet. „Fatigue life methodology for bonded composite skin/stringer configurations“. In: *Journal of Composites, Technology and Research* 24.2 (2002), pp. 308–331 (cit. on p. 121).

[157]LB Freund. „Stress intensity factor calculations based on a conservation integral“. In: *International Journal of Solids and Structures* 14.3 (1978), pp. 241–250 (cit. on p. 131).